12-31-2020

Development of novel inks and approaches for printing tissues and organs

Shen Ji
New Jersey Institute of Technology

Copyright Warning & Restrictions

The copyright law of the United States (Title 17, United States Code) governs the making of photocopies or other reproductions of copyrighted material.

Under certain conditions specified in the law, libraries and archives are authorized to furnish a photocopy or other reproduction. One of these specified conditions is that the photocopy or reproduction is not to be "used for any purpose other than private study, scholarship, or research." If a, user makes a request for, or later uses, a photocopy or reproduction for purposes in excess of "fair use" that user may be liable for copyright infringement,

This institution reserves the right to refuse to accept a copying order if, in its judgment, fulfillment of the order would involve violation of copyright law.

Please Note: The author retains the copyright while the New Jersey Institute of Technology reserves the right to distribute this thesis or dissertation

Printing note: If you do not wish to print this page, then select "Pages from: first page # to: last page #" on the print dialog screen

ABSTRACT

DEVELOPMENT OF NOVEL INKS AND APPROACHES FOR PRINTING TISSUES AND ORGANS

by
Shen Ji

Tissue engineering is a multidisciplinary field that investigates and develops new methods to repair, regenerate and replace damaged tissues and organs, or to develop biomaterial platforms as in vitro models. Tissue engineering approaches require the fabrication of scaffolds using biomaterials or fabrication of living tissues using cells. As the demands of customized, implantable tissue/organs are increasing and becoming more urgent, conventional scaffold fabrication approaches are difficult to meet the requirements, especially for complex large-scale tissue fabrication. In this regard, three-dimensional (3D) printing attracted more interest over the past decades due to its unrivaled ability to fabricate highly customized tissues or scaffolds from patients' medical images using computer aided design (CAD), as well as its flexibility, cost-effectiveness, and high efficiency. And more recently, 3D bioprinting can fabricate cellular constructs using a "bioink", an aqueous composite formulation that contained live cells as a mandatory component, which is a big step towards functional organ fabrications.

However, to fully realize the potential of 3D (bio)printing in tissue engineering, there are still a lot of barriers before implantable artificial organs, including but not limited to vascularization of fabricated tissue/organs, multicellular biofabrication, limited functional biomaterial, and dynamic maintenance/remodeling. To address some of these problems, this dissertation aims to develop novel inks and approaches for printing tissue and organs. Firstly, a novel bioprinting approach is developed to create user-defined

complex perfusable channels within cell-laden hydrogels, which uses commercially available bioprinters, hydrogels, and open-source software. The printing process is cell-friendly, and the channels could be further endothelialized to make the cell-laden hydrogel a vascularized tissue. Secondly, novel bioinks from UV-responsive norbornene-functionalized carboxymethyl cellulose macromers are developed. The cost-effectiveness, tunability, degradability, and cytocompatibility make this bioink platform a good addition to the current available bioink library. Thirdly, considering the demands of fabricating hard degradable scaffolds for bone tissue engineering, a polyester-based ink platform with tunable bioactivity is developed. Functionalized 3D printed scaffolds show a significant impact that enhanced the osteogenesis of human stem cells. Finally, the impact of the architectures of the 3D printed scaffolds on stem cell differentiation is investigated, which demonstrated enhanced osteogenesis of human stem cells on scaffolds with wavy architectures, compared with on scaffolds with orthogonal architectures.

DEVELOPMENT OF NOVEL INKS AND APPROACHES FOR PRINTING TISSUES AND ORGANS

by
Shen Ji

A Dissertation
Submitted to the Faculty of
New Jersey Institute of Technology
in Partial Fulfillment of the Requirements for the Degree of
Doctor of Philosophy in Chemical Engineering

Otto H. York Department of
Chemical and Materials Engineering

December 2020

.

APPROVAL PAGE

DEVELOPMENT OF NOVEL INKS AND APPROACHES FOR PRINTING TISSUES AND ORGANS

Shen Ji

Dr. Murat Guvendiren, Dissertation Advisor Assistant Professor, Chemical & Materials Engineering, NJIT	Date
Dr. Edward L. Dreizin, Committee Member Distinguished Professor, Chemical & Materials Engineering, NJIT	Date
Dr. Treena Arinzeh, Committee Member Distinguished Professor, Biomedical Engineering, NJIT	Date
Dr. Roman Voronov, Committee Member Associate Professor, Chemical & Materials Engineering, NJIT	Date
Dr. Xiaoyang Xu, Committee Member Associate Professor, Chemical & Materials Engineering, NJIT	Date

BIOGRAPHICAL SKETCH

Author: Shen Ji

Degree: Doctor of Philosophy

Date: December 2020

Undergraduate and Graduate Education:

- Doctor of Philosophy in Chemical Engineering,
  New Jersey Institute of Technology, Newark, NJ, 2020

- Master of Science in Chemical Engineering,
  New Jersey Institute of Technology, Newark, NJ, 2016

- Bachelor of Science in Pharmaceutical Engineering,
  Yunnan University, Kunming, China, 2013

Major: Chemical Engineering

Publications:

Peer-reviewed Journal Articles

S. Ji, A. Abaci, T. Morrison, W.M. Gramlich, M. Guvendiren, Novel bioinks from UV-responsive Norbornene-functionalized Carboxymethyl Cellulose Macromers, Bioprinting 18 (2020) e00083.

S. Ji, M. Guvendiren, 3D Printed Wavy Scaffolds Enhance Mesenchymal Stem Cell Osteogenesis, Micromachines (Basel) 11(1) (2019).

S. Ji, E. Almeida, M. Guvendiren, 3D Bioprinting of Complex Channels within Cell-laden Hydrogels, Acta Biomaterialia 95 (2019) 214-224.

S. Ji, K. Dube, J.P. Chesterman, S.L. Fung, C.Y. Liaw, J. Kohn, M. Guvendiren, Polyester-based Ink Platform with Tunable Bioactivity for 3D Printing of Tissue Engineering Scaffolds, Biomaterials Science 7(2) (2019) 560-570.

C.Y. Liaw, **S. Ji**, M. Guvendiren, Engineering 3D hydrogels for Personalized in vitro Human Tissue Models, Advanced Healthcare Materials 7(4) (2018) 5.

S. Ji, M. Guvendiren, Recent Advances in Bioink Design for 3D Bioprinting of Tissues and Organs, Frontiers in Bioengineering and Biotechnology 5 (2017) 23.

Patent

Murat Guvendiren, Shen Ji, "Additive Manufacturing of Channels," US20200047399A1

Presentations:

Novel Bioinks from UV-Responsive Norbornene-Functionalized Carboxymethyl Cellulose Macromers, AIChE 2020 Annual Meeting, November 14-20, 2020, online, [podium]

3D Bioprinting Vascularized Constructs for Cancer Models, BMES 2019 Annual Meeting, October 16-19, 2019, Philadelphia, PA. [poster]

Bioprinting of Complex 3D Vascular Networks within Cell-Laden Hydrogels, 2nd National Symposium on Mechanobiology, October 12, 2019, St. Louis, MO. [poster]

3D Bioprinting of Complex Channels within Cell-Laden Hydrogels, 45th Northeast Bioengineering Conference Annual Meeting, March 20, 2019, New Brunswick, NJ. [podium]

Bioprinting of Large-Scale Hydrogels with Built-in Vascular Channels, AIChE 2018 Annual Meeting, October 28-November 2, 2018, Pittsburgh, PA. [podium]

3D Printing Vascular Networks with Photocurable and Sacrificial Hydrogels, 2018 Annual Center for Engineering MechanoBiology Retreat, July 26 – 27, 2018, Swarthmore, PA. [poster]

Rapidly Constructing 3D Vascular Networks with Photocurable and Sacrificial Hydrogels, Thermal Analysis Forum of Delaware Valley Spring Symposium, April 3, 2018, Rutgers University-Camden, NJ. [poster]

Rapidly Constructing 3D Vascular Networks with Photocurable and Sacrificial Hydrogels, NJ Symposium on Biomaterials Science, October 23-24, 2017, New Brunswick, NJ. [poster]

This dissertation is dedicated to my beloved：
my wife, Hao Shi,
my mother, Junying Wu,
my father, Yanping Ji

谨以此论文献给:
我的妻子石昊，
我的母亲吴俊英，
我的父亲季延平

ACKNOWLEDGMENT

First of all, I would like to express my deep gratitude to Prof. Murat Guvendiren for his excellent guidance, caring, patience, continuous support, and for providing me an opportunity to be involved in so many exciting projects. He is not only my research advisor, but also my life-time friend and mentor. I was more than fortunate to be his student.

I would like to thank the committee members, Prof. Edward Dreizin, Prof. Treena Arinzeh, Prof. Roman Voronov, and Prof. Xiaoyang Xu. Their advice and insight are invaluable to me.

I also want to thank all the funding sources: NJIT Chemical and Material Science Department for supporting my teaching assistantship, National Science Foundation (DMR-1714882, CMMI: 15-48571) for supporting my research assistantship.

Finally, I would like to extend my appreciation to my colleagues: Dr. Chya-yan Liaw, Andrew House, and Alperen Abaci. You make this group collaborative, interactive, creative, and productive. I will always remember our good times in 311 York Center. Thank you to all the masters and undergraduate students that I have mentored, namely, Emily Almeida, Hazal Yalcin, Piuli Faizur, Jaspal Kaur, Fiona Dunn, Christopher Fitzharris, Daniel King, Christina Gedeon, Asma Elgouz, Mahima Choudhury, and Ecem Badruk.

TABLE OF CONTENTS

Chapter	Page
1 INTRODUCTION……..……..	1
1.1 3D Printing Technologies for Tissue Engineering and Regenerative Medicine.	1
1.2 3D Bioprinting and 3D Printing of Biomaterials.....	2
1.3 Currently Available Bioinks and Biomaterial inks.....	5
1.4 Complex 3D Bioprinting.....	10
1.5 Objectives.....	13
1.6 Dissertation Organization.....	14
2 3D BIOPRINTING OF COMPLEX CHANNELS WITHIN CELL-LADEN HYDROGELS.....	15
2.1 Introduction	15
2.2 Materials and Methods.....	19
2.2.1 Polymer Synthesis.....	19
2.2.2 Ink Preparation.....	19
2.2.3 Rheological Characterization of Ink Formulations.....	20
2.2.4 Printer Parameter Optimization (Line Test).....	21
2.2.5 Scaffold Design.....	21
2.2.6 Preparation of Methacrylated Glass Slides.....	21
2.2.7 3D Printing of Sacrificial Hydrogel within the Matrix Hydrogel.....	22
2.2.8 Cell Culture and Characterization.....	23
2.2.9 Statistical Methods.....	24
2.3 Results.....	25

TABLE OF CONTENTS
(Continued)

Chapter		Page
	2.3.1 Preparation and Characterization of Inks	25
	2.3.2 Line Tests Results for Matrix Hydrogel Inks	26
	2.3.3 Rheological Properties of the Printed Matrix Hydrogels	28
	2.3.4 Line Tests Results for Sacrificial Hydrogel Ink	29
	2.3.5 Controlling Channel Size with Print Speed	30
	2.3.6 3D Printing of Perfusable Channels Embedded within Hydrogels	32
	2.3.7 Cell Culture within Channels	33
	2.3.8 Bioprinting of Stem Cell-laden Hydrogels with Embedded Channels	34
	2.4 Discussion	35
	2.5 Conclusion	40
3	NOVEL BIOINKS FROM UV-RESPONSIVE NORBORNENE-FUNCTIONALIZED CARBOXYMETHYL CELLULOSE MACROMERS	42
	3.1 Introduction	42
	3.2 Materials and Methods	46
	3.2.1 Polymer Synthesis	46
	3.2.2 Cell Culture and Maintenance	47
	3.2.3 Ink Preparation	48
	3.2.4 Rheological Characterization of the Ink Formulations	48
	3.2.5 Mechanical Properties of the Crosslinked Ink Formulations	49
	3.2.6 Scaffold Design	49
	3.2.7 Line Test	50

TABLE OF CONTENTS
(Continued)

Chapter **Page**

3.2.8 Printability Test..... 50

3.2.9 3D Bioprinting of Cell-laden Hydrogels..... 50

3.2.10 Cell Viability Tests..... 51

3.2.11 Statistical Methods..... 51

3.3 Results..... 51

3.3.1 Bioink Formulations..... 51

3.3.2 Rheological Test Results..... 53

3.3.3 Mechanical Tests Results..... 54

3.3.4 Swelling Tests Results..... 55

3.3.5 Line Test Results..... 55

3.3.6 Printability Test Results..... 56

3.3.7 Bioprinting Test Results..... 57

3.4 Discussion..... 58

3.5 Conclusions..... 63

4 POLYESTER-BASED INK PLATFORM WITH TUNABLE BIOACTIVITY FOR 3D PRINTING OF TISSUE ENGINEERING SCAFFOLDS..... 65

4.1 Introduction..... 65

4.2 Experimental..... 68

4.2.1 Synthetic Procedures..... 68

4.2.2 Monomer and Polymer Characterization..... 69

4.2.3 Thermal Properties..... 71

TABLE OF CONTENTS
(Continued)

Chapter **Page**

4.2.4 Compression Molding..... 71

4.2.5 Melt Rheology..... 71

4.2.6 Mechanical Properties..... 71

4.2.7 Hydrolytic Degradation..... 72

4.2.8 Functionalizability..... 72

4.2.9 3D Printing of Scaffolds..... 73

4.2.10 Preparation of Scaffolds for Cell Culture..... 73

4.2.11 Cell Culture and Characterization..... 74

4.2.12 Statistical Analysis..... 76

4.3 Results and Discussion..... 76

4.3.1 Monomer and Polymer Synthesis..... 76

4.3.2 Thermal and Mechanical Characterization..... 77

4.3.3 Hydrolytic Degradation..... 79

4.3.4 Functionalizability..... 80

4.3.5 Rheological Characterization..... 83

4.3.6 3D Printing..... 84

4.3.7 Stem Cell Culture and Osteogenic Differentiation..... 85

4.4 Conclusions..... 88

5 3D PRINTING WAVY SCAFFOLDS FOR ENHANCED MSC OSTEOGENESIS 90

5.1 Introduction..... 90

TABLE OF CONTENTS
(Continued)

Chapter	Page
5.2 Materials and Methods	93
5.2.1 Scaffold Design	93
5.2.2 3D Printing of Scaffolds	95
5.2.3 Characterization of the Scaffolds	95
5.2.4 Preparation of the Scaffolds for Cell Culture	95
5.2.5 Cell Culture and Reagents	95
5.2.6 Cell Culture and Characterization	96
5.2.7 Statistics	98
5.3 Results	98
5.3.1 3D printing of PCL Scaffolds	98
5.3.2 Mechanical Tests	98
5.3.3 Growth Study	100
5.3.4 Differentiation Study	102
5.4 Discussion	105
5.5 Conclusions	109
6 SUMMARY, CONCLUSIONS, AND FUTURE WORK	111
APPENDIX A SUPPLEMENTARY DATA OF CHAPTER 2	114
APPENDIX B SUPPLEMENTARY DATA OF CHAPTER 3	116
APPENDIX C SUPPLEMENTARY DATA OF CHAPTER 4	118
REFERENCES	136

LIST OF TABLES

Table		Page
2.1	Line Test Results Showing the Range of Printed Strut Size (Diameter) with Respect to Print Speed and Extrusion Pressure, and Corresponding Needle Size for each Formulation	28
3.1	Composition, Corresponding Viscosities, and Autogelation Time of Tested Ink Formulations	52
4.1	Properties of the Polymers	77
4.2	Printing Parameters, including Needle Diameter (d), Print Temperature (T_p), Time to Equilibrate Temperature (t_e), Print Pressure (P), and Print Speed (v_p)	85
5.1	Design and Printing Parameters for the Scaffolds	94
C.1	The List of Results from Reactions between HP5GP and 1H,1H,2H,2H-perfluorodecanethiol	127

LIST OF FIGURES

Figure		Page
1.1	Different types of 3D printing technologies.....	4
1.2	Examples of currently available bioinks.....	7
1.3	Distinction between a bioink (left side) in which cells work as a mandatory component, and a biomaterial ink (right side), where a biomaterial is used to print a scaffold for cell seeding.....	9
1.4	The evolution of complex bioprinting: (A) 3D printing integrated with gel-casting; (B) 3D bioprinting with support materials; (C) unit-stacking approach; (D) coaxial bioprinting; (E) Freeform bioprinting; (F) Light-assisted bioprinting	13
2.1	Schematic showing the novel printing approach to create complex channels embedded within photocurable hydrogels, including sequential printing of a photocurable matrix hydrogel and a sacrificial hydrogel within freshly printed matrix hydrogel layer, followed by a post-printing process to remove the sacrificial hydrogel to create channels.....	25
2.2	Shear viscosity values with shear rate for MeAlg, MeHA, and Pluronic.....	26
2.3	Line test results for 15% MeHA (A) and 9% MeAlg (B) printed using a 0.21 mm diameter needle. 3D printed strut size (diameter) plotted against print-head speed for extrusion pressures equal to 483, 552, and 621 kPa, for MeHA, and 138, 207, and 276 kPa, for MeAlg.....	27
2.4	Rheological characterization of matrix hydrogel inks 9% MeAlg (A and C) and 15% MeHA (A and D). Time-sweeps were performed to investigate the evolution of elastic modulus (G'), viscous modulus (G"), and phase angle (Φ). Inks were tested for ~80 s, followed by partial crosslinking (15 s for MeAlg and 5 s for MeHA) with UV light, and fully crosslinking (240 for MeAlg and 90 s for MeHA), mimicking the channel printing process. Green boxes show the light exposure region.....	29
2.5	(A) Strut width (diameter), before (hydrogel strut) and after dissolution (channel) of sacrificial hydrogel with matrix (MeAlg) hydrogel, is plotted against print speed (mm/s) and pressure (psi). (B-C) Optical images of a representative strut before (B) and after (C) dissolution. (D-E) Representative confocal 3D scans of a strut (D) and a channel (E). In (D) rhodamine dye is mixed with Pluronic. In (E), the channel was injected with a solution containing rhodamine dye, and dye diffused out of the channel. Scale bars are 500 μm.....	30

LIST OF FIGURES
(Continued)

Figure **Page**

2.6 3D printed MeAlg hydrogel with two channels with varying channel sizes. (i) and (ii) showing the print speed and channel size values plotted against print length, corresponding to the channels in the top picture..... 31

2.7 Digital designs and corresponding 3D devices. (A) Linear channels with different sizes in a MeAlg matrix (10 x 10 mm) (channel sizes from left to right: 732 ± 6 μm, 481 ± 46 μm, 423 ± 23 μm, 367 ± 13 μm). (B) MeAlg matrix (10 × 10 mm) with 2 layers of linear channels (800 μm in diameter). (C) MeAlg matrix (18 × 16 mm) with converged channels (800-1200 μm). (D) Closed loop NJIT channel within MeHA hydrogel. (E) Injecting red dye into complex channels; (E) Top and side view of a hydrogel (16 × 14 × 4 mm) with 2 sets of channels (500 μm in diameter) at different x- and z-plane; (F) 3D printed wavy channels constant wavelength (8 mm) but increasing amplitude (2, 1, 0.5, and 0 mm). (G) Top and side view of a 3D printed device (30 × 20 mm) with 2 reservoirs (6 mm in diameter) connected with 2 channels (800 μm in diameter) embedded in MeAlg hydrogel. All channels were injected with red food coloring..... 33

2.8 Fluorescent images of the HUVECs cultured within channels (green showing F-actin and blue showing nuclei). (A) Maximum projection image from top. Cross-sectional (B) and top (C) view of the channels. Scale bars are 100 μm..... 34

2.9 (A) Confocal scanning microscopy images of hMSCs (green indicating live cells, and red indicating dead cells) bioprinted with MeHA and MeAlg hydrogels with and without channels and cultured for 1 day. (B-C) Corresponding % viability data for hMSCs cultured in MeHA (B) and in MeAlg (C) hydrogels for up to 4 days..... 35

3.1 Chemical structure, modification reaction, and crosslink mechanism of (A) NorCMC and (B) cCMC..... 52

3.2 Time sweep test of ink formulations without light exposure. (A-C) 10% NorCMC with thiol to norbornene ratio, (T:NB) equal to (1:4) (A), (1:2) (B), and 1:1 (C). (D-F) 15% cCMC with (T:NB) = 1:4 (D), 1:2 (E), and 1:1 (F)..... 53

3.3 Time sweep test of ink formulations under light exposure for: (A) NorCMC (1:4) and (B) cCMC (1:4). Green area denotes the UV exposure period..... 54

LIST OF FIGURES
(Continued)

Figure **Page**

3.4 (A) Compressive modulus (*E*) values of the 3D printed hydrogels from bioink formulations. $p<0.005$ for cCMC (1:2), as compared to the rest of the sample groups, and for NorCMC (1:2), as compared to the other groups. (B) The equilibrium swelling ratios values of the 3D printed hydrogels. $p<0.005$ for cCMC (1:4) and for NorCMC (1:2), as compared to cCMC (1:2) and NorCMC (1:2)..... 55

3.5 (A) Line test results for 15% cCMC, 10% NorCMC and 10% MeHA bioinks. Error bars denote standard deviation for $n \geqslant 5$. (B) Printability tests for 15% cCMC and 10% NorCMC for different (T:NB). The x-axis shows the elapsed time after mixing the crosslinker (DTT) with the ink formulation. Printability test result for 10% MeHA is given as a control..... 56

3.6 Pictures showing multi-material printing of thick (>3 mm in height) scaffolds. (A-B) Top (A) and side (B) views of NorCMC (1:2) scaffold printed with Pluronic (red). (C-D) Scaffold after Pluronic is dissolved in DPBS. (E-F) NorCMC (1:2) scaffolds printed with fast degrading cCMC (1:4) (red). Scale bars are 5 mm..... 57

3.7 (A) Plots showing % cell viability with culture time for cells (hMSCs, NIH 3T3 cells and HUVECs) cultured within bioprinted cCMC, NorCMC and MeHA hydrogels. * indicates the cCMC (1:4) sample group that degraded before Day 7. (B) Confocal fluorescent images of cells (hMSCs, NIH 3T3 cells and HUVECs) within bioprinted cCMC, NorCMC and MeHA hydrogels (green indicating live cells and red indicating dead cells). (Scale bars are 200 μm) For hMSC, $^{\alpha}p < 0.005$ cell viability for MeHA at Day 1 vs. at Day 4 and at Day 7, and at Day 4 vs. at Day 7; cell viability for cCMC (1:4) as compared to NorCMC (1:4) at Day 1; cell viability for NorCMC (1:2) as compared to MeHA at Day 7; $^{\beta}p < 0.0001$ NorCMC (1:4) vs. MeHA at Day 7. For NIH 3T3 cell line, $^{\alpha}p < 0.005$ cell viability for MeHA at Day 1 vs. Day 4 and Day 7; cell viability of MeHA as compared to NorCMC (1:2) and (1:4) at Day 1 and at Day 7; $^{\gamma}p <0.005$ for NorCMC at Day 1 vs. Day 7. For HUVECs, $^{\alpha}p < 0.005$ cell viability for NorCMC (1:4) and (1:2) at Day 1 vs. Day 7; cell viability for MeHA as compared to NorCMC (1:2) and (1:4) at Day 1. For all groups n=6..... 58

4.1 (A) Synthesis of HTy. (B) Synthesis of gluhexenamide. (C) Synthesis of glupentyamide..... 70

4.2 General polymer synthesis 70

LIST OF FIGURES
(Continued)

Figure **Page**

4.3 DSC thermograms for the polymers..... 78

4.4 Hydrolytic degradation of polymers over 25 weeks at 37 ˚C in DPBS. (A) Percent retained molecular weight (% Mw) with time. (B) Percent mass retention with time..... 79

4.5 (A) XPS spectra for HP5GH (green), HP reacted with 1*H*,1*H*,2*H*,2*H*-perfluorodecanethiol under UV light (red), and HP5GH reacted with 1*H*,1*H*,2*H*,2*H*-perfluorodecanethiol under UV light (blue). (B) QCM data showing the change in areal mass with time for HP5GH covered with BSA solution in the presence (+) or absence (-) of UV light..... 82

4.6 QCM data showing the change in frequency with time for HP5GP. Az-Heparin was flowed over HP5GP film for 60 min, followed by DPBS for 240 min, then BMP-2 for 100 min, and finally DPBS..... 82

4.7 Plots showing the change in storage modulus (G') and loss modulus (G") of the polymers with temperature (T). Solid to melt transition temperature is defined as the temperature where G'=G" 84

4.8 Top row: 3D printed scaffolds from PLA, HP, HP5BG, HP5GP, and HP5GH. The corresponding SEM images including from top view and cross-section are shown in middle and bottom row, respectively. Scale bars are 200 μm for SEM images..... 85

4.9 (A) Average peak intensities from alamarBlue cell viability assay for hMSCs cultured on scaffolds. (B) Average dsDNA quantities found within each scaffold group. Error bars represent the standard deviation (n = 6 and 3 samples/group for A and B, respectively). (C) Scanning fluorescent confocal 3D reconstructions of F-actin (green) and DAPI (blue) stained hMSCs cultured on the scaffolds for 14 days. Scale bars are 200 μm 86

LIST OF FIGURES
(Continued)

Figure **Page**

4.10 (A) Confocal images of hMSCs cultured on 3D printed scaffolds for 14 days in osteogenic differentiation media, and immunostained for human osteocalcin (OC) (green). Cell nuclei are stained with DAPI (blue). (B) Brightfield images of hMSCs stained for alkaline phosphatase (ALP, dark blue/purple) after 14 days of culture in osteogenic media. (C) Percentage of cells stained positive for OC corresponding to (A). For Day 14, #p<0.2 for Hep-BMP2 as compared to HP5GP and (+)Hep, #p<0.5 for Hep-BMP2 as compared to (+)BMP2. For Day 21, p<0.02 sBMP2 group as compared to HP5GP, (+)Hep, and (+)BMP2, and *p<0.4 for (+)Hep-BMP2 as compared to HP5GP and (+)Hep. (D) Percentage of cells stained positive for ALP corresponding to (B). *p<0.001 for (+)Hep-BMP2 as compared to other sample groups (n=3). (E) Alizarin Red (AR) staining quantification results using fluorometric analysis depicting AR concentration (mM) for each scaffold after 14 and 21 days of culture in osteogenic induction media..... 88

5.1 Wavy scaffold design containing 4 layers (left) and schematic showing the strut design for wavy scaffolds (right)..... 94

5.2 Images of the scaffolds. From the top to bottom row, images correspond to pictures (top view), micro-computed tomography (micro-CT) images (top view), scanning electron microscope (SEM) images, and SEM cross-section images. Scale bars are 500 μm for pictures and micro-CT images and 1 mm for SEM images..... 99

5.3 Young's modulus (*E*) values of the scaffolds for each scaffold design. * $p < 0.005$ for orthogonal vs. A05W2, A0.5W4, and A1W4; and for A0.5W4 vs. all sample groups..... 100

5.4 (A) AlamarBlue Assay (n=6); (B) PicoGreen Assay (n=3), *p<0.005 101

5.5 Multiphoton confocal images of the human mesenchymal stem cells (hMSCs) cultured on the scaffolds for seven days. Cells were stained for F-actin (red) and nuclei (blue). Scale bars are 200 μm..... 102

5.6 (A) Optical microscopy images of the hMSCs stained for alizarin red (red) after culture in osteogenic induction media for 21 days. Scale are 200 μm. (B) Alizarin red concentration indicating calcium deposition at Day 21. (* $p < 0.15$, ** $p < 0.05$, for $n = 3$) 103

5.7 ALP activity assay results for: (A) Day 14 and (B) Day 21 (* $p < 0.15$, ** $p < 0.05$, for $n = 3$) 104

LIST OF FIGURES
(Continued)

Figure **Page**

5.8 Multiphoton confocal images of hMSCs that are stained for vinculin (green) at Day 7..... 104

5.9 Multiphoton confocal images for hMSCs that were cultured in osteogenic induction media for 14 (top row) and 21 days (bottom row). Cells were immunostained for osteocalcin (green) and stained for F-actin (red) and cell nuclei (blue). Scale bars are 200 μm..... 105

A.1 ^{1}H NMR spectrum of methacrylated hyaluronic acid (MeHA) and methacrylated alginate (MeAlg). For MeHA, the functionalization was of ~90%, determined from the integration of the vinyl group (δ=5.8, 1 H and δ=6.25, 1 H) with respect to the HA backbone (δ=3.20-4.20, 10 H). For MeAlg, the functionalization was of ~72%, determined from integration of vinyl group (δ=5.8, 1H, and δ=6.25, 0.72 H) with respect to the hydroxyl group in alginate (δ=4.8-5.2 1H) 114

A.2 Line test results showing the strut width plotted against print speed and print pressure for (A) 0.08 mm, (B) 0.10 mm, and (C) 0.16 mm needle from top to bottom, respectively..... 115

B.1 ^{1}H NMR spectra of (A) cCMC and (B) NorCMC..... 116

B.2 Time sweep test of ink formulations under light exposure, (A) 10% NorCMC 1:2 and (B) cCMC 1:2. Green area denotes the UV exposure period..... 116

B.3 Time sweep test of cCMC (1:2) without pH adjustment..... 117

C.1 ^{1}H NMR spectra of HP..... 128

C.2 ^{1}H NMR spectra of HP5BG..... 129

C.3 ^{1}H NMR spectra of HP5GH..... 130

C.4 ^{1}H NMR spectra of HP5GP..... 131

C.5 Stacked ^{1}H NMR spectra for the polymers..... 132

C.6 Left: Young's modulus over time at 37 ˚C in DPBS; Right: Yield strength over time at 37 ˚C in DPBS..... 133

C.7 Graph of frequency change over time when az-Heparin, 2% SDS, and DPBS were flowed over a QCM crystal coated with HP5GP..... 134

LIST OF FIGURES
(Continued)

Figure **Page**

C.8 Young's modulus values of the 3D printed scaffolds..... 135

CHAPTER 1

INTRODUCTION

1.1 3D Printing Technologies for Tissue Engineering and Regenerative Medicine

Tissue engineering is a multidisciplinary field currently focused on two major areas: (i) developing new methods to repair, regenerate and replace damaged tissues and organs, and (ii) creating *in vitro* tissue models to better understand tissue development, disease development and progression, and to develop and screen drugs [1-6]. Despite recent advances in tissue engineering, there is a continuous lack of tissues and organs for transplantation and a shortage of tissue models for drug discovery and testing [7]. Conventional techniques, such as porogen-leaching, injection molding, and electrospinning, are generally recognized as the bottleneck due to limited control over scaffold architecture, composition, pore shape, size, and distribution [8-10]. 3D bioprinting is an emerging field enabling fabrication of scaffolds, devices, and tissue models with high complexity [9-12]. 3D printing allows the construction of tissues or scaffolds from commonly used medical images (such as X-ray, magnetic resonance imaging (MRI), and computerized tomography (CT) scan) using computer aided design (CAD). Custom and patient-specific design, on-demand fabrication, high structural complexity, low-cost, and high-efficiency are some of the major advantages of 3D printing, making it very attractive for medicine [13, 14].

Tissue engineering scaffolds are three-dimensional porous structures providing an infrastructure for cells to infiltrate, adhere, proliferate, and enabling new tissue formation for functional integration [1]. Scaffolds are generally required to display bioactivity to

instruct cellular behavior, such as adhesion, proliferation, migration, and differentiation [3]. In addition, control over composition, stiffness, degradation, and structural architecture are required as cells are responsive to their microenvironment [3, 15]. *In vitro* tissue models require the ability to fabricate cell only or cell-biomaterial platforms that mimic cellular organization (spatial distribution of multiple cell lines) and microenvironment (stiffness, structural topography, and biochemical cues) in relatively high resolution (25-100 μm) [2, 4, 5, 16, 17]. 3D printing has the potential to fabricate these complex platforms.

1.2 3D Bioprinting and 3D Printing of Biomaterials

Tissue engineering approaches require the fabrication of scaffolds using biomaterials or fabrication of living tissues using cells. 3D printed scaffolds can be utilized directly, allowing native cells to infiltrate and regenerate the tissue when implanted, or after seeded with cells. The printable material is referred as a "biomaterial ink." Currently available 3D printing technologies allow a wide range of biomaterials to be printed using diverse biomaterial ink formulations [13]. 3D printing technologies for biomaterial printing are classified under four main groups in this work: extrusion-based, droplet-based, powder-based, and vat photopolymerization-based printing. Extrusion-based printing technologies include fused filament fabrication (FFF) or known as under trademark fused deposition modeling (FDM), and direct ink writing (DIW). FDM utilizes synthetic thermoplastics and their composites with ceramics or metals [18]. For FDM, the form of the ink material is a filament, and it is extruded at elevated temperatures (140-250 ℃) in a melt state. Direct ink writing (DIW) allows extrusion of polymer melts, high viscosity solutions, hydrogels, and colloidal suspensions [19]. Inkjet printing is a droplet-based technology, and the

processing principle is the deposition of polymeric solutions and colloidal suspensions, with relatively low viscosities (< 10 cP (mPa.s)) at relatively high shear rates (10^5-10^6 s^{-1}) in the form of droplets (~50 μm in diameter) [20-23]. Selective laser sintering (SLS) utilizes metals, ceramics, polymers, and composites in powder form (10-150 μm in diameter). In this technique, a directed laser beam locally melts either directly the powder or a polymeric binder onto the bed surface [24]. Layers of fresh powder are continuously supplied after each layer is created. Binder jetting is another powder-based printing technology, which jets binder polymers to selectively bond powder materials into 3D green bodies, followed by infiltration or sintering to achieve final products [25]. The vat photopolymerization approaches require a viscous photocurable polymer solution or a prepolymer, which is exposed to a directed light (such as UV or laser) to spatially crosslink the solution [26].

Three dimensional bioprinting is a technology that allows the fabrication of living tissues/constructs from living cells with or without a carrier material [9-11, 27, 28]. The material that is printed is referred to as a "bioink", which can be defined as an ink formulation that allows the printing of living cells. 3D bioprinting process should be relatively mild and cell-friendly as it is required to allow cell printing [29]. This requirement limits the number of 3D printing techniques that are suitable for bioprinting. DIW allows the printing of cell suspensions and/or aggregates with or without a hydrogel carrier. Inkjet printing is another technology for cell printing. As compared to DIW, inkjet bioprinters are not readily available, yet there are commercially available inkjet print heads that are suitable for bioprinting [30, 31]. Vat photopolymerization-based 3D printing technologies, such as SLA, digital light processing (DLP), and continuous digital light

processing (cDLP), have emerged in printing live cells as long as a cell-laden prepolymer formulation is used and the photocuring takes place in a mild, cell-friendly condition, which are the two major issues for vat photopolymerization-based bioprinting [32-34]. In addition to these technologies, laser induced forward transfer (LIFT) is also shown to be suitable for bioprinting [35-40]. In this technique, an ink solution is coated onto a glass slide and coated with a laser absorption layer (metal or metal oxide). The laser is directed to the laser absorption layer with an ablation spot size between 40 to 100 μm in diameter [35, 37], creating a local pressure to eject the ink layer to the substrate.

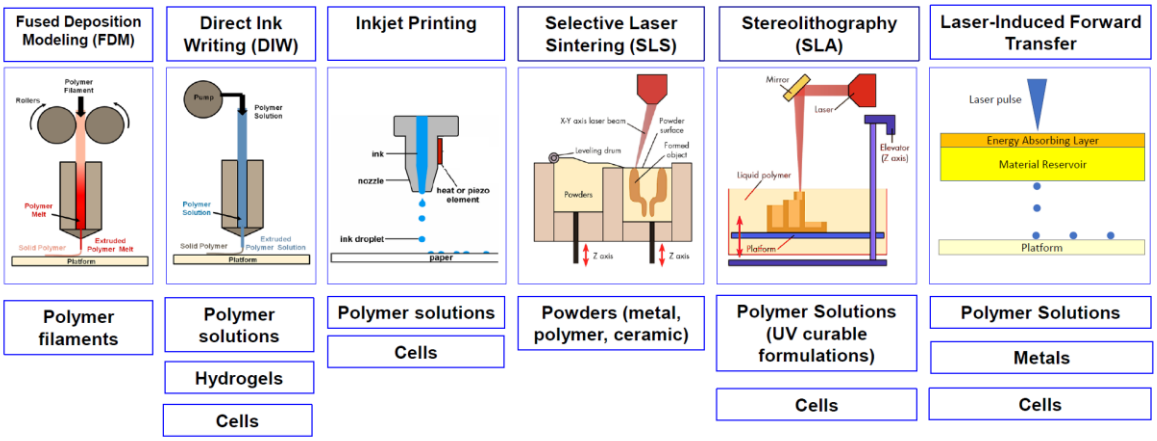

Figure 1.1 Different Types of 3D Printing Technologies.
Source: Adapted with permission [41], copyright 2016, American Chemical Society.

Among 3D printing techniques, extrusion-based printing is the most commonly used technology due to ease of use, availability, and low cost. In this regard, this dissertation is focusing on developing novel inks for extrusion-based biomaterial printing and bioprinting as well as developing novel bioprinting approaches using DIW bioprinting.

1.3 Currently Available Bioinks and Biomaterial inks

Noticeably, many of the biomaterial ink formulations are not suitable for cell printing. For instance, polycaprolactone (PCL) and poly(lactic acid) (PLA) are the most widely used biomaterials in 3D printing. However, they could only be printed at elevated temperatures in the form of a polymer melt, or when dissolved in organic solvents as a polymer solution. Therefore, they are not considered as bioinks, as both approaches are not suitable for live cell printing [42, 43].

Currently, cell-laden hydrogels (also known as scaffold-based bioinks) and cell-only bioinks (also known as scaffold-free bioinks) are the two major types of bioinks (**Figure 1.2**) [44-46]. Cell-laden hydrogels are particularly attractive due to their tunable properties and their ability to recapitulate the cellular microenvironment [47]. Cell-laden hydrogel bioink formulations utilize natural hydrogels such as agarose, alginate, chitosan, collagen, gelatin, fibrin, and hyaluronic acid, as well as synthetic hydrogels such as poly(ethylene glycol) (PEG) and its derivatives. Natural hydrogels offer inherent bioactivity (except for agarose and alginate) and display a structural resemblance to ECM. For instance, fibrin and collagen hydrogels with inherent filamentous structure display strain-stiffening property, mimicking the non-linear elastic behavior of the soft tissues in our body [48, 49]. Synthetic hydrogels permit but don't promote cellular function, yet there are many ways to tether bioactive cues into synthetic hydrogels [15]. When compared to natural hydrogels, synthetic hydrogels generally offer tunable mechanical properties. Many natural polymers (such as gelatin and hyaluronic acid) have functionalizable backbone side chains enabling them to be functionalized with chemical moieties to induce crosslinking (chemical- and/or photo-crosslinking) or additional bioactivity [50]. Blends of synthetic

and natural polymers have been used to develop mechanically tunable hydrogels with user-defined bioactivity. In addition, the mechanical properties and/or bioactivity can also be tuned by incorporating small amounts of nanoparticles into bioink formulation [51]. Derived from native tissues by removing the cells from the tissue while retaining the native extracellular matrix (ECM) ingredients, decellularized extracellular matrix (dECM)-based bioink formulations are an emerging field due to their inherent bioactivity and ease of formulation into a printable bioink [52, 53]. The compositions of dECM-based bioinks are more comprehensive than the others, which contains a tissue-specific complex composition of structural and functional ECM components of native tissue, such as collagen, glycosaminoglycans (GAGs), and growth factors [53-56]. This unique advantage makes dECM-based bioinks a good candidate for 3D bioprinting of tissue constructs [52, 57-59].

On the other hand, cell-only bioinks, including cell suspension, cell spheroids, and cell strands, are a viable option to create scaffold-free biological constructs [60, 61]. Modified inkjet printers have long been used to print cells into cellular assemblies. For instance, endothelial cells were printed from cell suspension (1×10^5 cells/ml) in growth media [62]. Bioprinting of scaffold-free constructs utilizes cell aggregates in the form of mono- or multi-cellular spheroids as a bioink [23, 63-65]. The bioink formulation undergoes fully biological self-assembly without or in the presence of a temporary support layer [63]. This technique relies on tissue liquidity and fusion, which allows cells to self-assemble and fuse due to cell-cell interactions [66-68]. Recently, due to the advantage of freeform bioprinting, pelleted cells were directly printed within a support bath in 3D structures [69].

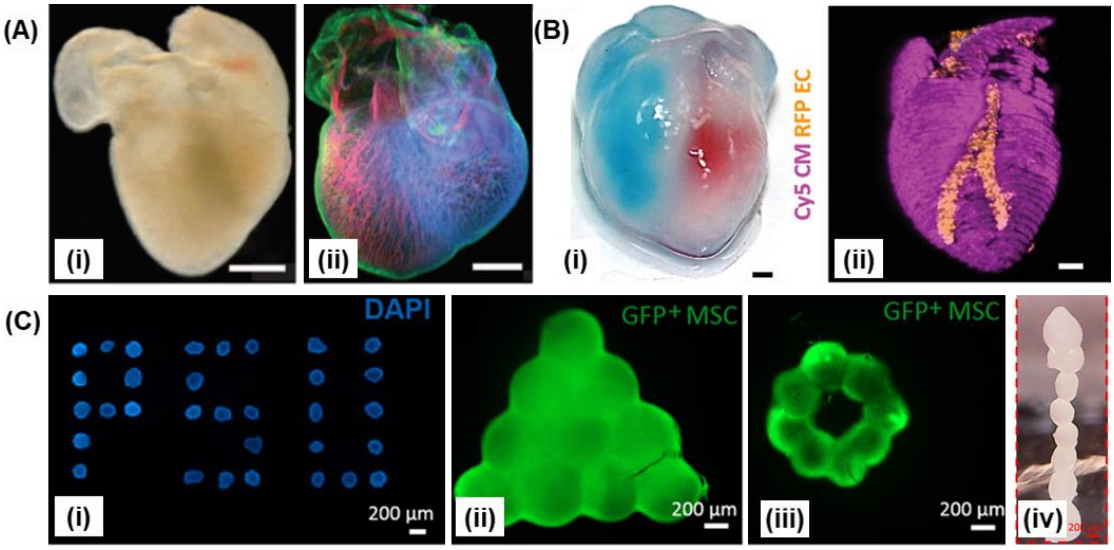

Figure 1.2 Examples of currently available bioinks: (A) an explanted embryonic chick heart bioprinted with cell-laden hydrogel: (i) darkfield image, and (ii) a confocal microscope image of the chick heart stained for fibronectin (green), nuclei (blue), and F-actin (red). (scale bar: 1 mm).; (B) A heart bioprinted with personalized cell-laden dECM-based hydrogel: (i) visualizing the left and right ventricles of the heart by injecting red and blue dyes, and (ii) a confocal image that visualized the bioprinted cardiomyocytes (pink), and endothelial cells (orange) (scale bar: 1 mm); (C) bioprinting of cell-only bioink (cell spheroids): (i) to (iii): bioprinted cellular patterns with cell spheroids, and (iv) stacking cell spheroids without supports.
Source: Adapted under the terms of the CC-BY 4.0 license [70]. Copyright 2015, the Authors. Published by American Association for the Advancement of Science.
Adapted under the terms of the CC-BY 4.0 license [59]. Copyright 2019, the Authors. Published by John Wiley and Sons
Adapted under the terms of the CC-BY-NC 4.0 license [71]. Copyright 2020, the Authors. Published by American Association for the Advancement of Science.

As to biomaterial inks, thermoplastic biomaterial inks, hydrogel inks, ceramic-based inks, and composite inks are currently available [41]. Thermoplastic biomaterials are the most commonly used in 3D printing of scaffolds, especially for desktop 3D printers, as a result of the ease to be processed, cost-effectiveness, biocompatibility, degradability, and mechanics. Thermoplastics could be engineered to be printed by extrusion-based (FDM and DIW), powder-based (SLS), and vat polymerization-based (SLA, DLP, cDLP) 3D printing techniques. Each of these techniques requires different material properties. For FDM and DIW at high temperatures, thermoplastics must render a rapid solid-to-melt

transition to secure melt formation pre-extrusion and solidification post-extrusion, whereas shear thinning properties of the melt are also required [18]. Specifically, for FDM, the value of the elastic modulus/melt viscosity should be lower than 5×10^5 s^{-1} to prevent filament buckling. In this regard, many thermoplastic biomaterials are available for high temperature FDM/DIW printing, including but not limited to PLA [72], PCL [73], polyether ether ketone (PEEK) [74], poly(butylene terephthalate) (PBT) [75], acrylonitrile butadiene styrene (ABS) [76], thermoplastic poly(urethane) (TPU) [77], and thermoplastic composite materials [78]. Unlike FDM, in which the ink must be in a filament form, DIW can print polymer solutions and hydrogels at low temperatures. The printable polymer solutions are typically comprised of volatile organic solvents, such as dichloromethane, chloroform, and tetrahydrofuran, which permits rapid dissipation within seconds after extrusion. Moreover, thermoplastic particles could be suitable for SLS, which requires the particle diameters in the range of 10-150 μm to permit good flowability and print resolution, and the melt viscosity should be low as well [79]. Finally, thermoplastics, such as poly(D,L-lactide) (PDLLA) [80] and poly(propylene fumarate) (PPF) [81], are also available for vat polymerization-based 3D printing (SLA, DLP, cDLP).

Hydrogel inks are also great candidates for DIW, which has been mentioned in the bioink sections. Besides, sacrificial hydrogels such as Pluronic F-127 (Pluronic) render excellent printability and fidelity, which is commonly used as support material during bioprinting processes [82]. Ceramic-based inks are also of great significance, especially for bone tissue engineering, due to their high stiffness and bioactivities [83]. Hydroxyapatite and tricalcium phosphates (TCP) are two major ceramic biomaterials used in bone tissue engineering. Due to the high melting point and processing difficulty, it is

convenient to mix ceramic biomaterials with polymers to formulate composite inks for 3D printing [84, 85]. Ceramic inks are also available to be printed in bulk forms by binder jetting of SLS [25, 86, 87]. As pure materials often fail to render all the desired properties, single material inks have been formulated with other materials as composite inks to enhance ink properties, which includes polymer-based, hydrogel-based, and ceramic-based composites. For instance, PCL could be supplemented by hydroxyapatite/TCP and growth factors to enhance the osteogenic function of the 3D printed scaffolds [88].

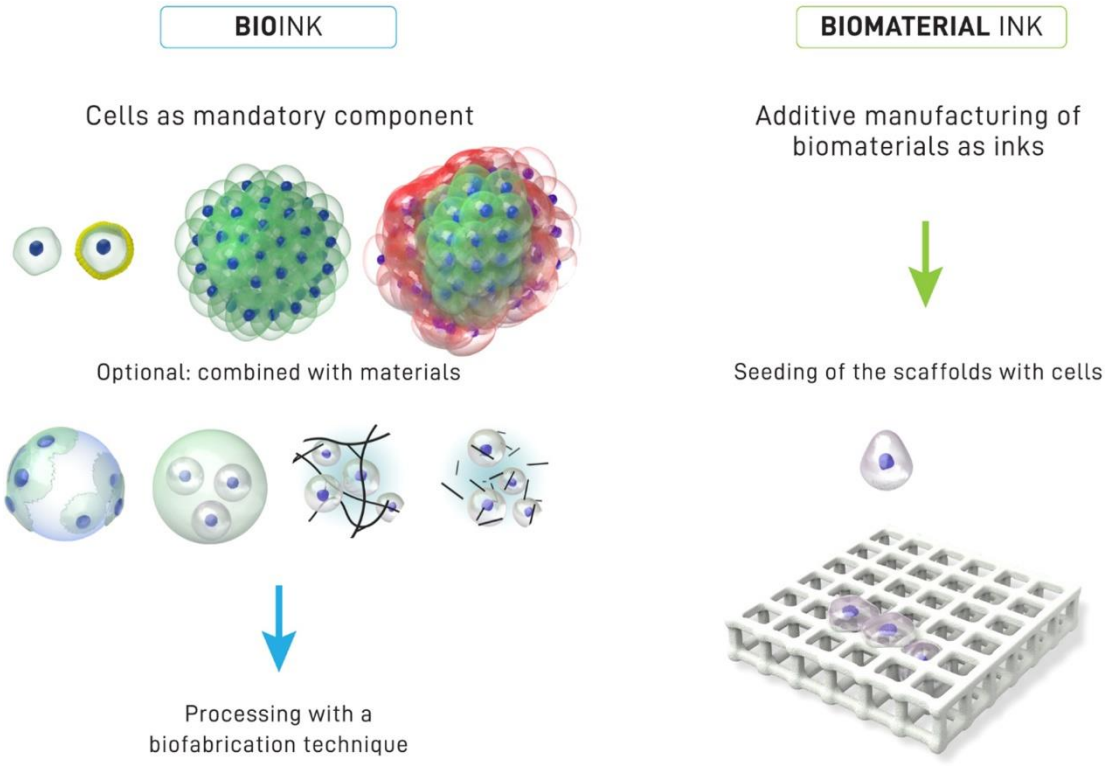

Figure 1.3 Distinction between a bioink (left side) in which cells work as a mandatory component, and a biomaterial ink (right side), where a biomaterial is used to print a scaffold for cell seeding.
Source: Adapted under the terms of the CC-BY 3.0 license [89]. Copyright 2018 IOP publishing.

1.4 Complex 3D Bioprinting

3D bioprinting technology already enabled the fabrication of small-scale tissues [5, 90, 91], and in the short-term, these bioprinted tissues could potentially address the lack of functional *in vitro* tissue/disease models for personalized medicine and drug screening. In the long-term, bioprinting show strong potential to address the shortage of implantable organs [27, 92]. To achieve these short- and long-term goals, it is crucial to capture the architectural, structural, mechanical, and biochemical complexity of the native tissue. This requires the bioprinting process to evolve from small-scale, low-resolution, single or dual cell and biomaterial printing to human-scale, high-resolution, multi-cellular, and multi-biomaterial printing [93-95]. For complex 3D bioprinting, two aspects of complexities of the printed tissue/organ constructs are usually considered to resemble *in vivo* conditions, including the tissue architecture and the physical (stiffness) and biochemical (cells and bioactive cues) complexity. Due to layer-by-layer fabrication, 3D printing of complex architectures such as tubular and spiral as well as hollow structures (such as embedded channels for vascularization) is limited. Native tissues are multicellular that compromise many cell types, which requires the ability to formulate and bioprint multiple cell types while maintaining their phenotype or derive them into site-specific lineages. To resemble the physical and biological complexity, it is crucial to place a multitude of bioinks within a 3D space allowing precise distribution of multiple cell types and ECM mimetic materials. Besides, the fabrication of vascular networks that are embedded within the bioprinted tissues is one of the key issues to achieve large-scale bioprinting, as vasculature is crucial for nutrient supply and waste removal to overcome mass transfer limitations [96, 97].

Recent advances in bioprinting technology and bioink development enabled to

overcome some of the abovementioned issues (**Figure 1.4**). For instance, 3D printing integrated with gel-casting is one of the widely used strategies for the fabrication of channel structures embedded within 3D cell-laden hydrogels (**Figure 1.4A**) [98-104]. This approach includes mold fabrication, 3D printing of sacrificial structures within the mold, hydrogel precursor solution casting into the mold followed by hydrogel crosslinking, and finally removal of the sacrificial structure. Another convenient approach is 3D bioprinting with support materials (**Figure 1.4B**) [52, 58, 82, 105-107]. By printing a sturdy framework of support material along with the bioinks, the bioprinted tissue construct becomes self-supportive. The support ink can be a sacrificial hydrogel such as Pluronic, which can be removed after printing, or a thermoplastic (such as PCL and polyurethane (PU)) that can remain to provide mechanical stability for the bioprinted structure both *in vitro* and in vivo. In addition, the approach is efficient for bioprinting straight tubular structures in macroscale (**Figure 1.4C**). In the unit-stacking approach, cell-laden hydrogels are bioprinted as cylinders or spheroids, which serve as the building units that can be stacked into the desired shape or a construct [63, 108-112]. Moreover, Coaxial bioprinting is suitable for the continuous fabrication of tubular structures (**Figure 1.4D**). The key feature of coaxial bioprinting is the 2-layered nozzle, which enables co-extrusion of two different bioink formulations in a core-shell manner [113-115]. Due to the ease of direct bioprinting of tubular channels, researchers formulated endothelial cell-laden bioactive bioinks to fabricate thick, vascularized, functional tissues [57, 116-120], and recent studies showed coaxial bioprinting of heterogenous and hallow filaments enabling fabrication of complex tissue constructs [121-124]. However, the layer-by-layer printing process significantly limits the achievable complexity of the microstructures and 3D anisotropy as well as the

ability to print tissue mimetic soft hydrogels (elastic modulus below 100 kPa) or cells alone. Freeform extrusion-based bioprinting overcomes these issues by eliminating the need for layer-by-layer fabrication and enabling omnidirectional freeform fabrication (**Figure 1.4E**) [125]. In this approach, DIW is performed within a support bath which physically supports the printed structure. The ink is extruded out of a needle-like nozzle that moves through a support bath, deposited within the bath, and held in place [59, 70, 126-130]. Last but not least, vat photopolymerization-based printing approaches have gained recent attention due to their ability to create support-free complex structures and omnidirectional printing (**Figure 1.4F**). In particular, light-assisted printing using projection, including DLP and cDLP, attracted more interest due to enhanced print speed as compared to SLA [34, 131-144].

Although the abovementioned techniques enable complex bioprinting, yet there is still more to accomplish to achieve the fabrication of fully functional, human-scale, and highly-complex tissues and organs.

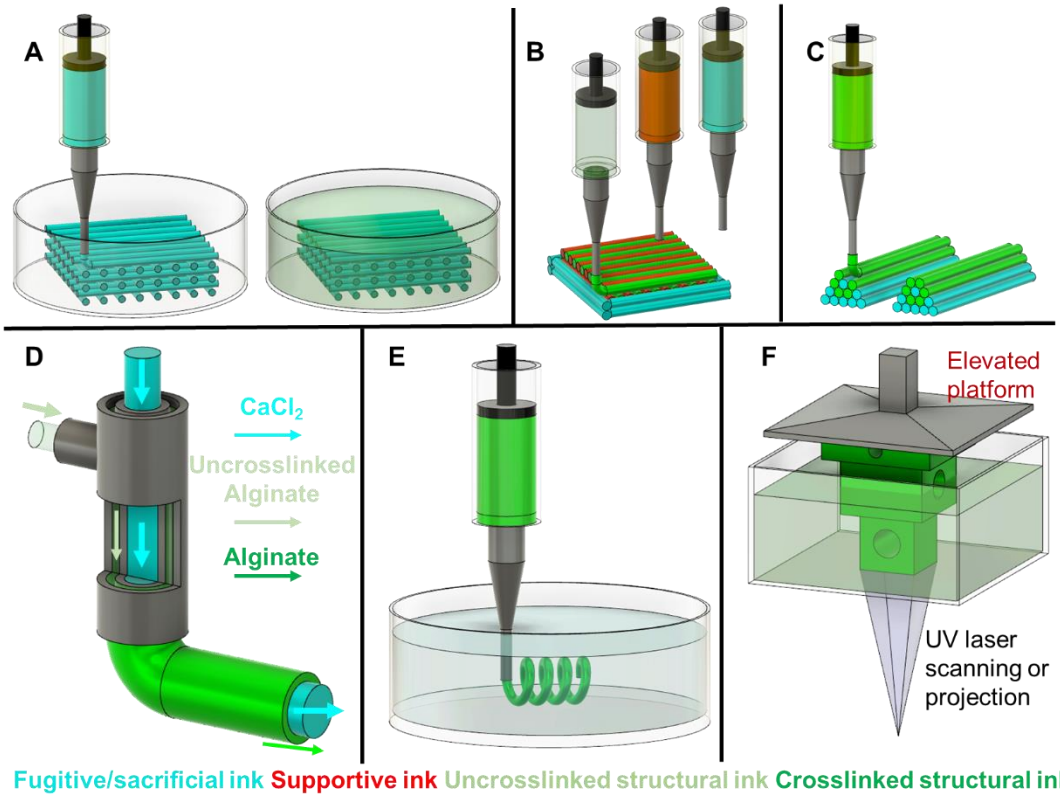

Figure 1.4 The evolution of complex bioprinting: (A) 3D printing integrated with gel-casting; (B) 3D bioprinting with support materials; (C) unit-stacking approach; (D) coaxial bioprinting; (E) Freeform bioprinting; (F) Light-assisted bioprinting.

1.5 Objectives

In this dissertation, two main objectives are presented:

Objective 1. To develop a novel bioprinting approach to create complex microchannels within cell-laden hydrogels.

Objective 2. To extend the range of available inks for tissue engineering applications

Objective 2.1. To develop novel bioinks from UV-responsive norbornene-functionalized carboxymethyl cellulose macromers

Objective 2.2. To develop a functional polyester-based ink platform with the potential for tunable bioactivity

1.6 Dissertation Organization

In Chapter 2, a novel 3D bioprinting approach is developed to create complex microchannels within cell-laden hydrogels, which utilized photocurable and sacrificial hydrogels.

In Chapter 3, novel bioinks from UV-responsive norbornene-functionalized carboxymethyl cellulose macromers are developed, where the formulation, rheological properties, printability/printing process, and cell viability were investigated.

In Chapter 4, a novel functional polyester-based ink platform with tunable bioactivity was developed, which has promising rheological, mechanical, and biological properties towards 3D printing of tissue engineering scaffolds for bone regeneration.

In Chapter 5, 3D porous scaffolds with wavy or linear patterns were printed to investigate the effect of wavy scaffold architecture on hMSC osteogenesis.

In Chapter 6, the summary and conclusion of this dissertation are provided. And the future work directions are envisioned.

CHAPTER 2

3D BIOPRINTING OF COMPLEX CHANNELS WITHIN CELL-LADEN HYDROGELS

This chapter has been adapted from the publication:
S. Ji, E. Almeida, M. Guvendiren, 3D bioprinting of complex channels within cell-laden hydrogels, Acta Biomaterialia 95 (2019) 214-224.

2.1 Introduction

The advances in additive manufacturing technologies enabled the fabrication of complex 3D scaffolds and medical devices [9, 27, 28, 82, 145, 146]. To fabricate clinically relevant and human scale tissue and organs, development of 3D constructs with vascular networks is one of the major bottlenecks [96, 147-149]. Thus, there is a growing demand for novel approaches to create perfusable microchannels, with tunable sizes and shapes, within 3D printed hydrogel constructs. Hydrogel constructs with embedded microchannels are also essential for the development of organ-on-a-chip systems for fundamental studies relating to tissue development and disease, and potentially be useful for drug testing [150].

Besides 3D bioprinting, various approaches were reported to fabricate tubular vessels, porous constructs, and microchannels to develop vascular structures, including solvent-casting and particulate leaching [151-153], gas foaming [154], fiber bonding [155], phase separation [156, 157], electrospinning [158], and self-assembly/healing [159, 160]. Yet, 3D bioprinting offers many advantages, including precise control of channel size, shape, and location (within the construct), and the ability to print multiple-materials including cells and cell-laden hydrogels [161].

In the past decade, several strategies have been developed to create microchannels within 3D printed constructs. Gel-casting on a 3D printed sacrificial network is a convenient approach to fabricate embedded microchannels within hydrogels [98-101]. In

this approach, a curable hydrogel solution is casted on a 3D printed sacrificial template (scaffold) using a mold. A wide range of sacrificial ink materials have been used (agarose, gelatin, Pluronic, and sugar-based materials) to create microchannels [98-100, 162-164]. For example, Miller et al. reported the use 3D printed sugar-based inks to fabricate sacrificial (e.g., water-soluble) templates (scaffolds), and were able to fabricate a range of constructs (from curable hydrogels) with embedded channels, with diameters ranged from 150 μm to 800 μm [98]. Lewis group utilized a similar approach to fabricate hydrogels with vascularized, perfusable channels (using water-soluble Pluronic) that can support encapsulated cell growth for more than 6 weeks [100]. Although this approach is shown to be efficient in creating embedded microchannels within hydrogels, it is almost impossible to place channels at a user-defined height unless multiple printing (of sacrificial material) and gel-casting steps are introduced. Another approach is free-form bioprinting, which refers to direct printing of a material (e.g., hydrogel ink) into a support bath (e.g., hydrogel) using extrusion-based printing [70]. In this approach, the support bath can be filled either with a sacrificial material, in which case it will be removed after the printing of a matrix material, leaving out a self-supporting matrix, or with a stable matrix material, in which case a sacrificial material is printed within and removed after printing to create channels [70, 130, 165-169]. Independent of the particular approach (i.e., self-supporting matrix printing within support material or channel printing within matrix material), the bath material has to allow the needle motion during printing. In this regard, highly viscous polymer slurries, salt solutions, shear-thinning hydrogels, and micro-gels have been utilized [70, 130, 165-168]. This requirement significantly limits the number of available materials for this approach. In addition to extrusion-based printing, vat

photopolymerization printing was also utilized. Stereolithography was used to spatially cure photocurable hydrogels within vat to create embedded channels within hydrogels [132, 170-172].

In addition to the abovementioned approaches, “unit stacking” and “co-axial printing” approaches have also been utilized to develop vessels (or hollow tubes). In the unit stacking approach, cell spheroids were loaded in agarose hydrogel and printed to form a filament and supported by agarose only filaments. This technology enabled the fabrication of small vessel tubes that are 0.9-2.5 mm in diameter [63]. Byambaa et al. utilized “unit stacking” approach using GelMA hydrogels [112]. In this method, each GelMA strut is printed individually layer-by-layer on the building plane. To form channels, a sacrificial ink is printed, using a secondary print head, to replace one of the GelMA struts. This is the most commonly used bioprinting approach in the literature to fabricate channels. The advances in additive manufacturing technologies enabled the fabrication of complex 3D scaffolds and medical devices [9, 27, 28, 82, 145, 146]. To fabricate clinically relevant and human scale tissue and organs, the development of 3D constructs with vascular networks is one of the major bottlenecks [96, 147-149]. Thus, there is a growing demand for novel approaches to create perfusable microchannels, with tunable sizes and shapes, within 3D printed hydrogel constructs. Hydrogel constructs with embedded microchannels are also essential for the development of organ-on-a-chip systems for fundamental studies relating to tissue development and disease and potentially be useful for drug testing [150].

Although many approaches have been developed (as summarized above), there is still a need for novel approaches that are easily applicable, allowing the use of commercially available bioinks and desktop bioprinters to create user-defined and tunable

microchannels within 3D hydrogels. In this study, we address this gap. Here, a novel bioprinting approach is presented that enables 3D printing of user-defined and highly tunable channels (shape, size, and location within matrix hydrogel) embedded within a photocurable hydrogel matrix. In this approach, a photocurable hydrogel ink was printed layer-by-layer as usual, but partially photocrosslinked (for seconds) after the printing of each layer to allow self-supporting viscous construct. When the desired height was reached, the final matrix hydrogel layer was not exposed to light and s sacrificial hydrogel (Pluronic) was directly printed within this layer. The layer was then exposed to light to partially crosslink the matrix hydrogel and to confine Pluronic. This process was repeated as needed. Once the printing of the construct was finalized, it was exposed to light (minutes) to fully crosslink the construct and immersed in an aqueous solution to remove the sacrificial ink to form channels. Here, an important advance is reported as this approach does not require complex device modifications for bioprinters or complex synthesis and processing hurdles for the inks. It is also a reservoir and mold free (utilizes low amount of material) and allows flexibility to place channels at any height within the matrix. This approach allows bioprinting of cells with the matrix material and seeding of cells into channels after the sacrificial ink is removed. It could be envisioned that this approach can provide a robust platform for fabricating vascularized tissues and studying cell behaviors on diverse channel surfaces and will enable wide-spread use of bioprinting to create microchannels within hydrogels.

2.2 Materials and Methods

2.2.1 Polymer Synthesis

Methacrylated alginate (MeAlg) and methacrylated hyaluronic acid (MeHA) were synthesized by esterification of the hydroxyl group with methacrylic anhydride, following already established protocol [173, 174]. Briefly, 1 % (m/v%) polymer solution was prepared by dissolving 3 grams of low viscosity alginate (Alg, Alginic acid sodium salt from brown algae, Sigma) or sodium hyaluronate (HA, 60 kDa, Lifecore) in 300 mL deionized water in a three-neck flask. The solution was stirred and kept at ~1-4 ℃ in an ice bath. Subsequently, a 2M NaOH solution was used to adjust the pH of the polymer solution to 8-9. Then, 6 mL of methacrylated anhydride (MA, Sigma) was added dropwise to the 1% polymer solution, while 4M NaOH was simultaneously added to maintain the pH at 8-9. The whole amount of the MA was consumed with a span of 1.5~2 hours. After the addition of the MA, the pH was maintained by gradually pipetting 4M NaOH solution for 8 hours using an automated pH controller. The solution was kept at 4 ℃ overnight. The reaction was resumed the following day by adding 3mL of MA while maintaining the pH at 8-9. The material was then dialyzed (Spectra/Por®1 dialysis membrane, 6-8 kDa) against DI water for 4 days, followed by lyophilization. The percent modification was characterized using ^{1}H NMR.

2.2.2 Ink Preparation

Ink formulations were prepared by dissolving MeHA (or MeAlg) at different concentrations in phosphate-buffered saline (DPBS) in the presence of a photoinitiator (405-410 nm), lithium phenyl-2,4,6-trimethylbenzoylphosphinate (LAP). For instance, to prepare a 9% MeAlg, 0.001 g of LAP was dissolved in 2 ml of DPBS in a glass vial covered

with an aluminum foil. 0.18 g of MeAlg was then added into the solution, and the solution was stirred overnight at room temperature. Considering the previous reports [165], three different concentrations were used for MeAlg (5%, 7% and 9% (w/v)) and for MeHA (5%, 10%, and 15% (w/v)). Sacrificial ink, Pluronic F-127 (Sigma), was prepared by dissolving 4 g Pluronic in 10 ml of deionized water (40% (w/v) final solution) at 4 °C overnight.

To prepare cell-laden ink, 1 ml of 18% MeAlg (or 30% MeHA) was mixed with 20 μL RGD peptide (50 mg/mL, GRGDSPC - GenScript) and incubated at room temperature (RT) for 30 min. Then, the solution was mixed with 1 mL of cell suspension (hMSC, 2×10^6 cells/mL) under magnetic stirring, leading to a final concentration of 9% MeAlg (or 15% MeHA). Each ink formulation was transferred into a designated 10 mL syringe prior to printing.

2.2.3 Rheological Characterization of Ink Formulations

Malvern Ultra+ Rheometer was used to analyze the rheological properties of the ink formulations. All of the tests were performed using a flat plate geometry (20 mm) at 25 °C. For viscosity measurement, the shear viscosity was measured at shear rates from 0.01 to 1000 s^{-1}. Time sweep tests were done at a frequency of 1 Hz and an oscillatory strain of 0.05 to investigate the change in elastic modulus (G'), viscous modulus (G''), and phase angle (Φ). To investigate the evolution of the abovementioned rheological parameters during the 3D printing process, inks (9% MeAlg or 15% MeHA) were injected onto the lower plate of the rheometer, and time sweep tests were performed using a UV light apparatus (Malvern) connected to a UV light source (Omnicure S2000, 356 nm, 40 mW/cm^2). Light intensity was adjusted to compensate for the difference in the wavelength of the printer light source (405 nm) according to the molar absorptivity

spectrum of the photoinitiator (LAP) [175]. The ink was exposed to UV light in a stepwise manner mimicking the partial crosslinking (240 s for 9% MeAlg, 5 s for 15% MeHA) and fully crosslinking (15 s for 9% MeAlg, 90 s for 15% MeHA).

2.2.4 Printer Parameter Optimization (Line Test)

Ink formulations were used to print individual struts (lines) on a methacrylated glass slide at different pressures and speeds. The images of struts were captured by a microscope. Three random parts of each strut (from three samples per each group) were captured for analysis. The strut diameter was measured using ImageJ.

2.2.5 Scaffold Design

3D scaffold designs were created by Autodesk® Fusion 360™ and sliced with Slic3r in Repetier-Host to generate G-code files. For scaffolds with embedded channels, the matrix and the channel structures were sliced separately. The G-code file for the channel design was then incorporated into the G-code file for the matrix design.

2.2.6 Preparation of Methacrylated Glass Slides

In this study, surface modified glass slides (microscope slides) were used as the print substrate. The glass slides were modified with methacrylate as described previously [176]. Briefly, glass slides were first washed with DI water, then immersed in a 10M NaOH solution for 10 minutes. Subsequently, the glass slides were removed and washed with DI water, and dried. Glass slides were placed in a glass baking pan, and the surface of the glass slides were covered with 3-(Trimethoxysilyl)propyl methacrylate (TMS, Sigma) solution. After sealing the top of the pan with aluminum foil, the pan was put into an oven at 100 °C for 1 hour. After 1 hour, the temperature was increased to 110 °C for another 10 minutes. The glass slides were then washed with ethanol and rinsed with DI water and dried.

2.2.7 3D Printing of Sacrificial Hydrogel within the Matrix Hydrogel

A novel approach was developed to 3D print vasculature within cell-laden hydrogels. Our approach utilizes 3D printing of a sacrificial hydrogel (or polymer) within the freshly printed matrix layer. Our approach is summarized in **Figure 2.1**. Briefly, the matrix ink (MeHA or MeAlg) was printed layer-by-layer as usual. After each layer, the construct was exposed to light to partially cure the printed matrix hydrogel (405 nm, 40 mw/cm^2, 15 s for 9% MeAlg and 5 s for 15% MeHA), which formed a self-supporting layer. Each layer was usually in the range of 500-600 μm but adjusted by adjusting the print speed or pressure of the matrix ink. When the desired matrix thickness was reached, one additional layer was printed, but it wasn't exposed to light. The sacrificial ink was printed directly within this viscous layer, and the system was exposed to light. This process was repeated as required to complete the printing process. Once the printing of the desired construct was completed, the system was exposed to a final light exposure to fully crosslink the construct (405 nm, 40 mw/cm^2, 240 s for 9% MeAlg and 90 s for 15% MeHA). The construct was then immersed in an aqueous media (i.e., DPBS) to dissolve the sacrificial ink and form channels. A wide range of print speed and pressure was used for sacrificial hydrogel printing to investigate the effect of these parameters on strut size. The sacrificial matrix strut size was measured prior to the dissolution of the matrix, and the results were compared with the measured channel diameter. Channels were injected with red food coloring for visual clearance. Three random parts of each strut/channel (from three samples per each group) were captured for analysis. The strut/channel diameter was measured using ImageJ.

2.2.8 Cell Culture and Characterization

Human mesenchymal stem cells (hMSCs, passage 4, Lonza) were cultured in the growth media (α-MEM (minimum essential medium) supplemented with 10% fetal bovine serum (FBS, Gibco) and 1% penicillin-streptomycin (Gibco)). For hMSC-laden bioink studies, two scaffold groups were printed including scaffolds with channels and without channels (control group). Scaffolds were cultured for 4 days, and live-dead staining was done at Day 1 and Day 4 time points. For live-dead staining (Invitrogen), cells were stained with calcein-AM ("live", 0.5 μL/mL) and ethidium homodimer ("dead", 2 μL/mL) for 30 minutes. Samples were immediately transferred to confocal laser scanning microscope (confocal and 2-photon scanning microscope, Leica) after staining to capture 3D scans. Three samples per group was prepared for viability studies. The viability was calculated by counting cells using ImageJ.

Human umbilical vein endothelial cells (HUVECs, Lonza) were cultured for cell attachment studies on the channel surfaces. According to the vendor's protocol, HUVECs were cultured in EGM-2 media (EGM-2 BulletKit, Lonza). Media was changed every two days to ensure a proper cell proliferation. Cells with 4-6 passage number were used in this study. Prior to the seeding process, the channels were injected with fibronectin (Invitrogen) solution (50 μg/mL) to enhance cell attachment. Cell suspension (3×10^7 cells/ml) was injected into the channels using a micropipette (0.1-10 μL tip). Scaffolds were then incubated at 37 ºC for 2 h, during which the scaffolds were flipped every 30 min. Scaffolds were then cultured for 7 h (during which they were flipped back one more time after the first 2 h), followed by culture on an oscillating shaker at a frequency of 1 Hz. The non-adherent cells were flushed out of the channels by gently pipetting the media. The media

was changed every two days. The cell culture studies were performed in an incubator maintained at 37 ºC under 5% CO_2. Cells in the channels were observed with a fluorescent microscope. At Day 14, the channels were gently flushed with DPBS (3X), and cells were fixed with 4% formaldehyde. Cells were permeabilized with 0.25% Triton-X (Sigma) and stained with Alexa Fluor™ 488 Phalloidin (Invitrogen) and with DAPI (Sigma) for F-actin and nuclei, respectively.

2.2.9 Statistical Methods

If not stated specifically, three samples per each group were used for all studies. The data were analyzed using KaleidaGraph. Data are presented as mean ± standard deviation. ANOVA with Tukeys HSD post hoc test of means was used to make comparisons between sample groups.

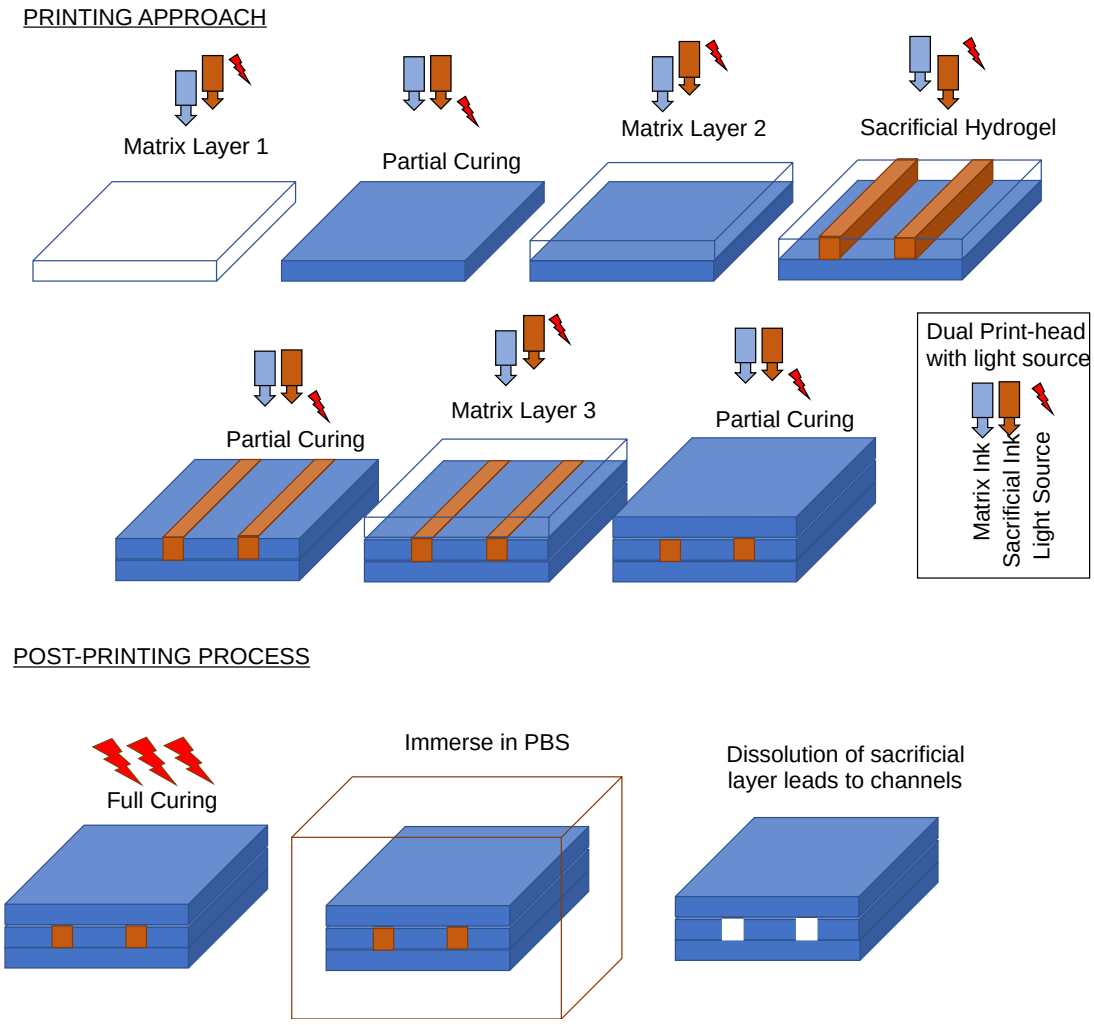

Figure 2.1 Schematic showing the novel printing approach to create complex channels embedded within photocurable hydrogels, including sequential printing of a photocurable matrix hydrogel and a sacrificial hydrogel within freshly printed matrix hydrogel layer, followed by a post-printing process to remove the sacrificial hydrogel to create channels.

2.3 Results

2.3.1 Preparation and Characterization of Inks

Ink formulations were prepared from MeAlg and MeHA, with 90 % and 72 % methacrylation, respectively (**Appendix A, Figure A.1**). Based on the literature [165, 177], three compositions per each polymer is selected: 5%, 7%, and 9% (w/v) for MeAlg, and 5%, 10%, and 15% (w/v) for MeHA. Pluronic (F-127) was used as a sacrificial ink (40%

(w/v)) [99]. The change in ink viscosity with shear rate for each formulation is shown in **Figure 2.2**. Viscosity of the ink formulations significantly increased with increasing polymer concentration for both MeAlg and MeHA. Shear thinning behavior (i.e., decrease in viscosity with increasing shear) is observed for MeAlg formulations, 15% MeHA ink and sacrificial ink. The viscosity values of MeAlg inks were significantly higher than that of MeHA (except for 15% MeHA, which has a viscosity similar to 5% MeAlg), despite the fact that MeHA inks had much higher polymer concentrations.

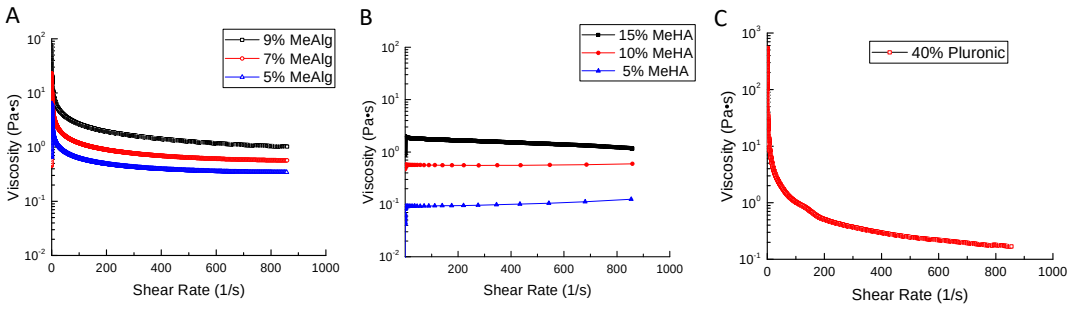

Figure 2.2 Shear viscosity values with shear rate for MeAlg, MeHA, and Pluronic.

2.3.2 Line Tests Results for Matrix Hydrogel Inks

Line tests were performed on methacrylated glass slides to determine the optimal printing parameters (print speed and pressure) for selected needle-sizes (0.21 and 0.30 mm in diameter). For instance, line test results for 9% MeAlg and 15% MeHA showing the printed strut size (μm) with print speed (mm/s) for three different print pressures (kPa) are given in Fig. 3. For MeHA inks, the strut size significantly increased with increasing pressure for each print speed. For instance, strut size increased from 600 μm, for 138 kPa (20 psi), to 900 μm, for 207 kPa (30 psi), and to 1150 μm, for 276 kPa (40 psi). Strut size decreased with increasing speed. When struts printed at

6 mm/s are compared with 10 mm/s, strut size decreased from 1150 to 900 μm, for 276 kPa; 900 to 700 μm, for 207 kPa; and 650 to 500 μm, for 138 kPa. For 9% MeAlg, there was no significant change in strut size with pressure, but the strut size decreased gradually with increasing speed. Line test results for all of the ink formulations are given in **Table 2.1**.

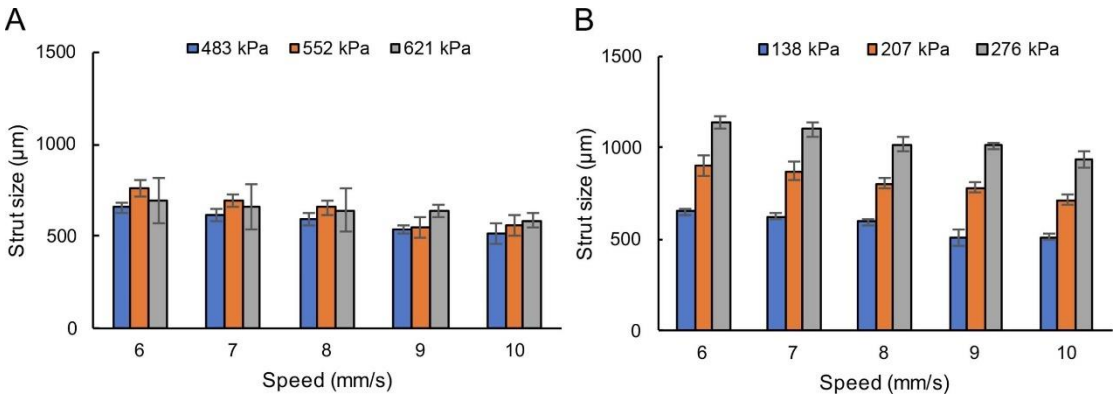

Figure 2.3 Line test results for 15% MeHA (A) and 9% MeAlg (B) printed using a 0.21 mm diameter needle. 3D printed strut size (diameter) plotted against print-head speed for extrusion pressures equal to 483, 552, and 621 kPa, for MeHA, and 138, 207, and 276 kPa, for MeAlg.

Table 2.1 Line Test Results Showing the Range of Printed Strut Size (diameter) with Respect to Print Speed and Extrusion Pressure, and Corresponding Needle Size for Each Formulation

Ink formulation		Needle size	Print speed	Pressure	Strut size
Hydrogel	% (w/v)	(mm)	(mm/s)	(psi)	(μm)
MeAlg	5	0.21	10-30	5-15	300-1400
	5	0.30	10-30	5	800-1400
	7	0.21	10-30	10-30	250-1100
	7	0.30	10-30	5-15	350-1400
	9	0.21	6-10	20-40	500-1100
	9	0.30	10-30	10-20	500-1500
MeHA	5	0.21	6-10	3-8	400-1000
	5	0.30	NP*	-	-
	10	0.21	6-10	10-30	400-700
	10	0.30	6-10	5-15	300-1100
	15	0.21	6-10	70-90	500-800
	15	0.30	6-10	90	600-1300

*: Not printable (NP)

2.3.3 Rheological Properties of the Printed Matrix Hydrogels

The evaluation of elastic modulus, viscous modulus, and phase angle was investigated using time sweep tests for 9% MeAlg and 15% MeHA (**Figure 2.4**). Green boxes in the figures show the light exposure periods, corresponding to partial crosslinking period (15 and 5 s for MeAlg and MeHA, respectively) and complete crosslinking period (240 and 90 s for MeAlg and MeHA, respectively). Our results showed that both formulations gelled

during the partial crosslinking period, and gelation progressed further during the complete crosslinking period.

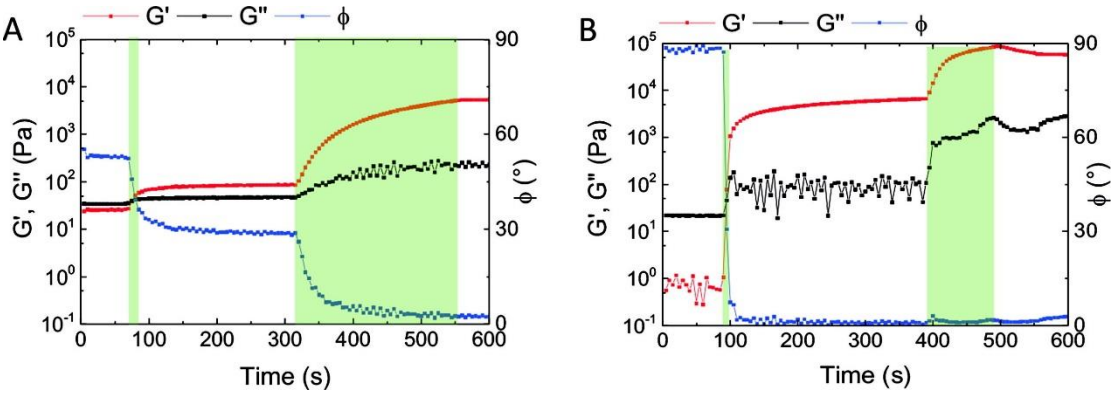

Figure 2.4 Rheological characterization of matrix hydrogel inks 9% MeAlg (A and C) and 15% MeHA (A and D). Time-sweeps were performed to investigate the evolution of elastic modulus (G'), viscous modulus (G"), and phase angle (Φ). Inks were tested for ~80 s, followed by partial crosslinking (15 s for MeAlg and 5 s for MeHA) with UV light, and fully crosslinking (240 for MeAlg and 90 s for MeHA), mimicking the channel printing process. Green boxes show the light exposure region.

2.3.4 Line Tests Results for Sacrificial Hydrogel Ink

Line tests for sacrificial ink were done on methacrylated glass slides (**Appendix A, Figure A.2**) and within matrix (MeAlg and MeHA) hydrogels (**Figure 2.5**). In general, strut size increased with increasing needle size. For instance, when printed at 4 mm/s and 414 kPa pressure, strut size was 85 μm for 0.08 mm needle, 300 μm for 0.10 mm needle, and 400 μm for 0.16 mm needle. Struts size increased with increasing pressure at a constant speed and decreased with increasing speed at a constant pressure (**Appendix A, Figure A.2**). Strut size was in the range of 85–380 μm, 200–800 μm, and 300–1200 μm for 0.08, 0.1, and 0.16 mm needle size, respectively. Sacrificial ink was then printed within the matrix hydrogels, and strut size was characterized before and after postprocessing to remove the sacrificial hydrogel (to create channels). **Figure 2.5** shows the data for MeAlg hydrogel. Our results show that the strut size values were slightly higher within hydrogels as

compared to a glass slide (when printed at the same speed and pressure), but not significantly different. There was no significant change in strut size before and after the removal of the sacrificial ink. Note that struts (**Figure 2.5B** and **D**) became channels (**Figure 2.5C** and **E**) after the removal of the sacrificial ink.

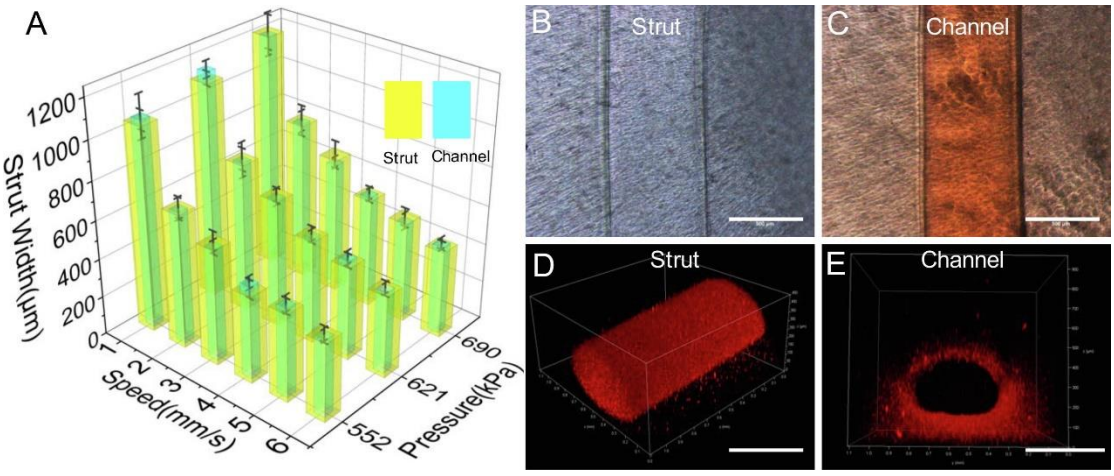

Figure 2.5 (A) Strut width (diameter), before (hydrogel strut) and after dissolution (channel) of sacrificial hydrogel with matrix (MeAlg) hydrogel, is plotted against print speed (mm/s) and pressure (psi). (B-C) Optical images of a representative strut before (B) and after (C) dissolution. (D-E) Representative confocal 3D scans of a strut (D) and a channel (E). In (D) rhodamine dye is mixed with Pluronic. In (E), the channel was injected with a solution containing rhodamine dye, and dye diffused out of the channel. Scale bars are 500 μm.

2.3.5 Controlling Channel Size with Print Speed

Print speed was used to control the printed sacrificial strut size, and hence, the channel size. **Figure 2.6** shows the picture of the MeAlg hydrogel device with two channels (injected with red food coloring) with a gradient change in channel size. The channel at the top was printed with 1 mm/s stepwise decrease in print speed from 10 mm/s to 1 mm/s, creating a change in channel size from 250 μm to 1350 μm, followed by a 1 mm/s stepwise increase in print speed to 8 mm/s. For each print (speed) step, the print length (strut length) was

kept as 0.8 mm, except for the lowest speed, at which the print length was 1.6 mm. The channel at the bottom (**Figure 2.6**) was printed by decreasing the print speed from 9 mm/s to 1 mm/s at 1.8 mm print step size, forming a gradual increase in channel size from 400 to 500 μm to ~500 μm, and up to ~1300 μm. In these print studies, the print pressure was kept constant at 621 kPa (90 psi), and 0.16 mm needle was used.

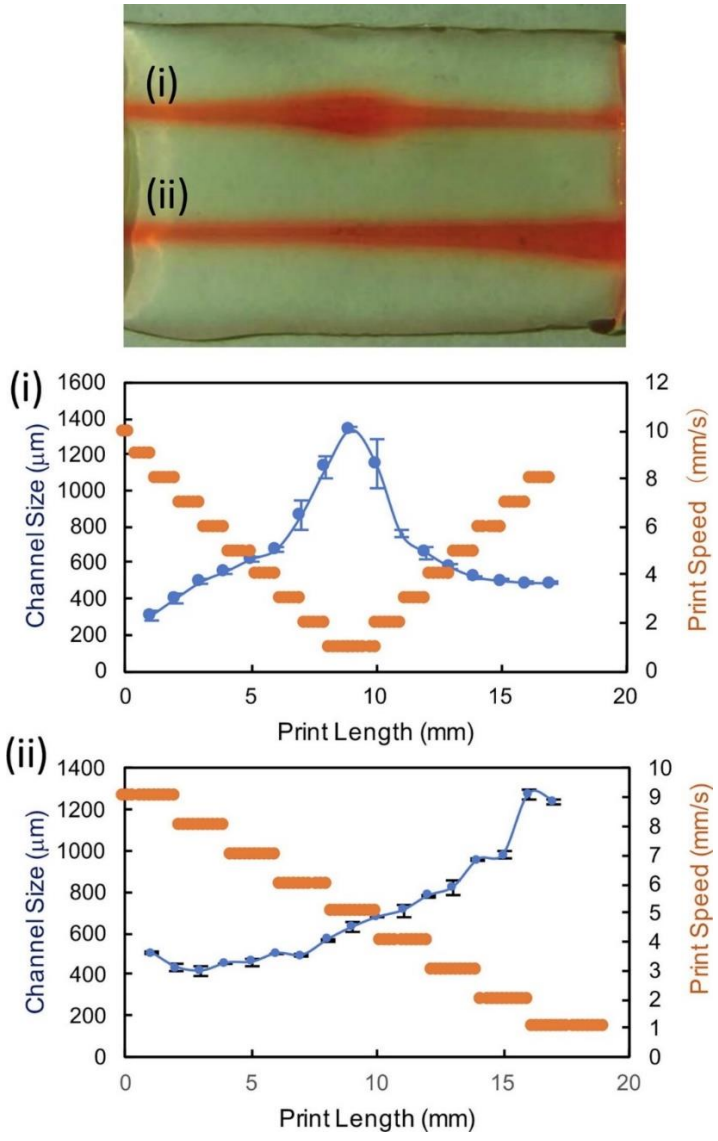

Figure 2.6 3D printed MeAlg hydrogel with two channels with varying channel sizes. (i) and (ii) showing the print speed and channel size values plotted against print length, corresponding to the channels in the top picture.

2.3.6 3D Printing of Perfusable Channels Embedded within Hydrogels

3D digital designs and their corresponding printed constructs are shown in **Figure 2.7**. Channels were injected with a red food coloring solution for visual clarity. In **Figure 2.7A**, MeAlg hydrogel (10 × 10 mm) is shown with various channel sizes, including 732 ± 6 μm, 481 ± 46 μm, 423 ± 23 μm, and 367 ± 13 μm in diameter, from left to the right, respectively. **Figure 2.7B** shows a 3D printed MeAlg hydrogel (10 × 10 mm) with linear channels (800 μm in diameter) on 2 different planes (in the z-direction), forming a checkerboard pattern. **Figure 2.7C** shows 2D converged channels (800 – 1200 μm) embedded within a MeAlg matrix (18 × 16 mm). In **Figure 2.7D**, MeHA hydrogel having wavy channels, in the form of sine waves with constant wavelength (8 mm) but decreasing amplitude (2, 1, 0.5, and 0 mm), is shown. A connected closed-loop channel depicting ‘‘NJIT” letters within MeAlg is shown in **Figure 2.7E**. In **Figure 2.7F**, two sets of linear channels (3 individual channels per set, 500 μm in diameter) were printed at different x- and z-planes. Finally, a hydrogel device with two reservoirs (6 mm in diameter) and connected with two embedded channels (~800 μm in diameter) is shown in **Figure 2.7G**.

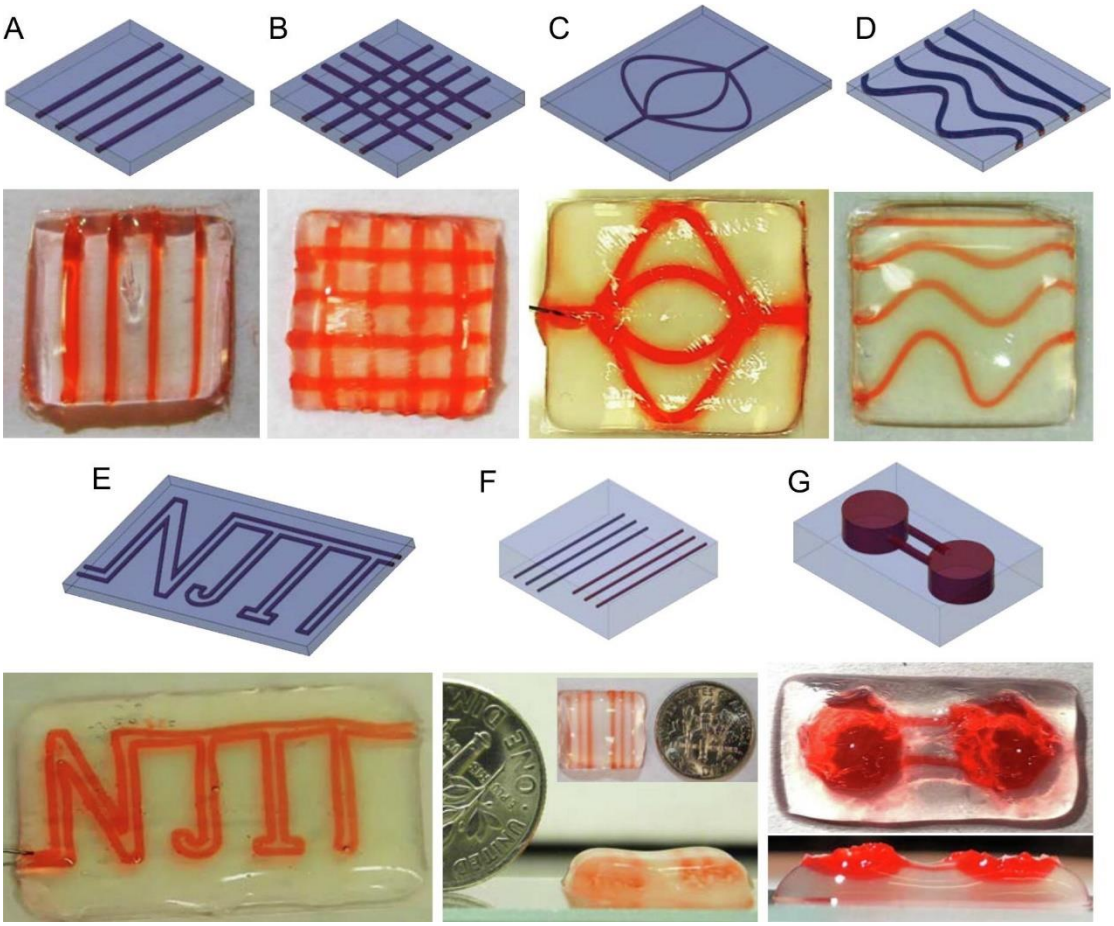

Figure 2.7 Digital designs and corresponding 3D devices. (A) Linear channels with different sizes in a MeAlg matrix (10 x 10 mm) (channel sizes from left to right: 732 ± 6 μm, 481 ± 46 μm, 423 ± 23 μm, 367 ± 13 μm). (B) MeAlg matrix (10 × 10 mm) with 2 layers of linear channels (800 μm in diameter). (C) MeAlg matrix (18 × 16 mm) with converged channels (800-1200 μm). (D) Closed loop NJIT channel within MeHA hydrogel. (E) Injecting red dye into complex channels; (E) Top and side view of a hydrogel (16 × 14 × 4 mm) with 2 sets of channels (500 μm in diameter) at different x- and z-plane; (F) 3D printed wavy channels constant wavelength (8 mm) but increasing amplitude (2, 1, 0.5, and 0 mm). (G) Top and side view of a 3D printed device (30 × 20 mm) with 2 reservoirs (6 mm in diameter) connected with 2 channels (800 μm in diameter) embedded in MeAlg hydrogel. All channels were injected with red food coloring.

2.3.7 Cell Culture within Channels

HUVECs were seeded and cultured up to 9 days within the channels. **Figure 2.8** shows the confocal scanning images of the HUVECs. Our results confirmed cell attachment and complete (circumferential) coverage of the channels with HUVECs.

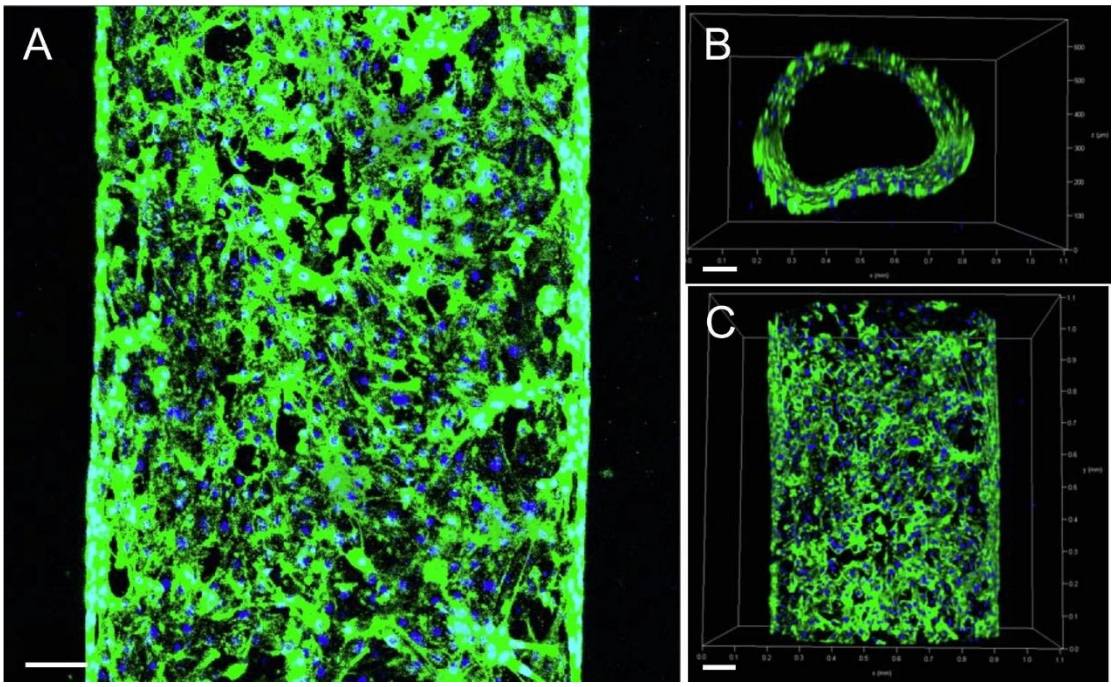

Figure 2.8 Fluorescent images of the HUVECs cultured within channels (green showing F-actin and blue showing nuclei). (A) Maximum projection image from top. Cross-sectional (B) and top (C) view of the channels. Scale bars are 100 μm.

2.3.8 Bioprinting of Stem Cell-laden Hydrogels with Embedded Channels

hMSCs were used to investigate the effect of our channel printing approach on cell viability. For this purpose, cells were mixed into our ink formulations (9% MeAlg and 15% MeHA), and hydrogels with and without channels were printed following our protocol. **Figure 2.9A** shows the representative confocal scanning images of the hMSCs (green indicates live cells, and red indicates dead cells) after printing. **Figure 2.9B** and **C** show the percent (%) cell viability up to 4-day culture. There was no significant change in the % cell viability between groups for 1-day and 4-day culture. We observed a slight decrease in % cell viability for cells cultured in MeHA without channels on Day 4. The cell viability was around 89–90% for cells within MeAlg (both with or without channels) for culture Day 1 and 4, except for the without channels group at Day 4, which was slightly low (~86%). For

the MeHA group, cell viability was 88% and 90% on Day 1, and 86% and 81% at Day 4, with and without channels, respectively.

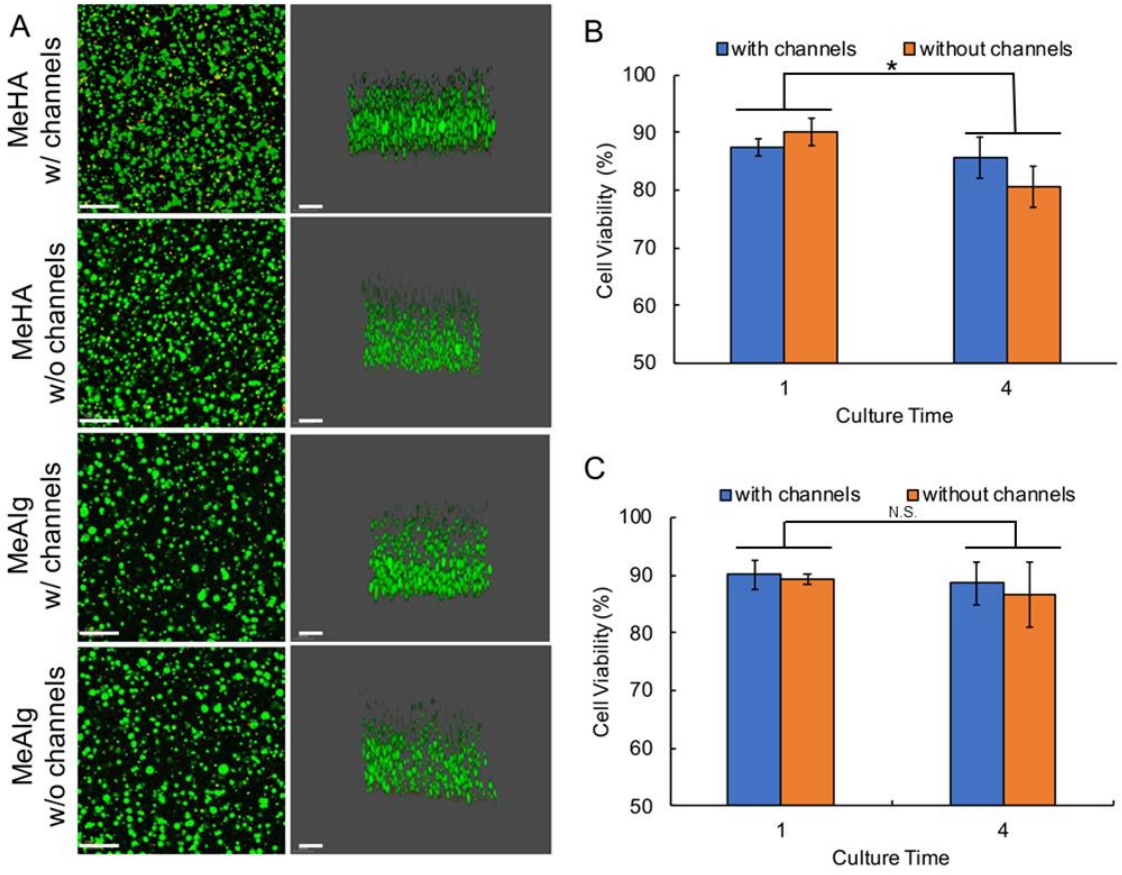

Figure 2.9 (A) Confocal scanning microscopy images of hMSCs (green indicating live cells, and red indicating dead cells) bioprinted with MeHA and MeAlg hydrogels with and without channels and cultured for 1 day. (B-C) Corresponding % viability data for hMSCs cultured in MeHA (B) and in MeAlg (C) hydrogels for up to 4 days. *$p<0.05$, N.S.: not significant.

2.4. Discussion

A novel bioprinting approach was developed to print user-defined and tunable microchannels within photocurable hydrogels. Our approach enables the use of commercially available photocurable hydrogels and sacrificial polymers/hydrogels without

requiring any complex synthetic and processing procedures, desktop (dual-head) bioprinters (e.g., Allevi-2), or any hardware modifications. In this study, we used commercially available and commonly utilized MeAlg and MeHA hydrogels as the photocurable matrix ink and Pluronic (F-127) as the sacrificial ink. MeAlg and MeHA undergo radical polymerization in the presence of a photoinitiator when exposed to light, forming a crosslinked network (or a hydrogel). The degree of crosslinking can be controlled easily by controlling the methacrylate consumption, initiator concentration, and light exposure time [174]. Methacrylates also undergo a Michael-type addition reaction with thiols, thus allowing tethering of bioactive molecules containing cysteine groups [173, 174]. This could be useful to incorporate bioactive cues into the hydrogel matrix when needed. For instance, we functionalized the matrix inks with RGD-peptide, following the protocol developed previously [173, 174], to enhance stem cell-matrix adhesion (**Figure 2.9**).

In this study, we first investigated the printability of the ink formulations by performing single line (strut) tests on methacrylated glass slides. Methacrylation of the glass slides was not required and did not affect the printing parameters or printed line size but ensured strong adhesion of MeHA and MeAlg to the glass slide during line tests. For matrix hydrogels, two different needles (0.21 and 0.30 mm in diameter) were used to investigate the printability of these formulations. In addition to these two needles, we were able to extrude the sacrificial hydrogel using a 0.08 mm needle due to its superior shear thinning behavior as compared to matrix hydrogels (**Figure 2.2**). The main goal of these studies was to adjust the print speed and pressure to obtain good quality struts (or lines), i.e., continuous lines that are uniform in thickness without sagging or dragging. A wide

range of print pressure (34–621 kPa) and speed (6 – 20 mm/s) were used to create lines from 250 μm up to 1,500 μm in diameter (**Table 2.1**) for matrix hydrogels. As expected, higher pressures were needed to extrude the more concentrated formulations. For instance, a print pressure in the range of 483– 621 kPa was needed to extrude 15% MeHA, whereas the pressure was in the range of 138–276 kPa for 9% MeAlg (**Figure 2.3**). Note that the initial viscosity values for the MeAlg formulations were much higher than that of MeHA, but MeAlg formulations showed a higher degree of shear-thinning (**Figure 2.2**). We believe that this allowed the 9% MeAlg to be printed at lower pressures. We usually observed an increase in strut size with increasing pressure (as more material is extruded) at a constant speed and a decrease in strut size with increasing speed at a constant pressure. As shown in the results section (**Figure 2.3**), this was more pronounced in 9% MeAlg as compared to 15% MeHA (**Figure 2.3**). We believe that this is mainly due to the significantly higher print pressures for MeHA. As our printing approach requires partial crosslinking immediately after printing, we decided to use the formulations with the highest polymer concentrations (15% MeHA and 9% MeAlg) to reduce the partial crosslinking time, to allow sufficient support to the sacrificial hydrogel when the matrix hydrogel is in its uncrosslinked state, and to limit mixing between the matrix hydrogel and the support hydrogel. Thus, to form the matrix layers, 9% MeAlg was printed at a pressure of 138 kPa and a print speed of 10 mm/s, using 0.21 mm diameter needle. 15% MeHA was printed at a pressure of 552 kPa and a print speed of 10 mm/s, using the same needle. These conditions corresponded to ~500 μm diameter line (**Figure 2.3**) and led to printed layers that are ~500 μm in thickness. When needed, the matrix layer height was increased by

lowering the print speed (or increasing the pressure) to allow printing of larger size (>500 μm) sacrificial lines within the matrix layer.

For Pluronic (sacrificial ink), line test studies were crucial as the strut size directly determined the channel size (**Figure 2.5**). Line tests were first performed on the glass slides, to determine the relationship between print parameters and strut size. The strut sizes could be printed as low as 85 μm using a 0.08 mm needle. The next step was to use these parameters to print Pluronic in the matrix hydrogel. For this purpose, we first confirmed that the needle moved freely within the selected matrix formulations (15% MeHA as compared to 9% MeAlg) and that Pluronic did not mix with the selected matrix formulations when printed within. Note that it is not possible to use the free-form printing approach (discussed in the introduction) here, as formulations with much higher polymer concentrations are needed to support Pluronic when a support bath (filled with matrix formulation) is used, which would hinder the needle motion. Our approach overcomes this issue by taking advantage of a sequential crosslinking approach, completely eliminating the need for a bath of support material.

In our approach (**Figure 2.1**), we printed the (photocurable) matrix ink layer-by-layer as usual. To create self-supporting layers, each layer was briefly exposed to light (5 s for MeHA, 15 s for MeAlg) to partially photocrosslink the layer. The ink formulations behaved like a viscous liquid (indicated by G'' > G') (**Figure 2.4**). When partially crosslinked, both G' and G'' increased, but G' became larger than G'', indicating a transition from a viscous behavior to an elastic behavior (gel point defined at G' = G''). At this stage, printed hydrogel layer was able to self-support itself. After the second layer of matrix material was printed, Pluronic was directly printed inside the top layer, and then the

layer was exposed to light for partial crosslinking. A final layer of matrix material was printed, followed by partial crosslinking. The construct was then exposed to light to fully crosslink the construct (240 s for 9% MeAlg and 90 s for 15% MeHA). At this stage, we observed a significant increase in G' and a significant decrease in phase angle, confirming the complete gelation. The line test results showed that Pluronic strut size was slightly larger but not significantly different when printed inside the matrix hydrogel as compared to struts printed on the glass slides (at the same print pressure and speed). Struts were dissolved in DPBS within minutes to form channels, and there was no significant difference between the strut and channel size (**Figure 2.5**). This was due to the equilibrium swelling behavior of the matrix hydrogels in their fully crosslinked state, which limited the volume changes caused by swelling. One of the advantages of our approach is the ability to control the channel size by simply controlling the print speed. This allowed fabrication of individual channels with varying sizes, or a channel with varying size (**Figure 2.6**), without changing the print needle.

To show the applicability of our approach, we developed a wide range of hydrogel devices with embedded channels, with different sizes, shapes, and complexity (**Figure 2.7**). We were also able to print a commonly used microchip design from MeAlg hydrogel. The size of these devices was not limited by the printing step but the ability to keep the devices in a humid environment. Larger devices tend to shrink with time, which is a gradual process and usually starts from the top surface, leading to slight deformations in the hydrogel (**Figure 2.7G**). This is typical behavior for hydrogels, and it could potentially be eliminated by keeping the hydrogels in a humidity-controlled chamber or in an aqueous media immediately after the printing process.

Finally, we successfully showed the compatibility of our printed devices for cell culture by performing two separate *in vitro* studies using HUVECs and hMSCs. These cell types are significant and commonly used models: hMSCs are used for tissue regeneration, and organ printing due to their ability to migrate, proliferate, and differentiate into many tissue types (muscle, cartilage, and bone) and HUVECs are important in understanding vascularization and angiogenesis. HUVECs were seeded inside the channels and cultured for 9 days to investigate cell adhesion and monolayer formation. Our results showed that cells attached inside the channels circumferentially and formed confluent layers. Note that cells that did not attach to the channels formed large aggregates and eventually died in the absence of adhesive peptides. Our future goal is to further investigate the endothelization and permeability of the endothelial layer. In a separate study, hMSCs were incorporated into the ink formulations to test the cell viability. The goal was to check if our printing approach had an effect on cell viability. Cell viability was 90% after 1 day of culture and slightly dropped (but not significantly) after 4 days of culture. But for MeAlg and MeHA without channels, this drop was about 5% and 10%, which is not surprising considering these were bulk hydrogels. The presence of channels enhanced viability as expected. Overall, these results show the feasibility of our approach to fabricate 3D printed cell culture platforms.

2.5. Conclusions

In conclusion, a novel approach was developed to 3D print complex microchannels within photocurable hydrogels. Specifically, photocurable hydrogels were used as bioinks to print constructs layer-by-layer and exposing each printed layer to light ensured the formation of

self-supporting layers. This approach enabled direct printing of a sacrificial hydrogel into a freshly printed photocurable hydrogel layer. This freshly printed hydrogel layer confined and supported the sacrificial strut. After complete crosslinking of the hydrogel layer, the sacrificial hydrogel was washed away to form channels. Endothelial cells adhered and formed confluent layers within these channels. When incorporated into the photocurable ink formulations, stem cells remained highly viable within the matrix hydrogels.

CHAPTER 3

NOVEL BIOINKS FROM UV-RESPONSIVE NORBORNENE-FUNCTIONALIZED CARBOXYMETHYL CELLULOSE MACROMERS

This chapter has been adapted from the publication:
S. Ji, A. Abaci, T. Morrison, W.M. Gramlich, M. Guvendiren, Novel bioinks from UV-responsive norbornene-functionalized carboxymethyl cellulose macromers, Bioprinting 18 (2020) e00083.

3.1 Introduction

Three dimensional bioprinting is an emerging field with a significant potential to create custom-designed and patient-specific "living" constructs using a patient's own medical images and cells [9, 27, 28, 178]. 3D bioprinting could potentially eliminate organ shortage [59, 82, 142, 146] and enable development of patient-specific tissue models for personalized drug screening [145, 150, 179-181]. A recent frontier is in situ bioprinting for reparative or regenerative therapy, in which a living tissue is printed directly at the site of an injury or a defect [182-184]. Despite the strong potential of bioprinting and recent advancements in the bioprinting technology, there is a notable lack of diversity in bioinks which significantly hinders the widespread use of bioprinting.

Three dimensional bioprinting enables layer-by-layer manufacturing of a living construct from bioinks, which are bioprintable formulations composed of cells that are usually supported with a hydrogel [89]. The requirement for live cell printing significantly limits the number of additive manufacturing technologies that are suitable for bioprinting [185]. Bioprinting technologies include extrusion-based direct ink writing (DIW), droplet-based inkjet printing, and light-based approaches, including projection stereolithography and laser-induced forward transfer (LIFT) [10, 20, 185]. DIW is the most commonly used technique due to its availability, affordability, and ease of use. In DIW, a bioink

formulation is extruded through a blunt needle to form a self-supporting structure. In this process, the bioink should meet the basic requirements for extrusion-based bioprinting [186-188], such that it should *(i)* have a suitable viscosity, i.e., low enough for easy extrusion yet high enough for formation of self-supporting layers post-printing to minimize sagging, usually in the range of 30 to 6×10^7 mPa·s, and *(ii)* allow printing of living cells and support high viability (>90%) [89, 186, 187]. In addition, the bioink and its degradation products should be cytocompatible and should not induce an inflammatory response when implanted [187, 189].

Most commonly used bioinks are formulated from cell-laden hydrogels due to their high-water content and properties mimicking native tissue microenvironment [44, 45]. A variety of hydrogel-based bioinks have been developed from synthetic (such as Pluronic [190, 191] and poly(ethylene glycol) [192]), or natural (gelatin [193-195], hyaluronic acid [130, 196], alginate [196, 197], chitosan [198], collagen [199, 200], fibrin [201], and silk [202, 203]) polymers/macromers , or decellularized tissue materials (e.g., heart, bone, liver, pancreas, etc.) [204, 205]. The building blocks of these formulations are usually modified to allow tunable viscosity and shape fidelity during printing process. Although innovative approaches have been developed to control printability including pre-crosslinking to control flow [192] or rapid crosslinking during or after-printing [206, 207], or designing shear thinning formulations [130, 208], novel bioink formulations are still needed to broaden the currently available bioink "library" and to develop stimuli responsive bioinks enabling control of bioprinted construct properties post-printing.

This study is focused on carboxymethyl cellulose (CMC), a commonly used cellulose derivative. Cellulose is one of the most abundant and renewable natural polymers

[209, 210]. As a natural polymer, cellulose is inherently bioactive, biodegradable, and biocompatible [209]. The hydroxyl groups on its backbone structure allows functionalization of cellulose to tune its properties [211]. When compared to cellulose, CMC is highly soluble in water due to its carboxyl groups [212] making it an attractive building block for hydrogels. CMC-based hydrogels have been developed utilizing a wide range of crosslink mechanisms including physical and chemical crosslinking [13]. For instance, Nie et al. reported CMC-based hydrogels by crosslinking sodium CMC with $AlCl_3$, and studied the effects of crosslinker, CMC concentration and temperature on hydrogel stiffness and degradation [16]. Chemically crosslinked CMC-based hydrogels have been developed using irradiation-initiated [17-19], photo-initiated radical [20, 21], enzymatic [22], and epoxide-opening reactions [23]. For instance, methacrylated CMC is synthesized to allow photo-initiated radical reaction to fabricate CMC-based hydrogels. These hydrogels were used to facilitate chondrogenic differentiation of encapsulated human mesenchymal stem cells (hMSCs) encapsulated within the hydrogels [21].

Cellulose has been used a filler, or as a component, in ink formulations [213-216]. Majority of the studies utilized cellulose/alginate-based ink formulations, utilizing a range of cellulose derivatives (nanofibrillated cellulose, nanocellulose, and methylcellulose) and taking advantage of physically crosslinking ability of alginate with $CaCl_2$ [217-222]. For instance, nanocellulose-alginate based bioinks were developed for 3D bioprinting of human chondrocyte-laden hydrogels for cartilage regeneration [217, 223]. Muller et al. developed alginate sulfate/nanocellulose bioinks but reported significantly compromised proliferation ability of chondrocytes during printing process [220]. Markstedt et al. developed bioinks from cellulose nanofibrils mixed with xylan for crosslinking [224]. Most

recently, methylcellulose (MC)-based hydrogels were printed utilizing the sol-gel transition, or lower critical solution temperature (LCST), allowing printing of MC-based hydrogels at 21℃ with high cell survival (80%) post-printing [225]. Li et al. developed highly thixotropic inks from alginate/methylcellulose blend hydrogels, and showed that the treatment of the printed constructs with trisodium citrate (TSC) significantly enhanced the interfacial bonding between printed layers [226]. Finally, Lewis group developed hydrogel composite inks composed of soft acrylamide matrix supported with cellulose fibrils, and crosslinked with clay [213]. They were able to selectively align cellulose nanofibrils during the printing process to develop 3D printed structures with anisotropic stiffness, which led to shape change on immersion in water. In this study, novel photocurable bioink formulations were developed directly from carboxymethyl cellulose (CMC) eliminating the need for alginate or other additives/components.

Light-induced free radical polymerization of methacrylates or acrylates is a widely used approach in designing photoreactive bioinks, yet this reaction is not specific and leads to formation of a heterogenous network composed of kinetic chains. Thiol-norbornene photo-click chemistry is specific to norbornene and thiyl radicals (i.e., radicals from thiols) as compared to norbornene radicals (its own radicals) or nonradical thiols [227, 228]. This is important to achieve selectivity in crosslinking (crosslinkers containing multi-thiols) and tethering of biomolecules (containing mono-thiols). This mechanism ensures a more homogeneous crosslinking in a controllable manner [227, 229, 230]. Natural (such as alginate [231], hyaluronic acid [230, 232], and gelatin [233, 234] and synthetic polymers (such as poly(ethylene glycol) [229, 234, 235]) have been modified with norbornene group to fabricate photocurable, cell-laden hydrogels. Recently, CMC has been modified with

norbornene groups [212, 236] to develop renewable hydrogels. Gramlich group recently demonstrated high cell viability of encapsulated stem cells within norbornene functionalized CMC [237]. Motivated by these recent results, we focused on developing novel bioink formulations from norbornene functionalized CMC.

In this study, we report two novel stimuli responsive bioink platforms from CMC for extrusion based bioprinting. CMC is functionalized with thiol-ene reactive norbornene (Nor) with an amide, norbornene CMC (NorCMC), or an ester linker, carbic (norbornene) functionalized CMC (cCMC). CMC was chosen as the building block for both of our bioink platforms due to its high availability and low cost, and high solubility in water. Light-induced thiol-ene click chemistry enabling norbornene was selected as the functional group to achieve selective crosslinking and selective tethering of biomolecules. Printability of the bioink platforms was determined by the thiol-Nor ratio for each macromer concentration. CMC-based bioink platform allows tunable printability, stiffness, and high viability of bioprinted cells, and broadens the range of currently available bioink platforms.

3.2 Material and Methods

3.2.1 Polymer Synthesis

The macromers, cCMC and NorCMC, were synthesized according to methods developed previously for cCMC [236] and NorCMC [237]. To synthesize cCMC, CMC (90 kDa, 0.7 carboxymethyl groups per anhydroglucose unit, Sigma) was dissolved in reverse osmosis (RO) water at 1% (w/v). Then, 7.26 g of cis-endo-5-norbornene-2,3-dicarboxylic anhydride (carbic anhydride, TCI) was added to the CMC solution (per gram of CMC). The reaction was maintained for 2 hours while the pH of the reaction was adjusted at the

range of 9.0-10.5 by dropwise adding 10M NaOH. Subsequently, 10-fold volume of the reaction solution of ice-cold acetone was used to precipitate the reaction solution. The precipitate was collected by suction filtration and dissolved in RO water at 1% (w/v) and dialyzed (6-8 kDa) against RO water for 3 days followed by lyophilization. For NorCMC, sodium CMC (90 kDa, Sigma) was dissolved in RO water at 1% (w/v), and 0.592 g of 1-ethyl-3-(3-dimethylaminopropyl) carbodiimide hydrochloride (EDC HCl), 0.356 g of N-hydroxysuccinamide (NHS), and 0.4 mL of 5-norbornene- 2-ethylamine (NA) were added (per gram of sodium CMC). The reaction solution was stirred and maintained at room temperature for 18 hours. NaCl was added to the reaction solution, stirred at room temperature for 30 min, and the reaction solution was precipitated in 10-fold ice-cold acetone. The precipitate was dissolved in RO water at 1% (w/v) and dialyzed (6-8 kDa) against RO water for 3 days followed by lyophilization. The extent of the modification for both polymers was characterized using ^{1}H NMR spectroscopy using a Bruker Avance Neo 500 MHz spectrometer (NorCMC) and a Varian Inova 400 MHz spectrometer (cCMC).

3.2.2 Cell Culture and Maintenance

Human mesenchymal stem cells (hMSCs, passage 4, Lonza) were cultured in the growth media (MEM-α (Gibco), supplemented with 10% fetal bovine serum (FBS, Gibco) and 1% penicillin-streptomycin (pen-strep, Gibco)) at 37 ℃ and 5% CO_2. Growth media was refreshed every 3 days. Human umbilical vein endothelial cells (HUVECs, passage 5, Lonza) were cultured in EGM-2 media (EGM-2 Bullet Kit, Lonza). Media was changed every two days to ensure a proper cell proliferation. NIH 3T3 fibroblasts were cultured in DMEM (Gibco) supplemented with 10% FBS (Gibco) and 1% pen-strep (Gibco). Media was refreshed every 3 days.

3.2.3 Ink Preparation

Ink formulations contained norbornene modified CMC (15% (w/v) for cCMC and 10% (w/v) for NorCMC) and 0.05% (w/v) lithium phenyl-2,4,6-trimethylbenzoylphosphinate (LAP, Allevi) in growth media. For instance, to prepare a 10% NorCMC, 100 mg of NorCMC was dissolved in 1 ml of 0.05% LAP stock solution in growth media in a glass vial, covered with an aluminum foil. The solution was stirred overnight at room temperature. To adjust the pH of the cCMC solution to pH = 7.5, 20 μL of triethylamine (Sigma Aldrich) was added to the cCMC solution.

To prepare a bioink, 900 μL of LAP stock solution was used to dissolve the polymer. Then, the solution was mixed with 100 μL of cell suspension (hMSC, 3T3, or HUVEC; 1×10^7 cells/mL) using a magnetic stirrer, leading to a final ink concentration of 15% cCMC (or 10% NorCMC). Each ink formulation was transferred into a BD Luer-Lok™ 10-mL syringe prior to printing. Prior to printing process, pre-calculated amount of the crosslinker (DL-dithiothreitol (DTT), Sigma) was added to the bioink formulation and stirred gently for 1 minute.

3.2.4 Rheological Characterization of the Ink Formulations

Malvern Ultra+ Rheometer (flat plate geometry, 20 mm, 1 mm gap) was used to analyze the rheological properties of the ink formulations. To investigate the crosslinking process in the absence of light exposure, time sweep tests were performed at a frequency of 1 Hz and an oscillatory strain of 0.05%. Elastic modulus (*G'*), viscous modulus (*G''*), viscosity (γ) and phase angle (Φ) values were recorded. To investigate the photocrosslinking process, inks were casted on to the lower plate of the rheometer, and time sweep tests were performed using an optical kit (Malvern) connected to a UV light source (Omnicure S2000,

356 nm, 5 mW/cm^2). Light intensity was adjusted to represent the intensity during printing process (405 nm, 40 mW/cm^2) according to the molar absorptivity spectrum of the photoinitiator (LAP) [175]. The UV light was turned on for 4 minutes after 1 minute of equilibrium time during time sweep tests. Initial viscosity values refer to mean of the viscosity values measured for the first 1 min prior to UV exposure.

3.2.5 Mechanical Properties of the Crosslinked Ink Formulations

Malvern Ultra+ Rheometer (flat plate geometry, 8 mm) was used to measure the compressive modulus (Young's modulus, *E*) of the samples. Two sets of disc-shaped hydrogel samples (1 mm in thickness and ~25 mm in diameter) were prepared via direct casting followed by UV exposure and bioprinting process. Samples were kept in DPBS for 24 hours to ensure equilibrium swelling. The compression test was performed by applying a compressive normal force to the hydrogel sample using the upper flat plate geometry while monitoring the gap distance (where strain is equal to the gap - sample thickness). To ensure initial contact, an initial compressive force equal to 0.05 N was applied. The compressive force was increased continuously (0.1 mm/s) up to 2 N. The compressive modulus (*E*) was obtained by calculating the slope of stress-strain curve (using the linear range within 10% strain).

3.2.6 Scaffold Design

3D scaffold designs were created by Autodesk® Fusion 360™ and the 3D models were sliced with Slic3r in Repetier-Host to generate G-code files. A 15mm × 15 mm grid-like 2-layer scaffold and a 12 mm × 8 mm 3-layer cuboid were designed for printability tests and cell viability tests.

3.2.7 Line Test

Ink formulations were used to print individual struts (lines) on a glass slide at different print pressures and speeds. The images of the printed struts were captured by a microscope. Three random parts of each strut (from three samples per each group) were captured for analysis. The strut diameter was measured using ImageJ). 10% Methacrylated hyaluronic acid (MeHA) was used as a control group.

3.2.8 Printability Test

In this study, an Allevi 2 (Allevi) bioprinter was used to perform all the printing processes. After mixing with DTT, the bioink formulations were immediately transferred to a 10-mL syringe, and the syringe was mounted on the printer. To test the printability, the bioink was used to print a 15 mm × 15 mm grid-like 2-layer scaffold on a methacrylated glass slide (following the surface treatment protocol described previously [176]). The elapsed time was also recorded after mixing DTT in bioink formulation. Printing parameters were optimized with respect to this elapsed time to print uniform grids. Methacrylated hyaluronic acid (MeHA) was used as a control group. To print thick hydrogel scaffolds (> 3 mm), 30% Pluronic F-127 was used as a support ink. After crosslinking process, the scaffolds were immersed in DPBS at 4 ^{o}C to remove Pluronic support. To print multi-material scaffolds, cCMC 1:4 and NorCMC 1:2 were prepared as mentioned. To distinguish different inks, 100 μL of food color was added to cCMC 1:4.

3.2.9 3D Bioprinting of Cell-laden Hydrogels

Cell-laden bioink (15% cCMC or 10% NorCMC) was printed on methacrylated glass slides at optimized parameters obtained from printability tests. The printed cell-laden scaffolds were immediately transferred into non-treated 6-well plates and 5 mL of growth media was

added into each well. Methacrylated hyaluronic acid (MeHA) was used as a control group.

3.2.10 Cell Viability Tests

Cell-laden hydrogels were cultured for 7 days, and live-dead staining was performed at Day 1, 4, and 7 to characterize the viability of the encapsulated cells. Cell-laden hydrogels were washed with DPBS and then stained with calcein-AM ("live", 0.5 μL/mL) and ethidium homodimer ("dead", 2 μL/mL) for 15 minutes. Samples were washed with DPBS and transferred to confocal laser scanning microscope (confocal and 2-photon scanning microscope, Leica) to capture fluorescent images of the cells. Two samples per group was prepared for each time points and 3 random regions of the gel were scanned. The viability was calculated by counting cells using ImageJ.

3.2.11 Statistical Methods

If not stated specifically we used three samples per each group for all studies. The data were analyzed using KaleidaGraph. Data are presented as mean ± standard deviation. ANOVA with Tukeys HSD post hoc test of means was used to make comparisons between sample groups.

3.3 Results

3.3.1 Bioink Formulations

In this study, two distinct bioink formulations were developed from norbornene functionalized CMC **(Figure 3.1)**, either with an amide, NorCMC, or an ester linker, cCMC. ^{1}H NMR results confirmed 30% and 20% functionalization for cCMC and NorCMC, respectively (**Appendix B**, **Figure B.1**). The compositions of the bioink formulations are given in **Table 3.1**. Bioinks were formulated at 15% cCMC and 10%

NorCMC, with thiol to norbornene ratio (T:NB) equal to (1:4), (1:2), and (1:1).

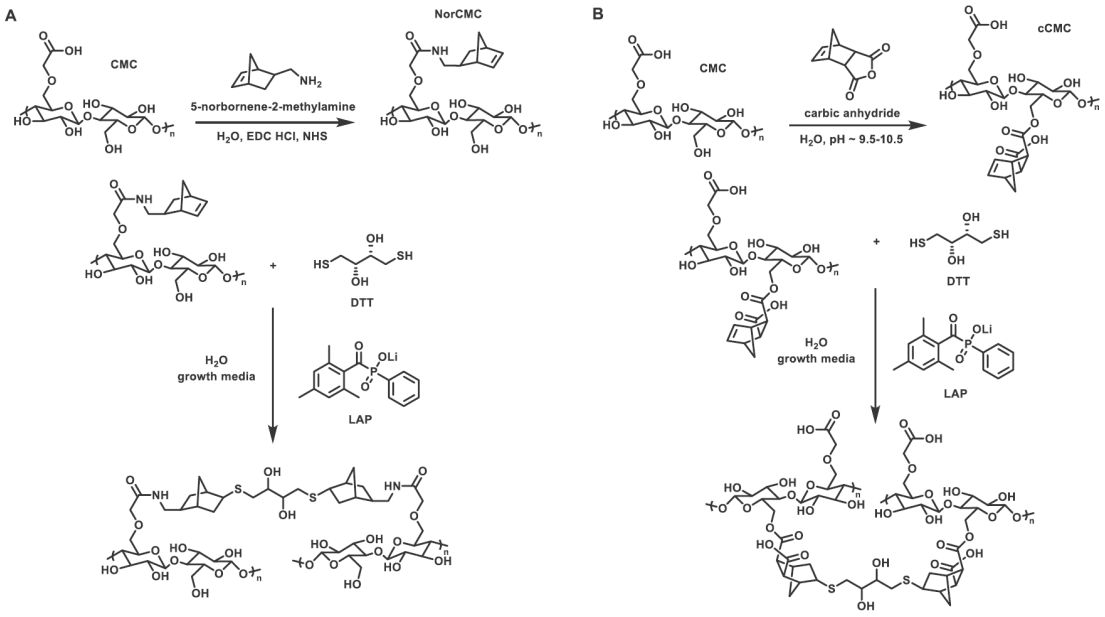

Figure 3.1 Chemical structure, modification reaction, and crosslink mechanism of (A) NorCMC and (B) cCMC.

Table 3.1 Composition, Corresponding Viscosities, and Autogelation Time of Tested Ink Formulations

Ink formulation	Polymer concentration	(T:NB)	Initial viscosity (Pa•s)	Gelation time (min)
cCMC (1:4)	15%	(1:4)	0.8±0.10	91
cCMC (1:2)	15%	(1:2)	1.2±0.10	57
cCMC (1:1)	15%	(1:1)	1.5±0.03	29
NorCMC (1:4)	10%	(1:4)	0.8±0.09	>180
NorCMC (1:2)	10%	(1:2)	1.2±0.09	49
NorCMC (1:1)	10%	(1:1)	2.8±0.03	26

3.3.2 Rheological Test Results

The initial shear viscosities of the bioink formulations were in the range of 0.8-2.8 Pa•s (**Table 3.1**). The gelation behavior of the formulations was characterized with time sweep experiments, in which the elastic modulus (G'), viscous modulus (G''), and phase angle (Φ) values were recorded (**Figure 3.2**). For all of the formulations, autogelation behavior is observed within 3 hours in the absence of UV light. The gel point, i.e., onset of gelation, and the elapsed time for equilibrium for each formulation are summarized in **Table 3.1**. The gel point decreased with increasing T:NB, or increasing crosslinker concentration. For cCMC, gelation time significantly increased from 29 min (1:1) to 91 min (1:4). For NorCMC, gelation time values were 26, 40, and greater than 180 min, for (1:1), (1:2), and (1:4), respectively.

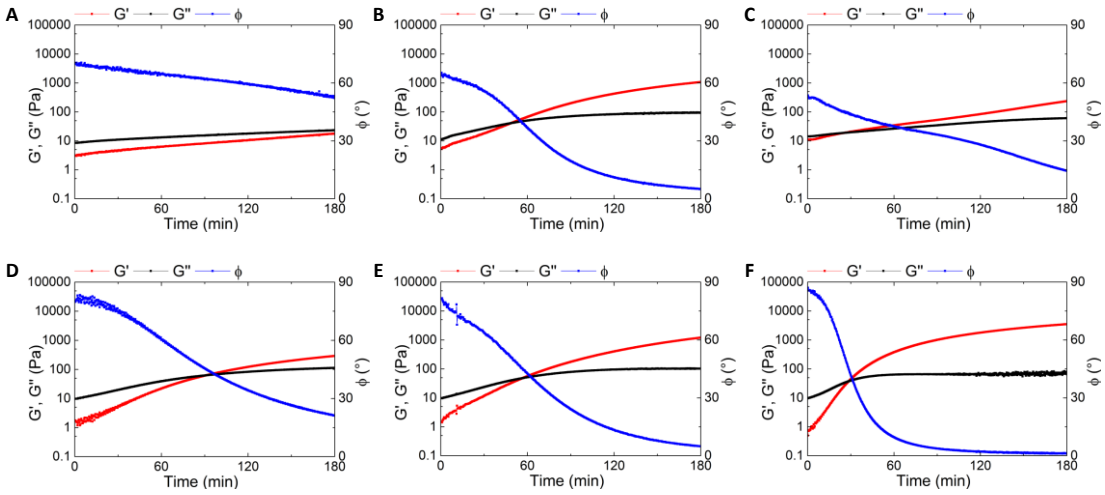

Figure 3.2 Time sweep test of ink formulations without light exposure. (A-C) 10% NorCMC with thiol to norbornene ratio, (T:NB) equal to (1:4) (A), (1:2) (B), and 1:1 (C). (D-F) 15% cCMC with (T:NB) = 1:4 (D), 1:2 (E), and 1:1 (F).

To investigate the gelation under light exposure, samples were exposed to UV light during time sweep tests (**Figure 3.3,** and **Appendix B**, **Figure B.2**). For cCMC,

independent from T:NB, gel point was equal to ~18 s, and it took approximately 120 s for crosslinking reaction to reach equilibrium. For NorCMC, the gelation time and equilibrium time were equal to ~5 s and ~60 s, respectively. The magnitude of the equilibrium shear modulus (*G'*) was determined by the composition of the ink formulation, such that a higher (T:NB) resulted in a higher *G'*. For cCMC formulations, the equilibrium values for *G'* were equal to ~3200 Pa for (1:4) and ~9300 Pa for (1:2). For NorCMC, the equilibrium values for *G'* were equal to ~4600 Pa for (1:4) and ~8700 Pa for (1:2).

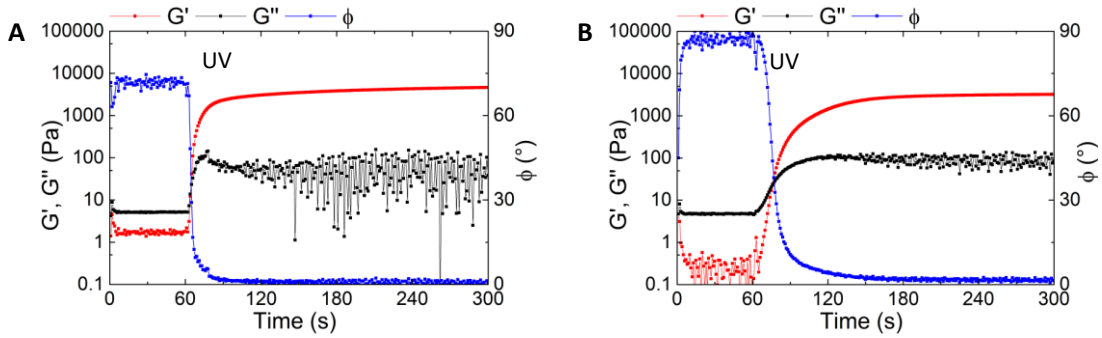

Figure 3.3 Time sweep test of ink formulations under light exposure for: (A) NorCMC (1:4) and (B) cCMC (1:4). Green area denotes the UV exposure period.

3.3.3 Mechanical Tests Results

To probe the mechanical properties, the compression moduli were measured using 3D printed samples from all of the ink formulations. As shown in **Figure 3.4A**, for the same macromers, higher (T:NB) resulted in higher compressive moduli. For 15% cCMC, the compressive modulus increased by ~7-fold (from 46 to 316 kPa) when the (T:NB) increased from (1:4) to (1:2). The same trend was observed for 10% NorCMC, but the increment was less than 3.3-fold (from 40 to 133 kPa).

3.3.4 Swelling Tests Results

Swelling tests were conducted on 3D printed samples (**Figure 3.4B**). Our results showed that increasing (T:NB) resulted in a 1.8 fold decrease in the swelling ratio (from 26 to 14 kPa) for cCMC, and a 1.6 fold decrease in the swelling ratio (from 24 to 15 kPa) for NorCMC.

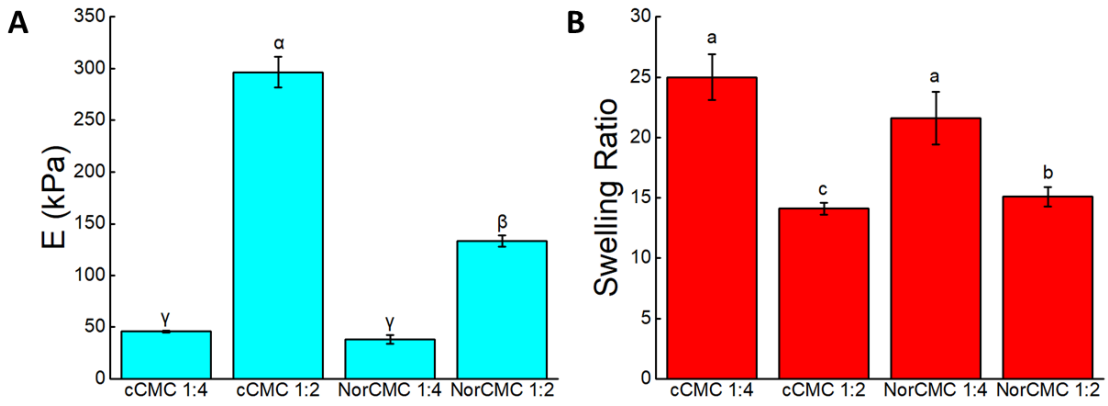

Figure 3.4 (A) Compressive modulus (*E*) values of the 3D printed hydrogels from bioink formulations. p<0.005 for cCMC (1:2), as compared to the rest of the sample groups, and for NorCMC (1:2), as compared to the other groups. (B) The equilibrium swelling ratios values of the 3D printed hydrogels. p<0.005 for cCMC (1:4) and for NorCMC (1:2), as compared to cCMC (1:2) and NorCMC (1:2).

3.3.5 Line Test Results

Figure 3.5 shows the line test results for 15% cCMC and 10% NorCMC. MeHA (10%) was used as a control group. In general, strut size increased with increasing print pressure and decreasing print speed. For instance, at 10 mm/s, the line width increased from 920 to 1390 m for cCMC, from 850 to 1790 m for NorCMC, and from 1110 to 1720 μm for MeHA, when the pressure was increased from 138 kPa (20 psi) to 276 kPa (40 psi). When printed at 20 mm/s and 138 kPa print pressure, it was possible to achieve 630 μm for cCMC, 620 μm for cCMC, and 800 μm for MeHA.

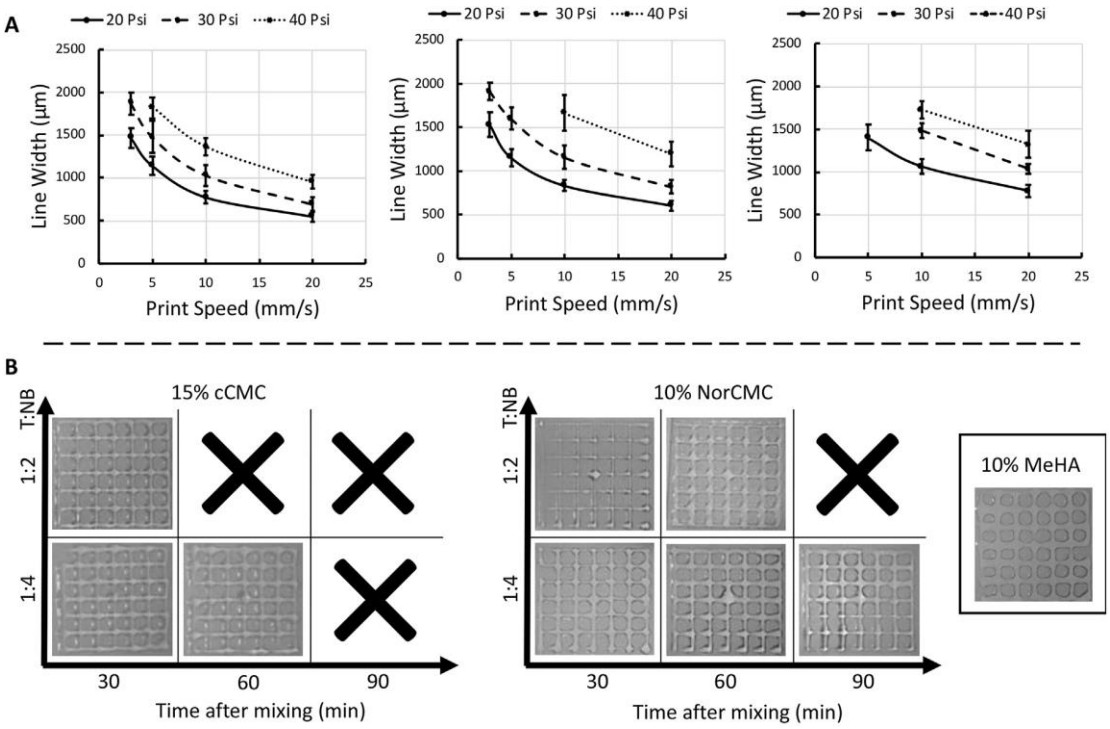

Figure 3.5 (A) Line test results for 15% cCMC, 10% NorCMC and 10% MeHA bioinks. Error bars denote standard deviation for n $\geqslant$ 5. (B) Printability tests for 15% cCMC and 10% NorCMC for different (T:NB). The x-axis shows the elapsed time after mixing the crosslinker (DTT) with the ink formulation. Printability test result for 10% MeHA is given as a control.

3.3.6 Printability Test Results

Ink formulations from cCMC and NorCMC (both formulations with (T:NB) equal to (1:4) and (1:2)), were used to print grid-like scaffolds (**Figure 3.5**) to investigate printability. The pressure was set at 138 kPa (20 psi) at the beginning (for 30 min delay time) and gradually increased to 276 kPa (40 psi, for 60 min delay time) and 345 kPa for (50 psi, for 90 min delay time) to compensate the increment of the ink viscosity due to autogelation. The print speed was controlled between 5 mm/s and 10 mm/s to print the gel with a uniform shape. Due to autogelation, ink formulations were not extrudable after a certain time for each formulation that was marked with a cross sign in **Figure 3.5**. Dual material printing

was used to bioprint thick hydrogel scaffolds (NorCMC (1:2)) supported with sacrificial Pluronic, and NorCMC (1:2) scaffolds with fast degrading cCMC (1:4) patterns (**Figure 3.6)**.

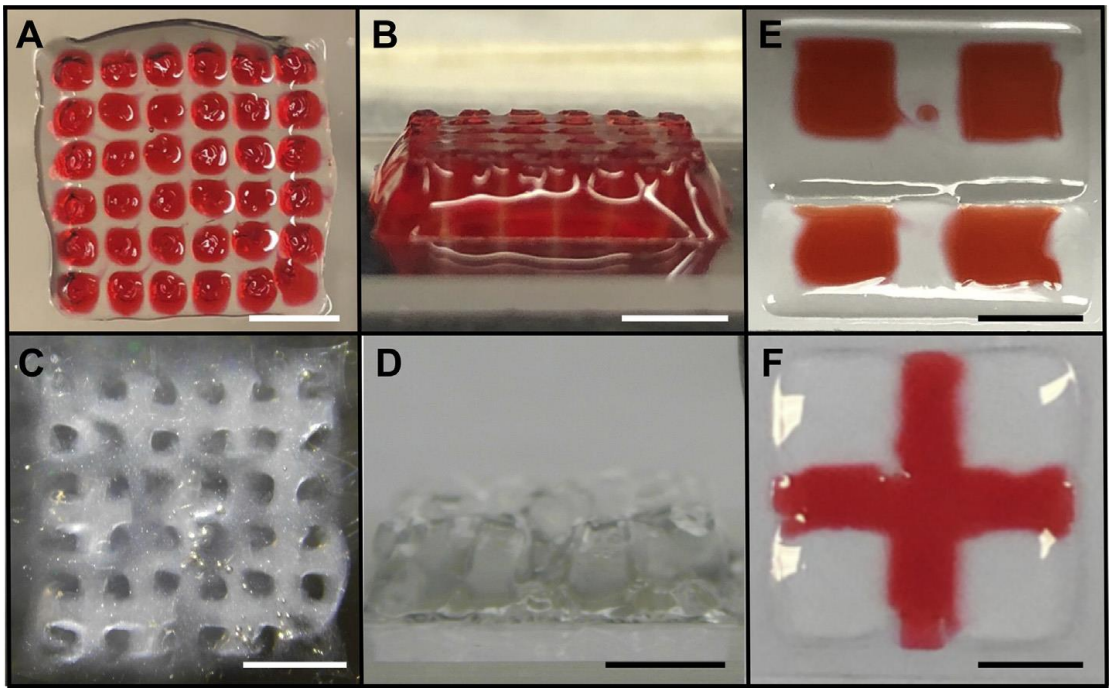

Figure 3.6 Pictures showing multi-material printing of thick (>3 mm in height) scaffolds. (A-B) Top (A) and side (B) views of NorCMC (1:2) scaffold printed with Pluronic (red). (C-D) Scaffold after Pluronic is dissolved in DPBS. (E-F) NorCMC (1:2) scaffolds printed with fast degrading cCMC (1:4) (red). Scale bars are 5 mm.

3.3.7 Bioprinting Test Results

Figure 3.7A shows the cell viability data (in percentage) for hMSCs, 3T3 cells, and HUVECs. Note that cCMC sample group degraded in the medium after Day 4. **Figure 3.7B** shows the confocal images of the stained cells, in which the green indicates live cells, and the red indicates dead cells. In the side view images, the range of cells in the vertical direction was different due to the different swelling properties for each ink formulation.

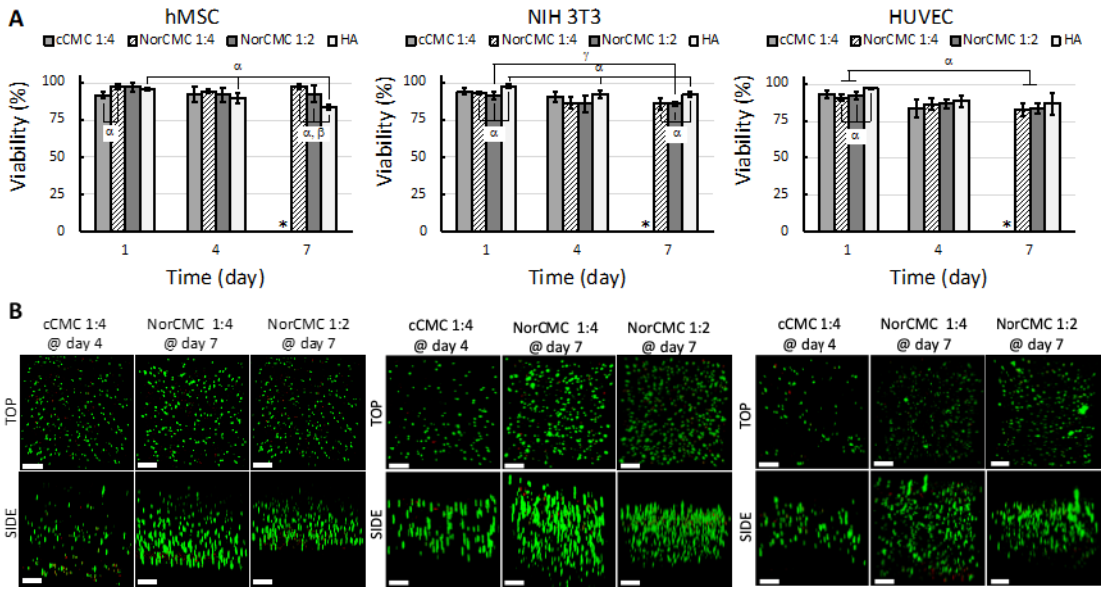

Figure 3.7 (A) Plots showing % cell viability with culture time for cells (hMSCs, NIH 3T3 cells and HUVECs) cultured within bioprinted cCMC, NorCMC and MeHA hydrogels. * indicates the cCMC (1:4) sample group that degraded before Day 7. (B) Confocal fluorescent images of cells (hMSCs, NIH 3T3 cells and HUVECs) within bioprinted cCMC, NorCMC and MeHA hydrogels (green indicating live cells and red indicating dead cells). (Scale bars are 200 μm) For hMSC, $^{\alpha}p < 0.005$ cell viability for MeHA at Day 1 vs. at Day 4 and at Day 7, and at Day 4 vs. at Day 7; cell viability for cCMC (1:4) as compared to NorCMC (1:4) at Day 1; cell viability for NorCMC (1:2) as compared to MeHA at Day 7; $^{\beta}p < 0.0001$ NorCMC (1:4) vs. MeHA at Day 7. For NIH 3T3 cell line, $^{\alpha}p < 0.005$ cell viability for MeHA at Day 1 vs. Day 4 and Day 7; cell viability of MeHA as compared to NorCMC (1:2) and (1:4) at Day 1 and at Day 7; $^{\gamma}p < 0.005$ for NorCMC at Day 1 vs. Day 7. For HUVECs, $^{\alpha}p < 0.005$ cell viability for NorCMC (1:4) and (1:2) at Day 1 vs. Day 7; cell viability for MeHA as compared to NorCMC (1:2) and (1:4) at Day 1. For all groups n=6.

3.4 Discussion

Here, we report novel bioink formulations from norbornene modified, cellulose-based macromers for the first time. Cellulose-based materials are promising candidates as bioinks due to their inherent bioactivity, abundance, and low cost. In this study, two distinct macromers were developed by functionalizing CMC with an amide (NorCMC) or an ester linker (cCMC) with 30% and 20% functionalization for cCMC and NorCMC, respectively. These degrees of functionalization were selected because hydrogels at the same thiol to

norbornene ratio and low solids content (4 wt% polymer) yielded similar compression modulus values [74,75]. Our previous studies (utilizing the same extrusion-based printer) revealed that an initial viscosity in a range of 1-10 Pa•s was ideal for a non-shear-thinning hydrogel when a 27-gauge needle was used [196]. To adjust the viscosity of the inks within this range, polymer concentrations were set to 15% for cCMC and 10% for NorCMC, due to differences in solubilities of the macromers. A higher concentration of cCMC was used as compared to NorCMC to yield similar bioink initial viscosities. The cCMC polymer is significantly easier to dissolve than NorCMC because additional carboxylic acid groups are introduced through the functionalization reaction (**Figure 3.1**). This behavior translated into similar bioink viscosities at different polymer concentrations. Additionally, since the norbornenes are connected to the CMC with different functional groups, degradation behavior was expected to be different with the ester linkages of cCMC degrading earlier than the amides of NorCMC.

Crosslinker, or thiol, to norbornene ratio (T:NB) was systematically increased, from (1:4), (1:2) and to (1:1), to investigate the effect of (T:NB) on bioink properties. For cCMC, the viscosity values did not change significantly with (T:NB). However, for NorCMC, we observe a significant increase in viscosity with increasing (T:NB), such that a 2-fold increase in viscosity is observed when (T:NB) increased from (1:4) (0.8 Pa•s) to (1:1) (2.8 Pa•s). This we believe is due to the spontaneous crosslink of the macromers in the absence of UV light, i.e., autogelation process. Rheological evaluation of the formulations revealed autogelation in all formulations, but the gel point (onset of gelation) decreased significantly with increasing (T:NB). The mechanism of this phenomena has not been understood yet, but it is previously reported that the autogelation accelerates with

increasing thiol and norbornene concentrations, increasing temperature, dissolved oxygen, and acidic conditions [212]. Previous chemical characterization of the autogelation has indicated that it is still a thiol-norbornene reaction, which must be initiated through radicals spontaneously produced in the solution [50]. Future work aims to understand the origin of these radicals. Note that cCMC is acidic when directly dissolved in the growth media or DPBS (pH reaching to ~4) due to the presence of carboxylic acid units in the carbic groups. Therefore, we adjusted the pH to 7.6 (as described in the experimental section) to mainly eliminate cell viability issues. We found that cCMC could form a gel within few minutes when the pH is not adjusted **(**Appendix B, **Figure B.3)**. Considering the autogelation behavior of our macromers, the gelation time (gel point) is considered as a critical parameter for planning the printing process, since these hydrogels were not extrudable when gelled. Considering the time required for pre-printing process, we decided to eliminate the macromer formulations with gel point below 1 hour (**Table 3.1 and Figure 3.5**). Thus, macromer formulations with highest (T:NB), (1:1), for both macromers were eliminated.

Norbornene groups allowed the macromers to be photoresponsive which can lead to crosslinking in the presence of a photoinitiator (LAP) and a crosslinker (DTT) when exposed to light. Rheological tests in the presence of a UV light source allowed us to determine the photocrosslinking parameters to be used during the bioprinting process. For cCMC, it required ~18 s to gel and ~120 s to completely crosslink, which directed us to set the partial crosslink time to be 30 s and the post-print crosslinking time to be 120 s (**Figure 3.3**). The crosslink setting for NorCMC was also set as 10 s for partial crosslinking and 90 s for post-print crosslinking. The printability tests were conducted to evaluate the

printability and to optimize the print parameters (print speed, print pressure, layer height, blue light exposure time). In the printing phase, some deviations between the rheological data (**Figure 3.2**) and printing results (**Figure 3.5**) were observed. In **Figure 3.2E**, the gelation time of cCMC 1:2 was 57 min, which means that the available time for printing should be around 1 hour. However, as shown in **Figure 3.5**, cCMC 1:2 was not printable after 30 min. We believe that this is caused by the undermixing of the gel solution and the crosslinker leading to localized gelation in the syringe due to increased thiol concentration. Vigorous mixing such as vortex is not suitable for viscous ink formulations, and ink can gel during gentle, but longer, mixing process. Due to these concerns, cCMC 1:2 was eliminated from further study.

Our results indicate that the thiol to norbornene ratio (T:NB) of the bioink formulation, controlled by the crosslinker concentration, also affects the mechanical properties of the hydrogel (**Figure 3.4A**). Normally, at the molecular level, increasing crosslinker concentration leads to an increase in the compressive modulus (Young's modulus, *E*). Thus, as expected the *E* values increased significantly with increase in (T:NB) from (1:4) to (1:2) for both cCMC and NorCMC.

For each bioink formulation, we compared the cell viability with culture time for each cell line. For instance, hMSC viability decreased from 96% at Day 1 to 90% at Day 4, and to 84% at Day 7 for MeHA control group. Note that MeHA is not degradable, and this could potentially eliminate the ability of the hMSCs to spread and proliferate. However, hMSC viability was not significantly different for other degradable formulations, such that cell viability remained stable within 92-93% interval for cCMC (1:4), 95-97% interval for NorCMC (1:4), and 97-93% interval for NorCMC (1:2). When NIH 3T3 cells

are considered, cell viability decreased for NorCMC (1:2) from 92% at Day 1 to 83% at Day 7, and for MeHA from 97% at Day 1, to 88% at Day 4, and to 87% at Day 7. Cell viability did not show a significant change and remained constant within 93-83% for cCMC (1:4) and within 91%-83% for NorCMC (1:4). For HUVECs, cell viability decreased from 93% at Day 1 to 86% at Day 7 for NorCMC (1:4) and from 91% at Day 1 to 86% at Day 7, whereas the changes were not significant between Day 1 and Day 4 (including cCMC group), and Day 4 and Day 7. Cell viability for MeHA group remained within 97-93%. Our results showed that the decrease in cell viability for the NorCMC and cCMC formulations is not trivial, and dependent on the cell type and culture period. As we did not use any commonly used cell-adhesive peptides (such as RGD), we believe that cell variability could potentially be further enhanced, if needed. We also compared the cell viability between sample groups (bioink formulations) for each cell line at each culture Day. For hMSCs, cell viability for cCMC (92%) was lower than that for NorCMC (1:4) (97%) at Day 1. No significant difference was observed between sample groups at Day 4. However, cell viability for MeHA (84%) was lower than that for NorCMC (1:2) (93%) and for NorCMC (1:4) (97%) at Day 7. For 3T3 cell line, cell viability for MeHA (97% at Day 1, 87% at Day 7) was higher than that for NorCMC (1:2) (92% at Day 1, 83% at Day 7) and NorCMC (1:4) (91% at Day 1, 83% at Day 7) at Day 1 and Day 7. When HUVECs are considered, cell viability for MeHA (98%) was higher than cell viability for NorCMC (1:2) (91%) and NorCMC (1:4) (93%) at Day 1. No significant difference was observed between sample groups at Day 4 and Day 7. We believe that a lower cell viability at Day 1 could potentially indicate issues during printing process, such as cell damage due to shear or light exposure. One way to avoid this is to increase the bioink viscosity to protect

the cells. For instance, MeHA bioinks were much viscous leading to higher cell viability at Day 1.

The 15% cCMC (1:4) sample degraded and disintegrated by Day-7 while the similar NorCMC (1:4) did not because of the reduced degradation afforded by the amide connectivity versus the ester groups connecting the norbornenes to the CMC. Hydrolytic degradation of the cCMC bulk hydrogels was previously reported, such that for 4% cCMC with (T:NB) equal to (1:4), 30% mass loss was reported within 24 hour incubation, which increased to ~50% after 7 days [236]. This behavior was not observed for NorCMC hydrogels [237]. In good agreement with the swelling data (see above), we observed differences in the confocal side view images (**Figure 3.7B**) of the 3D printed samples. For instance, vertical distribution of the cells within NorCMC (1:4) was about twice thicker than NorCMC (1:2), which corresponded to the difference in the swelling ratio (23.4 for NorCMC (1:4), 12 for NorCMC (1:2)). For cCMC (1:4), cells distributed more sparsely when compared to that for NorCMC. We believe that this was due to hydrogel degradation as discussed above.

3.5 Conclusions

In conclusion, we report a two norbornene-modified cellulose-based macromers as novel bioink materials. Polymer concentration and thiol: norbornene ratio (T:NB) were optimized to prepare printable bioink formulations from cCMC (with (T:NB) = (1:2) and (1:4)) and NorCMC (with (T:NB) = (1:4)). All the ink formulations were able to encapsulate cells (hMSCs, NIH 3T3 fibroblasts, and HUVECs), and to be printed as cell-laden scaffolds. We believe that these two cellulose-based macromers broaden the bioink

library and could be further modified to render more desired properties in further practice and applications.

CHAPTER 4

POLYESTER-BASED INK PLATFORM WITH TUNABLE BIOACTIVITY FOR 3D PRINTING OF TISSUE ENGINEERING SCAFFOLDS

This chapter has been adapted from the publication:
S. Ji, K. Dube*, J.P. Chesterman, S.L. Fung, C.Y. Liaw, J. Kohn, M. Guvendiren, Polyester-based ink platform with tunable bioactivity for 3D printing of tissue engineering scaffolds, Biomaterials Science 7(2) (2019) 560-570. *Co-1st Author*

4.1 Introduction

Over the last decade, 3D printing has become a promising manufacturing approach for a wide range of medical applications, including dentistry, tissue engineering and regenerative medicine, medical devices, anatomical models, and pharmaceutics [9, 46, 238]. 3D printing enables fabrication of custom-designed and patient-specific tissue engineering scaffolds and devices using the patient's own medical images, which is not possible with conventional scaffold fabrication techniques [82, 239-244]. In addition, conventional techniques generally lack precise control of pore size, geometry, interconnectivity, spatial distribution, and the overall scaffold architecture [245-247]. These are crucial parameters for a biomaterial to promote the vascularization and tissue ingrowth that are necessary to establish functional integration of the scaffold [190, 191, 248, 249]. However, most devices currently printed using polymeric biomaterials only serve as a structural support; they permit, but do not promote, biological function [250, 251]. This limitation is due to the lack of bioactivity of common printable polymers, such as poly(lactic acid) (PLA) and polycaprolactone (PCL). Due to their thermoplastic and semi-crystalline behavior, PLA and PCL can be easily extruded as filaments for fused deposition (FDM) printing or directly printed from melt using direct ink writing (DIW). Semi-crystalline behavior contributes to dimensional stability during melt to solid

transition and to mechanical properties (stiffness). Both PLA and PCL are extensively used to 3D print tissue fixation devices and tissue engineering scaffolds, in particular for musculoskeletal tissue [252, 253]. Although significant progress has been made to develop novel printable soft material platforms (including hydrogels and elastomeric systems) [70, 168, 254-259], the progress in biodegradable "stiff" polymers is very limited.

From a materials-perspective, a polymeric biomaterial should meet the requirements for printing to be considered an "ink". Rheological properties of the polymers are crucial to determine their printability. For extrusion-based printing, the polymer melt must flow at the print temperature (T_p) (usually below 250 ˚C for commercially available printers); thus, the loss modulus (G'') must be greater than the storage modulus (G') at T_p.[13] The melt viscosity should be below 10^6 mPa·s to allow flow under applied pressure (usually ≤110 psi for commercially available printers) [260]. In addition, the polymer must have a reversible and fast melt to solid phase transformation (within minutes) to rapidly melt in the hot nozzle and to rapidly solidify when extruded from the nozzle [261].

In addition to printability, the ideal polymeric biomaterial should have sufficient mechanical properties (stiffness, toughness, etc.) to provide structural integrity, thereby enabling direct implantation, and should be biodegradable to allow replacement of the scaffold by newly grown tissue [262-265]. The latter requires the use of polymers that hydrolytically or enzymatically degrade to biocompatible, resorbable monomers that can be easily excreted from the body.

Finally, polymeric biomaterials often require bioactivity to control cell function, including cell migration (infiltration), proliferation, and phenotype preservation or differentiation [15, 266-268]. Naturally occurring polymers usually display inherent

bioactivity, which is not the case for synthetic polymers. Thus, it is of great interest to design functionalizable synthetic polymers for 3D printing. Polymers can be functionalized at the end groups or along the backbone by adding pendant reactive groups, such as carboxylic acids [269], amines [270], or hydroxyls [271], One of the most commonly utilized approaches is click-based conjugation chemistry using click-ready pendant groups, such as alkenes, alkynes, azides, and epoxides [272, 273], Click chemistry has been employed for a wide range of applications including bioconjugation, labelling, surface functionalization, polymer synthesis and modification, and hydrogel modification [272, 274-276],

In this study, we developed a novel platform of 3D printable biodegradable polymers with tunable bioactivity via click-based chemistry for extrusion-based printing, with printability and stiffness comparable to PLA. A wide range of tyrosine-derived polycarbonates with tunable properties have been developed previously [277-281], In this work, the synthetic design was based on 4-hydroxyphenethyl 2-(4-hydroxyphenyl)acetate (HTy), which is an ester derived from Tyrosol and 2-(4-hydroxyphenyl)acetic acid. Both compounds are naturally occurring organic molecules found in olive oil [282, 283], HTy has been shown to be antioxidant, anti-stress, and antibacterial [282, 283], *p*-Phenylenediacetic acid (PDA) was incorporated into the synthetic design to tune thermal processability by enhancing crystallinity via π-π stacking interactions. To enable functionalizability, glutamic acid derivatives were incorporated into the synthetic design without deteriorating printability and stiffness. Glutamic acid is a diacid with a pendant amine group, which can be easily modified to incorporate various functional groups. In this study, we focused on alkyne and alkene functionality for commonly utilized click-based

conjugation chemistry.

To demonstrate the utilization of this novel ink platform, osteogenic differentiation of stem cells was studied using 3D printed scaffolds. 3D printed scaffolds were functionalized with azide-Heparin (az-Heparin) via click chemistry. Heparin is a linear polysaccharide found in most biological tissues. Heparin is known to sequester growth factors, enzymes, and matrix proteins. Thus, it is extensively used for the sustained release of growth factors including bone morphogenetic protein-2 (BMP-2) (for up to 20 days) [284, 285] to enhance bone regeneration.[286] Our results showed a significant increase in osteogenic differentiation of stem cells when the scaffolds were tethered with heparin-bound BMP-2.

4.2 Experimental

4.2.1 Synthetic Procedures

4.2.1.1 Monomer Synthesis. Monomers including 4-hydroxyphenethyl 2-(4-hydroxyphenyl) acetate (HTy) (**Figure 4.1A**), hex-5-enoylglutamic acid (Gluhexenamide) (**Figure 4.1B**), and pent-4-ynoylglutamic acid (Glupentynamide) (**Figure 4.1C**) were synthesized as described in the experimental section of **Appendix C**.

4.2.1.2 Polymer Synthesis. A general procedure for the polymer synthesis ((**Figure 4.1**) is provided here and further details can be found in the Experimental Section of the **Appendix C**. In a round bottom flask, 1 equivalent of diol, 0.97 combined equivalents of diacid, and 0.33 equivalents of 1,4-dimethylpyridinium p-toluenesulfonate (DPTS) were combined with dichloromethane (DCM) and magnetically stirred for 15 min. The stirring reaction mixture was cooled for 30 min in an ice bath and then 2.1 equivalents of N,N'-

diisopropylcarbodiimide (DIC) were added. The stirring reaction mixture was kept in an ice bath for 1 hour and then allowed to gradually warm to room temperature overnight. After 16 hours, the reaction mixture was precipitated by gradually adding isopropanol (5X DCM volume) while stirring. The precipitate was collected by vacuum filtration, redissolved in DCM, and reprecipitated using isopropanol, twice. The final precipitate was collected by vacuum filtration and dried in a vacuum oven at 40 ˚C for 48 hours.

4.2.2 Monomer and Polymer Characterization

The synthesized monomers and polymers were characterized by ^{1}H NMR spectroscopy using Varian 400 MHz and 500 MHz NMR spectrometers with dimethyl sulfoxide-d_6 (DMSO-d_6) as solvent and peak shifts referenced to an internal tetramethylsilane standard. The molecular weight of the monomers was determined by electrospray ionization-mass spectroscopy (ESI-MS, Thermo Finnigan LCQ Duo). The number average molecular weight (M_n), weight average molecular weight (M_w), and the molecular weight distribution of the polymers were determined using gel permeation chromatography using a Waters 2695 GPC apparatus with a guard and 2 columns. Samples were dissolved in HPLC grade dimethylformamide (DMF) at a 2 mg/mL concentration, filtered through a 0.2 μm syringe filter, and run at 25 °C using HPLC grade DMF with 0.1% trifluoroacetic acid (TFA) as the eluent. Molecular weights were calculated relative to polystyrene standards (M_w = 7.2-526 kDa).

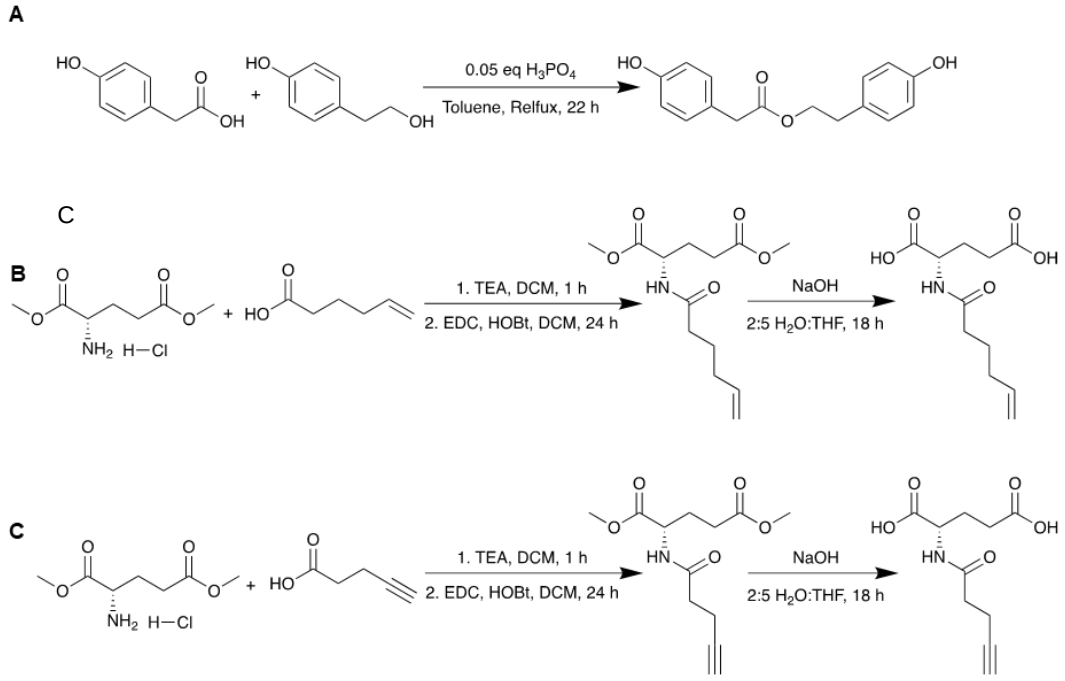

Figure 4.1 (A) Synthesis of HTy. (B) Synthesis of gluhexenamide. (C) Synthesis of glupentyamide.

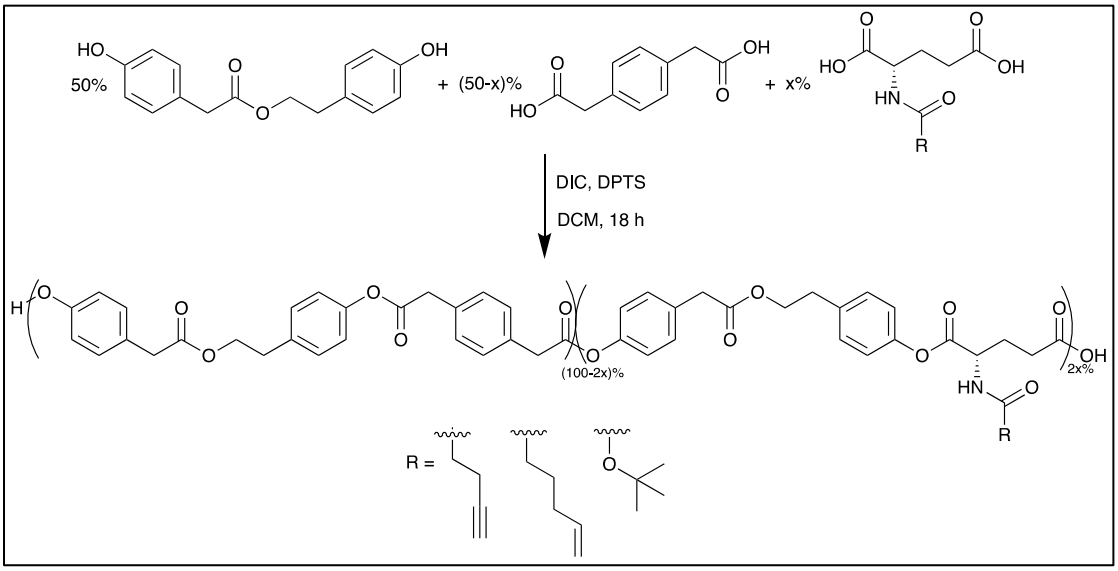

Figure 4.2 General polymer synthesis.

4.2.3 Thermal Properties

Thermal properties including the glass transition temperature (T_g) and melting point (T_m) were determined by differential scanning calorimetry (DSC) from the second heating scan at a 10 ˚C/min heating rate using a Mettler Toledo DSC821. The thermal degradation of the polymers was studied by thermogravimetric analysis (TGA, Mettler Toledo). The temperature at which mass loss began in the thermogram was considered as the thermal degradation temperature (T_d).

4.2.4 Compression Molding

Polymer films were fabricated using a Carver press (Carver 2625) at T_g+50 ˚C or T_m + 10 ˚C. Briefly, 0.3 g of polymer powder was placed between two Kapton films in a preheated steel mold, placed in the Carver press, and compressed using 1000 psi. The thickness of the films was adjusted by using spacer shims.

4.2.5 Melt Rheology

Melt rheology (Kinexus Ultra$^+$, Malvern Instruments) was used to study solid to melt transition behaviour and temperature dependent melt viscosity of the polymers. Compression molded polymer films (500 μm in thickness) were tested using a 20 mm diameter plate at a constant frequency (1 Hz) with increasing temperature (1 ˚C/min) up to 200 ˚C. Storage modulus (G′), loss modulus (G″), and melt viscosity were recorded with increasing temperature. The solid to melt transition temperature was defined as the temperature where G′=G″.

4.2.6 Mechanical Properties

Mechanical properties of the polymer films were tested using a mechanical tensile tester (MTS Sintech/5D Universal Testing Machine) with a 10 N load cell and a 10 mm/min

displacement rate. The tensile (Young's) modulus was calculated from the slope of the tangent drawn at the linear portion of the stress strain curve (0 to 2%). Five samples of each polymer were tested.

4.2.7 Hydrolytic Degradation

Hydrolytic degradation was studied by incubating scaffolds (5 mm diameter discs) in 1 mL Dulbecco's phosphate-buffered saline (DPBS) with 0.01% sodium azide at 37 ˚C. The solution was changed weekly for the duration of the study. At each time point, three scaffolds were separated, washed with DI water, lyophilized, and characterized gravimetrically for loss in mass and by GPC for M_n and M_w.

4.2.8 Functionalizability

The reactivity of the polymers with glutamic acid derivatives was characterized in bulk (using polymer solutions) and/or on the surface (using compression molded films). 1*H*,1*H*,2*H*,2*H*-perfluorodecanethiol was used to investigate reactivity in the bulk and on the surface for HP5GH and in bulk for HP5GP. Surface reactivity for HP5GH and HP5GP was also investigated using bovine serum albumin (BSA) and az-Heparin, respectively. Az-Heparin was synthesized by reacting heparin with imidazole sulfonyl azide (azo transfer reagent) as described in the **Appendix C** [287]. Characterization was done by X-ray photoelectron spectroscopy (XPS) for surface and ^{19}F NMR for bulk. A quartz crystal microbalance (Q-sense) was used to monitor the conjugation reaction of az-Heparin and physical adsorption of BMP-2 on polymer films in real time and the change in frequency was converted to a change in mass using the well-known Sauerbrey equation [288].

4.2.9 3D Printing of Scaffolds

A 3D Bioplotter® Starter Series (EnvisionTEC GmbH, Germany) was used to print the scaffolds. The 3D digital model for the scaffolds was designed and saved as an STL file using Autodesk® Fusion 360™. The scaffold was designed as a solid cylinder (1 mm in height and 9 mm in diameter) to fit in a 48-well plate. Perfactory RP software was used to slice the STL file with 250 μm layer height. The sliced file was transferred to 3D Bioplotter® and a linear infill pattern with 0.75 mm spacing was created with alternating 0° and 90° rotation between layers. To begin printing, polymer powder was loaded into a stainless-steel syringe and heated to a printing temperature determined by the thermal properties of each polymer. Line tests were performed to determine the optimum printing parameters, including temperature, pressure, and speed. Briefly, a built-in line test protocol was used to print individual struts using a range of print pressures and speeds at a predefined print temperature. Print parameters were optimized to print struts with a 350 μm diameter. Scaffolds were characterized by scanning electron microscopy (SEM, Jeol).

4.2.10 Preparation of Scaffolds for Cell Culture

To investigate stem cell attachment and proliferation, two sets of scaffolds were printed from PLA, HP, HP5BG, HP5GP, and HP5GH. Scaffolds were sterilized by immersion in 75% ethanol for 30 min, followed by irradiation with a germicidal UV lamp for 1 h per side. After sterilization, one set was incubated with fibronectin from bovine plasma (20 μg/mL, Sigma), while the other set was incubated in Dulbecco's phosphate-buffered saline (DPBS). After the incubation solutions were aspirated, the scaffolds were rinsed with DPBS three times and transferred into non-treated 48-well plates and maintained in 0.5 mL

of growth media per well for 2 h prior to cell seeding.

For differentiation studies, four groups of HP5GP scaffolds were used. Two of the groups were functionalized with az-Heparin (HP5GP-Heparin) by incubating the scaffolds in 200 μL az-Heparin solution (0.15 μg/mL az-Heparin in DI water) with 10 μL of copper sulfate pentahydrate (45 mg/mL) and 10 μL of sodium ascorbate (112.5 mg/mL) for 24 h. The scaffolds were washed with DPBS 3 times. One of these sample groups was further functionalized with BMP-2 (HP5GP-Heparin-BMP2) by incubating the scaffolds in 200 μL BMP-2 solution (7.5 μg/mL) for 1 h. One of the HP5GP groups was directly incubated with BMP-2 (7.5 μg/mL) for 1 h, washed with DPBS (3X), and used as a control. All scaffold groups (HP5GP, HP5GP-Heparin, HP5GP-Heparin-BMP2, and HP5GP-BMP2) were transferred into growth media 2 h prior to cell seeding.

4.2.11 Cell Culture and Characterization

Human mesenchymal stem cells (hMSCs, Lonza) were cultured in growth media (MEM-α (minimum essential medium) supplemented with 10% fetal bovine serum (FBS, Gibco) and 1% penicillin streptomycin). hMSCs (115,000 cells/mL, passage 3) were seeded from the top surface (300 μL per scaffold corresponding to 12,500 cells/cm^2) and incubated at 37 ˚C for 60 min to allow for cell attachment. Scaffolds were gently turned upside down and hMSCs were seeded again (300 μL at 115,000 cells/mL) from the top. For cell attachment and proliferation studies, the cells were cultured for 14 days in growth media. For differentiation studies, after 2 days of culture in growth media, the media was replaced with osteogenic induction media (Lonza) and the cells were cultured up to 21 days. Media was refreshed every 3 days. For control studies with soluble BMP-2, 1 μL of BMP-2 solution (165 μg/mL in DI water) was added into the media with each media change.

An alamarBlue cell viability assay (Invitrogen) was used to investigate cell viability at 2, 4, 7 and 10 days of culture for each group (6 samples per group). To quantify double stranded DNA (dsDNA), Quant-iT™ PicoGreen™ dsDNA assay kit (Invitrogen) was used. For this purpose, 3 samples per group were collected at culture Day 1, 4, 7, 10, and 14. The cells from each sample group were lysed and stored at -80 ˚C until all time points were collected for quantification. For both assays, an Infinite M200 Pro (Tecan) plate reader was used.

To visualize cells on the scaffolds, cells were washed with DPBS, fixed in 4% formalin for 15 min, and incubated in Triton X-100 solution (0.25% Triton X-100 in DPBS) for 15 min to permeabilize the cell membrane. Cells were stained for F-actin using Alexa Fluor™ 488 Phalloidin (1:40 in DPBS, Molecular Probes) and nuclei by 4', 6-diamidino-2-phenylindole (1:2000 in DPBS, DAPI, Invitrogen). For differentiation studies, cells were stained for alkaline phosphatase (ALP) with Fast Blue RR/naphthol solution (Sigma), for calcium deposition with alizarin red (AR) or immunostained for osteocalcin (OC). For fluorometric quantification of AR staining, cells were de-stained using 10% cetylpyridinium chloride in 10 mL sodium phosphate (10 mM, pH 7). For immunostaining, cells were rinsed with DPBS (3X) and incubated in blocking solution (10% goat serum in DPBS) for 30 min after the permeabilization step. Samples were incubated with the OC primary antibody (1:200, monoclonal mouse, Fisher Scientific Co.) in staining solution (3% BSA, 0.1% Tween-20, 0.25% Triton-X) overnight at 4 ˚C. After washing with 3% BSA solution, cells were incubated in Alexa Fluor 488 rabbit anti-mouse secondary antibody (1:100, Fisher Scientific Co.) in a 3% BSA solution. Cells were imaged by confocal microscopy (confocal and 2-photon system, Leica). The nuclei of the OC and ALP stained

cells were counted using ImageJ to determine OC and ALP positive cells.

4.2.12 Statistical Analysis

The data were analysed using KleidaGraph. Data are presented as mean ± standard deviation. ANOVA with Tukey's HSD post hoc test of means was used to make comparisons between sample groups. ($n \geq 3$ samples per group).

4.3 Results and Discussion

4.3.1 Monomer and Polymer Synthesis

The HTy monomer was synthesized via Fischer esterification from Tyrosol and 2-(4-hydroxyphenyl)acetic acid. HTy degrades hydrolytically to form Tyrosol and 2-(4-hydroxyphenyl)acetic acid **(Figure 4.1)**. Since HTy contains phenyl rings, polymers that incorporate it tend to show semi-crystalline behaviour due to π-π stacking interactions. To enhance the π-π stacking interactions of HTy-containing polymers and hence their processability, *p*-phenylenediacetic acid (PDA) was introduced into the polymer design. Functionalizability was achieved by incorporating amide derivatives of glutamic acid (GR), which were synthesized by reacting the dimethyl ester of glutamic acid with alkene or alkyne carboxylic acids **(Figure 4.1)**. Alkene or alkyne functionality was chosen to enable click-chemistry for tethering bioactive cues. Poly(HTy-50%PDA) (HP), poly(HTy-45%PDA-co-HTy-5%Gluhexenamide) (HP5GH), poly(HTy-45%PDA-co-HTy-5%Glupentynamide) (HP5GP), and poly(HTy-45%PDA-co-HTy-5%BocGlu) (HP5BG) were successfully synthesized by condensation polymerization of selected combinations of HTy, PDA, and GR using DIC and DPTS as a catalyst **(Figure 4.1)**. Note that HTy undergoes 1:1 step growth reaction with PDA and GR during polymerization. Thus, the

general formula for the functionalizable polymers is poly($HTy_{(0.5-x)}$-$PDA_{(0.5-x)}$-co-HTy_x-GR_x). Although we synthesized three polymer compositions with x = 0.01, 0.05, and 0.10, x=0.05 was used in this study due to favourable thermal properties, which will be discussed below. For simplicity, functionalizable polymers are referred to using the following format: HP5GR, where H, P, and GR denote HTy, PDA, and GR, and the number (5) indicates the mole percentage of functionalizable GR group. The M_w and *PDI* of each polymer are given in **Table 4.1**. NMR results are given in **Appendix C Figure C.1**.

Table 4.1 Properties of the Polymers

Polymer	M_w[a] (kDa)	PDI[a]	T_g[b] (˚C)	T_{m1}[b] (˚C)	T_{m2}[b] (˚C)	T_D[c] (˚C)	E_T[d] (GPa)	σ_y[d] (MPa)	η[e] (mPa.s)	G' fold change[e]	%M_w Retention[f]
p(HTy)	181	1.8	54	-	-	350	2.4(±0.3)	38(±7)	$5x10^6$	1.1	-
HP	143	1.7	50	131	147	320	2.1(±0.3)	28(±3)	$5x10^5$	3.5	88
HP5BG	141	1.7	46	125	141	330	1.9(±0.1)	40(±3)	$3.3x10^2$	4.0	70
HP5GH	126	1.6	47	128	143	320	2.2(±0.1)	34(±6)	$1.8x10^3$	4.0	18
HP5GP	129	1.6	50	127	144	320	2.3(±0.1)	38(±2)	$2.4x10^3$	4.0	18

[a]From DMF GPC, relative to PS standards. [b]From DSC measurements. [c]From TGA. [d]From tensile tests using compression molded films. [e]From melt rheology using compression molded films (η measured at 180 ˚C). [f]From hydrolytic degradation tests (8-week point) using DMF GPC

4.3.2 Thermal and Mechanical Characterization

Thermal properties of the polymers are summarized in **Table 4.1**. For poly(HTy carbonate) (p(HTy)), the T_g was observed at 54 ˚C. A shallow melting peak observed at 130 ˚C during the first heating cycle disappeared in the second heating cycle, thus indicating an amorphous behaviour. The lack of crystalline behaviour could be due to the rigidity of the carbonate bonds in the polymer backbone preventing the randomly oriented HTy repeating

units from aligning for π-π stacking interactions. When PDA was incorporated into the polymer design to form HP, the T_g dropped slightly to 50 ˚C and two distinct melting transitions were observed at T_{m1} = 131 ˚C and at T_{m2} = 147 ˚C (**Figure 4.3**). Replacing the carbonate bonds with PDA increases backbone flexibility and the appearance of two melting points may indicate the presence of distinct crystalline regions formed by either HTy or PDA π-π stacking interactions. HP5BG, HP5GH, and HP5GP all have similar thermal properties to HP with T_g, T_{m1}, and T_{m2} values within 4-6 ˚C (**Figure 4.3**). All of the polymers decomposed at temperatures between 320-350 ˚C. Note that polymers containing 5 mole % GR were used in this study as the resulting polymer becomes amorphous for 10 mole% GR. The average tensile Young's modulus values of the polymers were in the range of 1.9 to 2.4 GPa with yield stress values from 28 to 40 MPa **(Table 4.1)**. Both values were not statistically different when compared for each polymer.

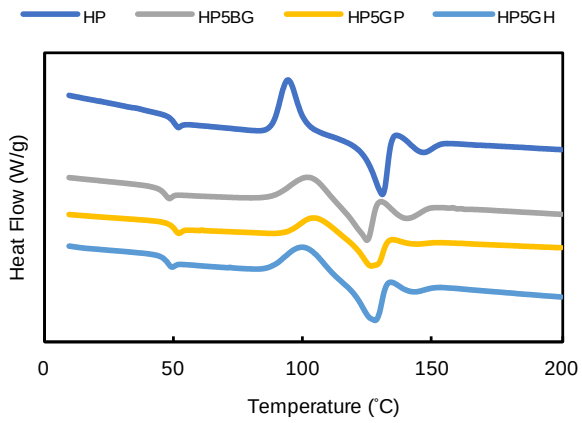

Figure 4.3 DSC thermograms for the polymers.

4.3.3 Hydrolytic Degradation

Polyesters undergo hydrolytic degradation due to the ester bonds in their backbone. The hydrolytic degradation of compression molded polymer films (HP, HP5BG, HP5GP, and HP5GH) was studied at 37 ˚C in DPBS **(Figure 4.4)**. For HP, a steady decrease in M_w was observed between weeks 5 and 22, reaching undetectable M_w values after 22 weeks. For HP5BG, a generally linear decrease in M_w was observed for the entire 25-week study. The M_w decreased much faster for HP5GP and HP5GH, such that only 18% M_w was retained after 8 weeks. We believe that this result could be due to less bulky side groups as compared to Boc in HP5BG. There are only a few semi-crystalline polymers that show a comparable high rate of degradation, such as poly(glycolic acid) (PGA) (degradation rate of 3-4 months) [289]. There was no significant mass loss for HP and HP5BG, which could be due to the hydrophobic nature of the polymer limiting the solubility of the degraded chains **(Figure 4.4B)**. The rate of mass loss for HP5GH and HP5GP was 3% and 2.5% per week, respectively. We did not observe any significant change in Young's modulus values of HP5GH and HP5GP up to 4 weeks (**Appendix C, Figure C.6**).

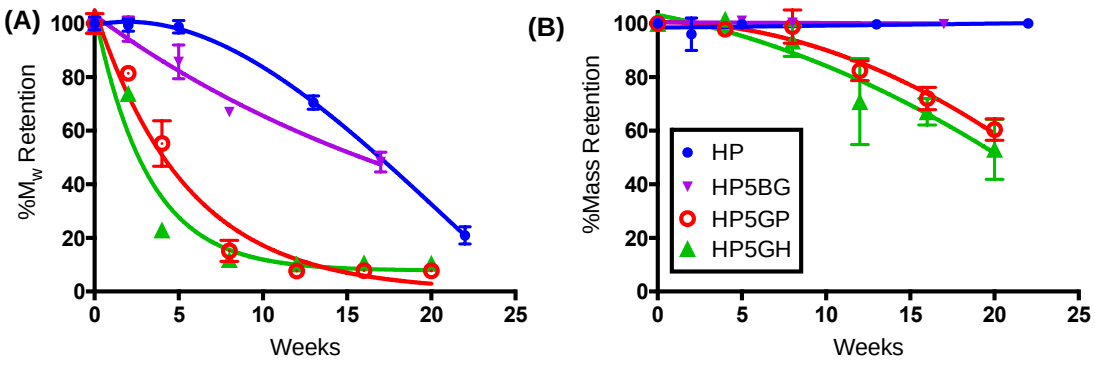

Figure 4.4 Hydrolytic degradation of polymers over 25 weeks at 37 ˚C in DPBS. (A) Percent retained molecular weight (% M_w) with time. (B) Percent mass retention with time.

4.3.4 Functionalizability

In this study, three distinct polymers were developed with pendent reactive groups. HP5GH and HP5GP have alkene and alkyne pending groups capable of click chemistry. The alkyne group can participate in copper catalysed alkyne-azide cycloaddition (CuAAC) reaction, utilized extensively in the literature [272, 274-276]. The alkene group can react with sulfhydryl containing compounds in the presence of a photoinitiator and UV light or via Michael-type addition reaction [290]. HP5BG contains Boc-protected amine groups capable of carbodiimide chemistry, which also enables functionalization with a wide range of side chain derivatives to further tether bioactive cues.

The reactivity of the alkene-containing HP5GH was tested by using a small thiol-containing molecule (1H,1H,2H,2H-perfluorodecanethiol) and a large protein, BSA (66.5 kDa), containing cysteine residues (**Figure 4.5**). A highly fluorinated small molecule enabled the study of the reactivity of the polymer in solution via ^{19}F NMR and the reactivity of the polymer surface (using compression molded films) via XPS. ^{19}F NMR showed that approximately 94% of the alkene bonds were converted to thioether bonds after UV irradiation in the presence of a photoinitiator, Irgacure 2959 (**Appendix C, Table C.1**). For the surface reaction, XPS data showed that the fluorine peak was only observed in the presence of UV light exposure, whereas the peak was missing for HP5GH sans UV exposure and for HP (without the pendent alkene group) with UV exposure (**Figure 4.5A**). The effects of thiol concentration, photoinitiator concentration, and UV irradiation time on the reaction yield for compression molded films were studied in detail, and the results are summarized in **Table C.1**. QCM studies indicated that 700 ng/cm^2 of BSA was chemically tethered onto the surface of HP5GH with UV exposure, which was significantly more than

the 100 ng/cm^2 of BSA physically adsorbed onto the surface in the absence of UV exposure (**Figure 4.5B**). The reactivity of the alkyne-containing HP5GP was studied via a CuAAC reaction using az-Heparin. The reaction was monitored in real-time by QCM. 1 μg/cm^2 of az-Heparin was found to be conjugated to the surface of the polymer within 1 hour **(Figure 4.6)**. Although az-Heparin was found adsorb onto the HP5GP and HP surface (polymer without a reactive pendent group) in the absence of the catalyst, the amount of adsorbed az-Heparin was significantly lower: 480 ng/cm^2 for HP5GP and 100 ng/cm^2 for HP (**Appendix C, Figure C.7**). Heparin is known to bind and release growth factors such as bone morphogenetic protein-2 (BMP-2). To further investigate the activity of tethered heparin, we studied the interaction of it with BMP-2. Approximately 1 μg/cm^2 of BMP-2 was found to bind to the heparinated polymer surface and remained bound after rinsing with DPBS for 10 h, indicating a strong association of BMP-2 with heparin. The ionic interaction between the BMP-2 and heparin was disrupted when a surfactant (SDS) was introduced.

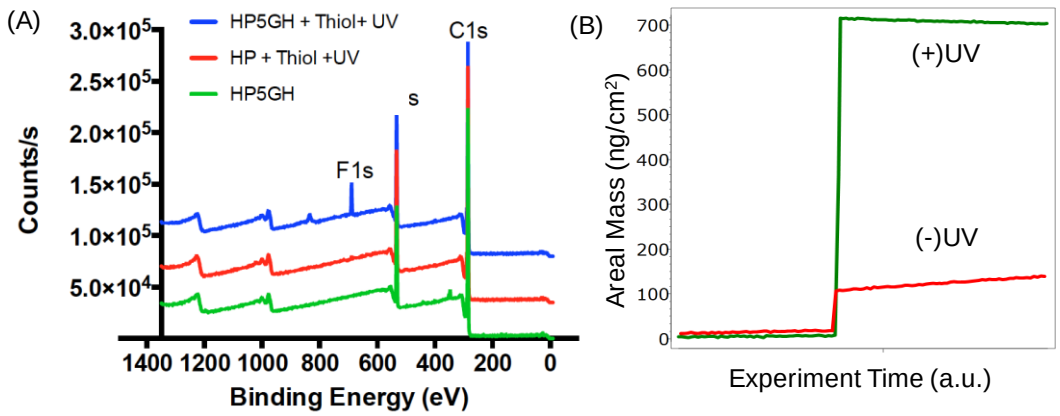

Figure 4.5 (A) XPS spectra for HP5GH (green), HP reacted with 1*H*,1*H*,2*H*,2*H*-perfluorodecanethiol under UV light (red), and HP5GH reacted with 1*H*,1*H*,2*H*,2*H*-perfluorodecanethiol under UV light (blue). (B) QCM data showing the change in areal mass with time for HP5GH covered with BSA solution in the presence (+) or absence (-) of UV light.

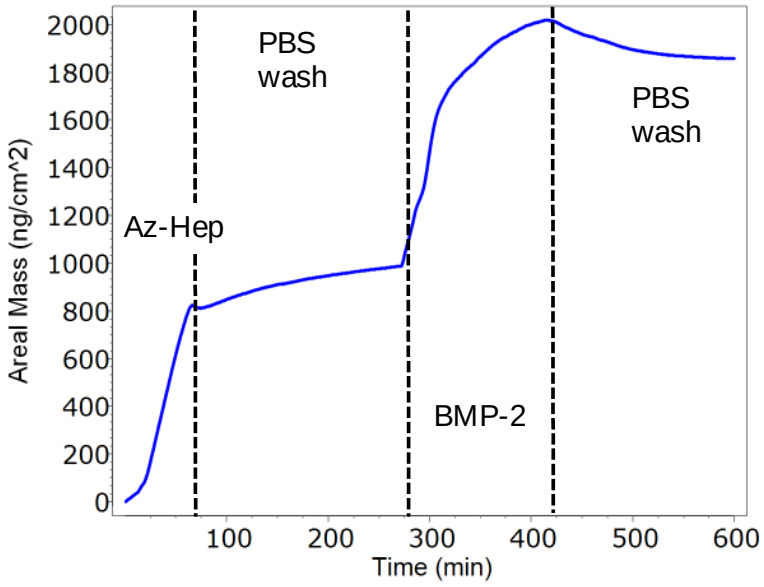

Figure 4.6 QCM data showing the change in frequency with time for HP5GP. Az-Heparin was flowed over HP5GP film for 60 min, followed by DPBS for 240 min, then BMP-2 for 100 min, and finally DPBS.

4.3.5 Rheological Characterization

The rheological properties of polymers are crucial to determine their printability. For extrusion-based printing at elevated temperatures, the polymer melt must flow at the print temperature (T_p), thus, the loss modulus (G'') must be greater than the storage modulus (G') at T_p. In addition, the polymer must have a fast melt to solid phase transformation (within minutes) to rapidly melt in the hot nozzle and rapidly solidify when extruded from the nozzle [13, 261]. For instance, PLA, the most widely used polymer in 3D printing, shows a fast phase transformation, indicated by a sharp drop in G' within a very narrow temperature window **(Figure 4.7).** For commercial PLA, solid to melt transition occurred at T_{sm} = 180 ˚C and melt viscosity was equal to 8.4×10^5 mPa·s above 180 ˚C (usual printing temperature). For p(HTy), T_{sm} = 140 ˚C, with a shallow drop in G' and a relatively high melt viscosity value ($\eta = 5\times10^6$ mPa·s). For HP, η was significantly reduced to 5×10^5 mPa·s with a significant drop in G' during solid-to-melt transition (at T_{sm} = 150 ˚C) **(Figure 4.7)**, which is consistent with the impact of incorporating PDA on the thermal properties. Note that the melt rheological behaviour of HP was similar to PLA. Functionalizable polymers showed extended transition regions with T_{sm} = 150 ˚C, 140 ˚C, and 138 ˚C, and $\eta = 3.3\times10^2$ mPa·s, 1.8×10^3 mPa·s, and 2.4×10^3 mPa·s (measured at 180 ˚C), for HP5BG, HP5GH, and HP5GP, respectively **(Figure 4.7)**. This result could be due to hydrogen bonding interactions between the amide groups present in the glutamic acid derivatives. The melt rheological data for all polymers are given in **Table 4.1**.

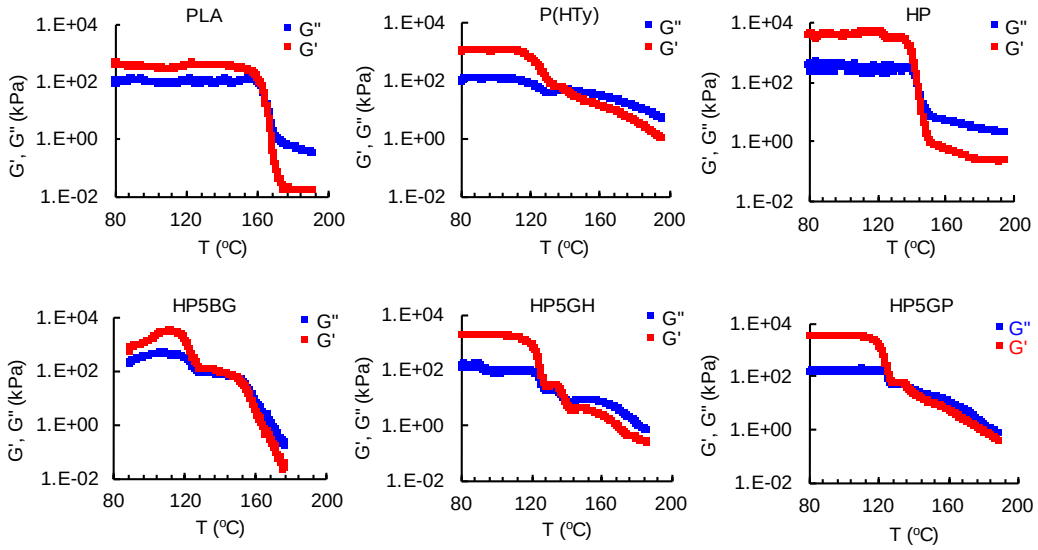

Figure 4.7 Plots showing the change in storage modulus (G') and loss modulus (G") of the polymers with temperature (T). Solid to melt transition temperature is defined as the temperature where G'=G".

4.3.6 3D Printing

An EnvisionTEC 3D Bioplotter®, an extrusion-based printer, was used to print the polymers. Initial extrusion tests were performed to determine the lowest print temperature (T_p) and polymer incubation time to equilibrate the print temperature (t_e). Following this study, printing parameters including print pressure (P) and print speed (v_p) were determined by performing line tests using two needle sizes. The summary of printing parameters to create 350 μm diameter print lines (struts) is given in **Table 4.2**. 3D scaffolds printed from HP, HP5BG, HP5GP, and HP5GH showed identical resolution when compared with scaffolds printed from PLA **(Figure 4.8)**. SEM images showed self-supporting scaffolds constructed from uniform 350 μm diameter struts.

Table 4.2 Printing Parameters, including Needle Diameter (d), Print Temperature (T_p), Time to Equilibrate Temperature (t_e), Print Pressure (P), and Print Speed (v_p)

Polymer	d (mm)	T_p (°C)	t_e (h)	P (bar)	v_p (mm/s)
PLA	0.3	200	0.5	7	2
HP	0.3	190	1	7	2
HP5BG	0.3	170	1	7	2
	0.4	170	1	6	13
HP5GH	0.3	170	1	7	3
HP5GP	0.3	175	0.5	7	1.5
	0.4	175	1	6	4

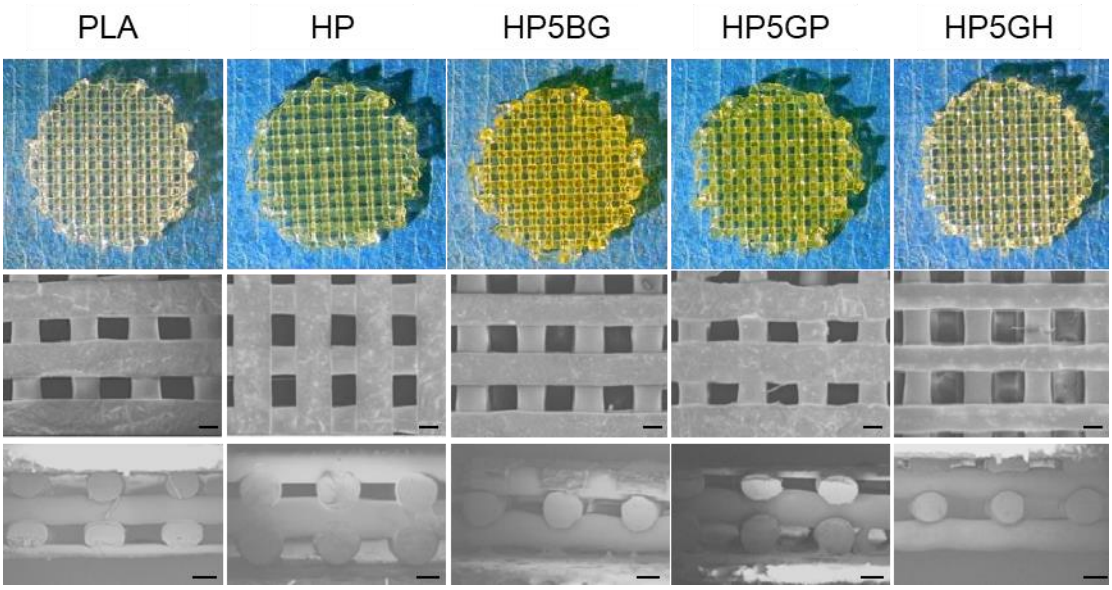

Figure 4.8 Top row: 3D printed scaffolds from PLA, HP, HP5BG, HP5GP, and HP5GH. The corresponding SEM images including from top view and cross-section are shown in middle and bottom row, respectively. Scale bars are 200 μm for SEM images.

4.3.7 Stem Cell Culture and Osteogenic Differentiation

hMSCs were cultured on 3D printed scaffolds for up to 14 days. Cells showed gradually increasing metabolic activity for the first 10 days, and total cell number (measured by dsDNA content) increased gradually starting from days 4 and 7 **(Figure 4.9)**. Confocal images of the scaffolds at Day 14 showed that cells had attached and spread uniformly to cover the struts **(Figure 4.9C)**.

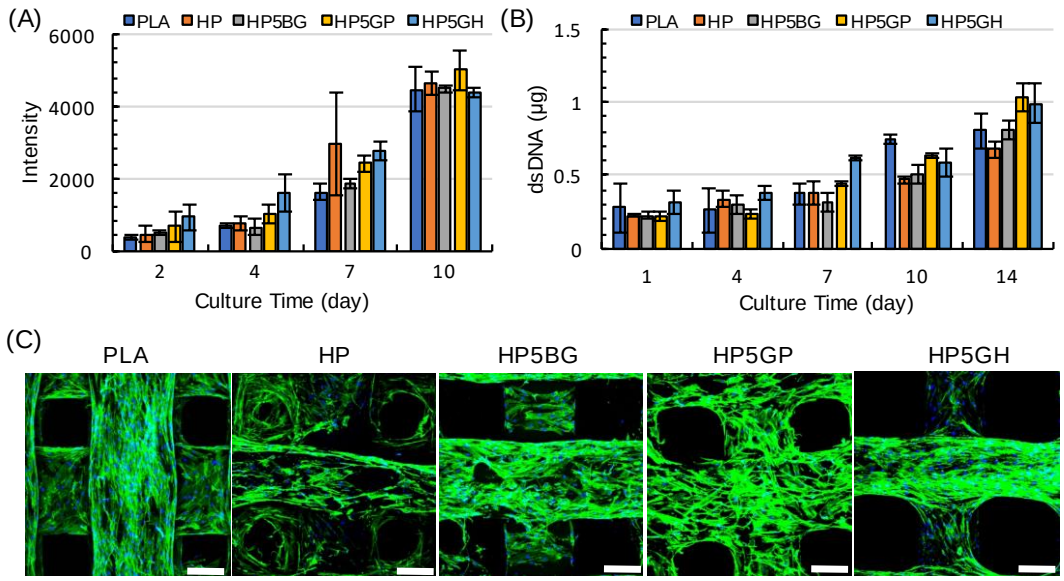

Figure 4.9 (A) Average peak intensities from alamarBlue cell viability assay for hMSCs cultured on scaffolds. (B) Average dsDNA quantities found within each scaffold group. Error bars represent the standard deviation (n = 6 and 3 samples/group for A and B, respectively). (C) Scanning fluorescent confocal 3D reconstructions of F-actin (green) and DAPI (blue) stained hMSCs cultured on the scaffolds for 14 days. Scale bars are 200 µm.

To utilize our functionalizable polymeric biomaterial ink platform, we studied the effect of heparin-tethered BMP-2 on osteogenic differentiation of hMSCs in osteogenic induction media up to 21 days. For this purpose, we printed scaffolds from HP5GP and functionalized them with az-Heparin ((+)Hep). One set of the (+)Hep group was then tethered with BMP-2 ((+)Hep-BMP2). Unfunctionalized HP5GP was used as a negative control. In addition, we included a positive control group where soluble BMP-2 ((+)sBMP2) is introduced into the media during media changes. Cells were stained for OC **(Figure 4.10A)** and ALP **(Figure 4.10B)** as markers of osteogenic differentiation. Alizarin Red (AR) staining was also used to qualitatively and quantitatively determine calcium deposition. When the cells were quantified at day 14, 85±3% and 80±4% of the cells stained positive for OC for (+)Hep-BMP2 and (+)sBMP2, respectively, which were significantly higher than (+)BMP2 (68±4%), (+)Hep (58±6%), and HP5GP (56±8%). At

day 21, (+)Hep-BMP2 and sBMP2 groups reached 93±4% and 100±5% as compared to (+)BMP2 (77±18%), (+)Hep (57±4%), and HP5GP (62±4%). Increased expression of OC suggested osteogenic differentiation was upregulated when HP5GP was functionalized with Heparin-BMP2 **(Figure 4.10C)**. The (+)Hep-BMP2 group also showed significantly higher ALP positive cells (57±3%) as compared to other groups at day 14 **(Figure 4.10D)**. When calcium deposition was characterized using AR staining, AR concentration increased significantly from ~0.1 to 0.5 mM for 14- and 21-day culture respectively, yet the sample groups did not show any significant differences **(Figure 4.10E)**. A longer culture period may be required to see significant changes.

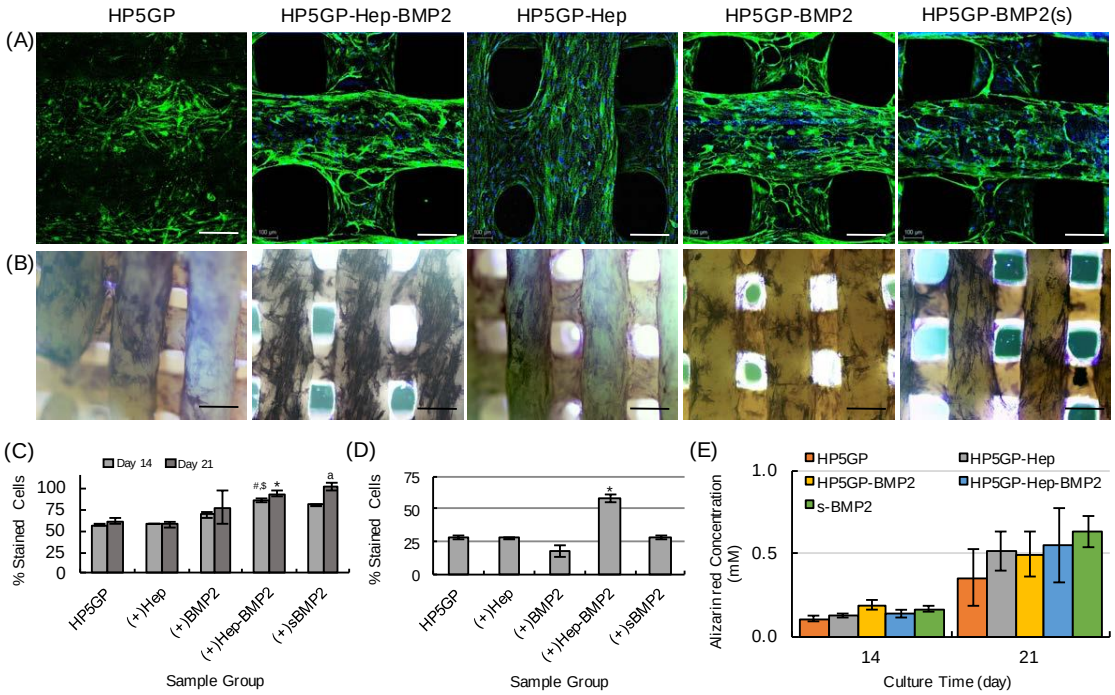

Figure 4.10 (A) Confocal images of hMSCs cultured on 3D printed scaffolds for 14 days in osteogenic differentiation media, and immunostained for human osteocalcin (OC) (green). Cell nuclei are stained with DAPI (blue). (B) Brightfield images of hMSCs stained for alkaline phosphatase (ALP, dark blue/purple) after 14 days of culture in osteogenic media. (C) Percentage of cells stained positive for OC corresponding to (A). For Day 14, $^{\#}p<0.2$ for Hep-BMP2 as compared to HP5GP and (+)Hep, $^{\#}p<0.5$ for Hep-BMP2 as compared to (+)BMP2. For Day 21, $p<0.02$ sBMP2 group as compared to HP5GP, (+)Hep, and (+)BMP2, and $*p<0.4$ for (+)Hep-BMP2 as compared to HP5GP and (+)Hep. (D) Percentage of cells stained positive for ALP corresponding to (B). $*p<0.001$ for (+)Hep-BMP2 as compared to other sample groups (n=3). (E) Alizarin Red (AR) staining quantification results using fluorometric analysis depicting AR concentration (mM) for each scaffold after 14 and 21 days of culture in osteogenic induction media.

4.4 Conclusions

We used a bottom-up synthetic design approach to develop novel 3D printable polymeric biomaterials for extrusion-based printing from biodegradable stiff polymers with tunable functionalizability. The polymer designs were based on the hydrolytically degradable monomer HTy, which is synthesized from two naturally occurring olive oil components (Tyrosol and 2-(4-hydroxyphenyl)acetic acid). Despite the presence of phenyl rings, p(HTy) was generally amorphous and not printable using commercially available 3D printers.

Introducing PDA into the synthetic design resulted in the HP copolymer, which showed crystalline behaviour due to enhanced π-π stacking interactions. The thermal processing properties of HP were almost identical to PLA, the gold standard for extrusion-based printing for biomedical applications. Functionalizability was achieved by incorporating glutamic acid derivatives (GR) into the synthetic design and generating copolymers of HTy, PDA, and GR. Our results showed that 5 mole% of GR addition did not significantly alter thermal properties, stiffness, and printability of these polymers. In this study, we particularly focused on functionalizable polymers enabling click-based conjugation chemistry via alkyne (HP5GP) or alkene (HP5GH) functionality. We successfully demonstrated the reactivity of these functional groups in bulk (using polymer solutions) and on the surface (using polymer films). 3D scaffolds fabricated from these polymers showed uniform strut distribution within the scaffolds, with strut resolution identical to that of PLA. When cultured on these scaffolds, hMSCs were highly viable, and uniformly attached and spread on the struts. To further demonstrate the utility of the functionalizable polymers, we studied the osteogenic differentiation of hMSCs on HP5GP scaffolds functionalized with az-Heparin and BMP-2 ((+)Hep-BMP2). Our results showed a significantly higher fraction of the hMSCs stained positive for ALP and OC, which are osteogenic markers for stem cells.

CHAPTER 5

3D PRINTING WAVY SCAFFOLDS FOR ENHANCED MSC OSTEOGENESIS

This chapter has been adapted from the publication:
S. Ji, M. Guvendiren, 3D Printed Wavy Scaffolds Enhance Mesenchymal Stem Cell Osteogenesis, Micromachines (Basel) 11(1) (2019).

5.1 Introduction

There is a growing interest in developing porous scaffolds for bone tissue engineering enabling temporary mechanical support for cells to attach, migrate and produce newly formed extracellular matrix to ultimately form a functional bone tissue [291-293]. Although bone has a robust regenerative ability, therapeutic interventions are required for large bone defects [294, 295]. Grafts (autografts, allografts, and xenografts) are commonly used in clinic to fill the defect site and to regenerate bone tissue [296, 297]. Porous scaffolds can be considered as an alternative to regenerate bone while mechanically supporting the defect site [298]. A wide range of techniques have been developed to fabricate porous bone scaffolds, such as gas foaming [299-301], solvent casting and particle/salt leaching [302-306], phase separation [307, 308], freeze drying [309, 310], and electrospinning [311-313]. However, the majority of these techniques fail to precisely control the 3D architecture of the scaffolds, including pore size and pore distribution, and also fail to develop reproducible scaffolds [291]. 3D printing is an additive manufacturing technique and enables fabrication of custom-designed and highly complex 3D scaffolds. 3D printing allows the use of patient's own medical images to design personalized scaffolds that are anatomically similar to the defect site. Thus, it has been widely utilized for fabricating custom-designed bone scaffolds [82, 145, 314-316]. A wide range of 3D printing techniques have been used to fabricate 3D bone scaffolds, such as fused deposition

modeling (FDM) [78, 317-319], direct ink writing (DIW) [320, 321], selective laser sintering and melting (SLS and SLM) [322], stereolithography (SLA) [323-325], continuous digital light processing (cDLP) [326, 327], and inkjet printing [328, 329]. These 3D printing technologies allow to utilize various printable materials [41] and designs [330]. Computational tools have also been utilized to optimize scaffold architecture to achieve enhanced permeability and mechanical properties [331-335].

Mesenchymal stem cells (MSCs) are regarded as a clinically relevant cell source for bone tissue engineering due to their ability to proliferate and migrate as well as their potential to differentiate into osteogenic lineage (bone) [336-339]. Stem cells are known to feel and respond to their microenvironment by regulating their function [174, 340-342]. Materials-based approaches have been developed to engineer extracellular matrix (ECM) mimetic microenvironments [15, 343, 344], including macro- and nano-scale topographical cues to control stem cell behavior [345, 346]. Topographical cues alone have been shown to control stem cell response, such as morphology, alignment, proliferation, migration, cytoskeletal organization, focal adhesion, nuclear deformation, and differentiation [346-348]. For example, human MSCs (hMSCs) are shown to produce bone mineral when cultured on substrates with the nanoscale disorder [349]. Nano-scale roughness is shown to enhance MSC osteogenesis even in the absence of induction media [350, 351]. This phenomenon is shown to be due to clustering of absorbed proteins on nano-topography, which promotes integrin-mediated focal adhesions enhancing cellular contractility and stem cell osteogenesis [350]. Micro-scale patterns confining stem cells within cell-adhesive regions were used to control stem cell shape or cellular spreading. For instance, McBeath et al. showed that hMSCs with spread morphology led to actin-myosin-generated

tension and promoted osteogenic differentiation [352]. Increasing cellular contractility, or cytoskeletal tension, by changing the shape of the multicellular sheets, Ruiz and Chen were able to enhance osteogenic differentiation of hMSCs [353]. Mrksich and co-workers showed that stem cells residing on curved surfaces became highly contractile and differentiated to osteogenic lineage [354]. Lineage commitment of hMSCs on hydrogel wrinkling patterns was determined by the pattern morphology, such that hMSCs on lamellar patterns formed spread morphology with a high cell aspect ratio (>4) differentiated into osteogenic progenitors [355]. When porous 3D scaffolds are considered, pore architecture, surface topography and interconnectivity are shown to control osteogenic differentiation of human mesenchymal progenitor cells [356]. Simon and co-workers fabricated 2D films and 3D porous scaffolds with different techniques (gas foaming, salt leaching, phase separation, electrospinning, 3D printing, and spin coating) to examine the seeded hMSCs osteogenesis, which indicated that the scaffolds could be optimized to control the cell morphology to direct differentiation [357]. Recently, DIW was used to create 3D scaffolds with distinct architectures composed of square (SQR), hexagonal (HEX), or octagonal (OCT) patterns [358]. Human MSCs were reported to exhibit higher cell aspect ratio and mean cell area on OCT scaffolds as compared to SQR and HEX scaffolds, and hence, showed significantly enhanced osteogenic differentiation. Although, the effect of curvature is well documented in 2D, it has not yet been studied systematically in 3D.

In this work, we used 3D printing to fabricate wavy poly(caprolactone) (PCL) scaffolds to investigate the effect of curvature on hMSC osteogenesis. A sinusoidal waveform was used to create wavy scaffolds. The wavelength and amplitude of the

sinusoid were systematically varied to design five distinct wavy scaffolds. Orthogonal scaffold with straight struts was used as a control. First, we investigated the effects of scaffold architecture on stem cell growth, including cell attachment, proliferation, and shape (spreading). Then, we studied the osteogenic differentiation of hMSCs on wavy scaffolds as compared to commonly used orthogonal architecture. The main hypothesis behind this study is that the wavy scaffolds can direct a more elongated and stretched stem cell morphology resulting in highly organized cytoskeletal arrangement with high contractility. This could lead to an increased osteogenesis, the degree of which can be controlled by the degree of the curvature or waviness.

5.2 Materials and Methods

5.2.1 Scaffold Design

Autodesk® Fusion 360™ (Autodesk Inc., San Rafael, CA, USA) was used to design the 3D models. The basic 3D model was designed as a cylinder with a diameter of 15 mm and a height of 1 mm. The 3D model (.stl file) was then loaded into Perfactory RP for slicing, with a layer height equal to 0.25 mm. The sliced file (.bpl file) was loaded into Visual Machine, and the infill patterns were selected. A linear pattern was selected for the orthogonal scaffolds (i.e., the control group), and a sinusoidal waveform was selected for the wavy scaffolds (**Figure 5.1**). For wavy scaffolds, the amplitude and the wavelength of the sinusoid were varied systematically to develop 5 distinct scaffold designs (**Table 5.1**).

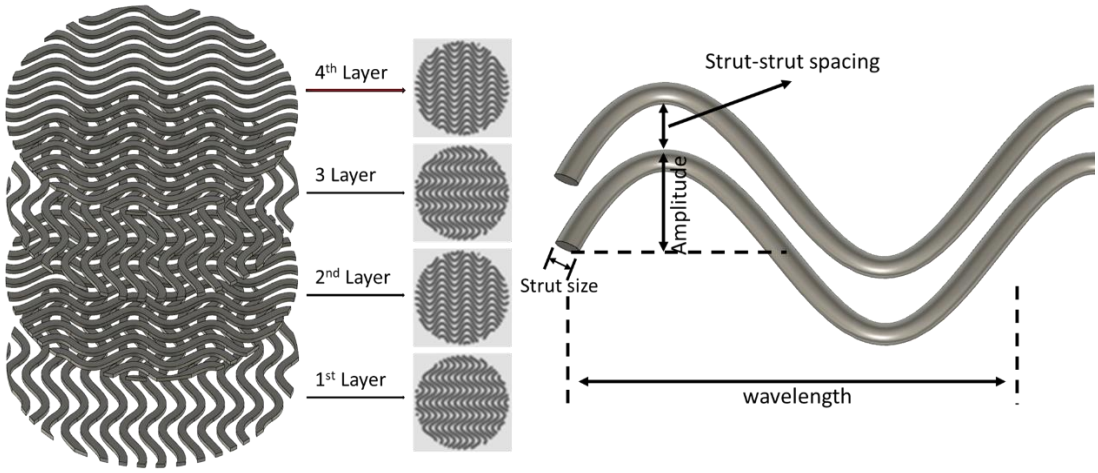

Figure 5.1 Wavy scaffold design containing four layers (left) and schematic showing the strut design for wavy scaffolds (right).

Table 5.1 Design and Printing Parameters for the Scaffolds

Parameter	Orthogonal	A0.5W2	A0.5W3	A0.5W4	A0.75W4	A1W4
Amplitude (mm)	-	0.5	0.5	0.5	0.75	1
Wavelength (mm)	-	2	3	4	4	4
Strut Diameter (μm)	533±9	497±73	490±36	513±30	510±32	460±58
Strut Spacing [1] (μm)	395±6	277±59	350±53	396±72	308±120	336±103
Struts Per Layer	16	15	15	15	15	15
Temperature [2] (°C)	80	80	80	80	80	80
Print Pressure (bar)	7	7	7	7	7	7
Print Speed (mm/s)	4	4	6	5	5	5
E [3] (MPa)	12.4±0.3	10.5±0.5	11.5±0.2	9.5±0.2	10.7±0.2	11.3±0.5
Porosity [4] (%)	56.3±0.7	56.5±1.2	55.9±0.3	61.7±0.9	57.6±0.5	57.2±3.1

[1]Strut-to-strut distance. [2] Print temperature. [3] Young's modulus from compression tests. [4] Micro-CT results.

5.2.2 3D Printing of Scaffolds

3D Bioplotter (EnvisionTEC) was used to print the scaffolds using PCL pellets (MW = 55 kDa, Polysciences Inc). The print temperature and pressure were set to 80 ℃ and 700 kPa (7 bar), whereas the print speed was varied from 4 to 6 mm/s for each design to achieve (see **Table 5.1** for actual values for each design).

5.2.3 Characterization of the Scaffolds

3D printed scaffolds were imaged by using a scanning electron microscope (SEM, JSM-7900F, JEOL) and a micro-computed tomography scanner (micro-CT, SkyScan 1275, Bruker). SEM images were used to measure the strut size and the strut-to-strut distance. Micro-CT was used to measure the porosity of the scaffolds. Compression tests were performed on 3D printed scaffolds using an Instron model 3343 with a 1000 N load cell and a 0.5 mm/min displacement rate. Three samples for each scaffold group were tested.

5.2.4 Preparation of the Scaffolds for Cell Culture

Scaffolds were sterilized by immersing them in 75% ethanol for 30 minutes, followed by 1-hour UV exposure (by a germicidal lamp) for each side of the scaffold. Scaffolds were then incubated in 20 μg/mL fibronectin solution in 300 μL (bovine fibronectin plasma, Invitrogen) overnight to enhance cell attachment. Fibronectin solution was removed, and scaffolds were washed with Dulbecco's Phosphate-Buffered Saline (DPBS, Gibco), moved into a new well, and kept in growth media prior to cell seeding.

5.2.5 Cell Culture and Reagents

Human mesenchymal stem cells (hMSCs, passage 4, Lonza) were cultured in growth media (α-MEM (minimum essential medium) supplemented with 10% fetal bovine serum (FBS, Gibco) and 1% penicillin-streptomycin (pen-strep, Gibco). Prior to seeding, each scaffold

was removed from growth media and placed in a single well in a non-treated 24-well plate. The hMSC suspension (133,000 cells/mL) were seeded from the top of the scaffolds (300 μL per scaffold, corresponding to approximately 5,000 cells/cm^2). Cells were incubated at 37 °C for 60 min to allow cell attachment. Scaffolds were then flipped, and the same amount of cell suspension was seeded from the top, followed by 60 min incubation at 37 °C. The scaffolds were then transferred to a new non-treated 24-well plate, and 1 mL of fresh growth media was added to each well. The scaffolds were incubated for 7 days in growth media. For osteogenic differentiation studies, growth media was replaced with osteogenic induction media (hMSC osteogenic differentiation medium BulletKitTM, Lonza) at Day 7, and cells were cultured for an additional 14 days. The media was refreshed every 3 days in cell culture studies.

5.2.6 Cell Culture and Characterization

For stem cell growth studies, alamarBlue assay (alamarBlue™ Cell Viability Reagent, Invitrogen) and PicoGreen assay (Quant-iT™ PicoGreen™ dsDNA Assay Kit, Invitrogen) was used to evaluate the cell proliferation at day 1, 4, and 7, according to manufacturer's protocol. Tecan plate reader (Infinite M200 Pro, Tecan) was used to complete the assays for these studies. To visualize the attached cells on the scaffolds, cells were washed with DPBS (3X), fixed with 4% formaldehyde for 15 min followed by DPBS wash (3X), and permeabilization in 0.25% Triton-X DPBS solution for 1 hour. Cells were stained for F-actin using rhodamine phalloidin (1:40 in DPBS, Invitrogen). Cell nuclei were stained with 4′,6-diamidino-2-phenylindole (DAPI, 1: 2000 in DPBS, Sigma). At day 7, cells were immunostained for vinculin using anti-vinculin−FITC antibody (1:50, mouse monoclonal, Sigma). For this purpose, cells were incubated in 10% goat serum (in DPBS) for 30 min,

washed with staining solution (3X, 3% bovine serum albumin + 0.1% Tween-20 + 0.25% Triton-X), and incubated in vinculin antibody in staining solution overnight at 4 °C. Cells were imaged by using a confocal and multiphoton microscopy (TCS SP8 MP, Leica).

For differentiation studies, calcium deposition was evaluated AT DAY 21 by using alizarin red staining kit (AR, Sigma). After the staining was completed, cells were washed with DPBS (3X), and incubated in 10% cetylpyridinium chloride (Sigma) in sodium phosphate buffer (10 mM, pH 7, Sigma) to remove the stain. This solution was then used to quantify calcium content by using a Tecan plate reader (scanned at 405 nm). Alkaline phosphatase activity was studied with QuantiChrom^{TM} Alkaline Phosphatase Assay Kit (ALP assay Kit, BioAssay Systems). Cells cultured within the scaffolds were first lysed with 0.2% Triton-X followed by 3 freeze-thaw circles. The lysate was then reacted with p-Nitrophenyl phosphate working solution and scanned at 405 nm using a plate reader (Infinite M200 Pro, Tecan). For osteocalcin (OC) staining, cells were fixed at Day 14 and Day 21. Cells were incubated in 10% goat serum (in DPBS) for 30 min, washed with staining solution (3X, 3% bovine serum albumin + 0.1% Tween-20 + 0.25% Triton-X), and incubated with the OC primary antibody (1: 200, monoclonal mouse, Invitrogen) in the staining solution overnight at 4 °C. After removing the antibody-containing staining solution and washing the samples with fresh staining solution, cells were incubated in Alexa Fluor 488 rabbit anti-mouse secondary antibody (1: 100, Invitrogen) in staining solution for 2 hours. Samples were then stained with phalloidin (rhodamine phalloidin, Invitrogen) and DAPI to visualize F-actin and cell nuclei, respectively. Cells were imaged by using a confocal and multiphoton microscopy (TCS SP8 MP, Leica). All of the collected images were processed using ImageJ for further analysis.

5.2.7 Statistics

The data were analyzed using Origin 2016 software. Data were presented as mean ± standard deviation. One-way ANOVA with Tukey's HSD post hoc test of means was used to make comparisons between sample groups ($n \geq 3$ samples per group unless otherwise specified).

5.3 Results

5.3.1 3D Printing of PCL Scaffolds

PCL scaffolds with 6 distinct designs, including one linear design (orthogonal), and 5 wavy designs in the form of sinusoidal wave with varying amplitude (A) and wavelength (W) (A0.5W2, A0.5W3, A0.5W4, A0.75W4, and A1W4, where numbers denote for the actual values of A and W in mm) are printed (**Table 5.1**). **Figure 5.2** shows the pictures, micro-CT images, and SEM images of the scaffolds. SEM images were used to measure the printed strut width and spacing between struts for each design, and results were summarized in **Table 5.1** Briefly, the average strut width was within the range of 460 ± 58 to 533 ± 9 μm, and the spacing between struts (strut-to-strut distance) was within the range of 277 ± 59 to 395 ± 6 μm.

5.3.2 Mechanical Tests

Compression tests were performed on each sample group, and the results are summarized in **Table 5.1** and **Figure 5.3**. The compressive modulus (Young's modulus, *E*) of all the designs were in the range of 9.5-12.4 MPa (**Table 5.1**). *E* (9.5 MPa) for the A0.5W4 design (with the highest porosity, ~62%) was significantly lower than the rest of the sample groups. The orthogonal design (*E* = 12.4 MPa and porosity = ~56%) showed significantly higher

E as compared to A0.5W2 (E = 10.5 MPa and porosity = ~56%), A0.5W4, and A1W4 (E = 11.3 MPa and porosity = ~57%).

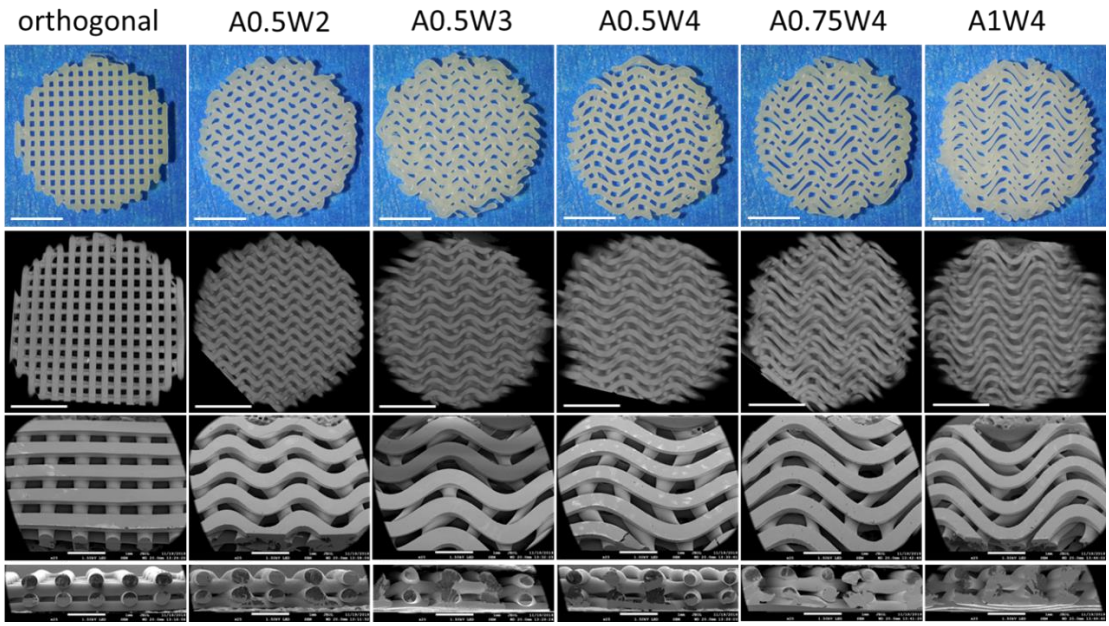

Figure 5.2 Images of the scaffolds. From the top to bottom row, images correspond to pictures (top view), micro-computed tomography (micro-CT) images (top view), scanning electron microscope (SEM) images, and SEM cross-section images. Scale bars are 500 μm for pictures and micro-CT images and 1 mm for SEM images.

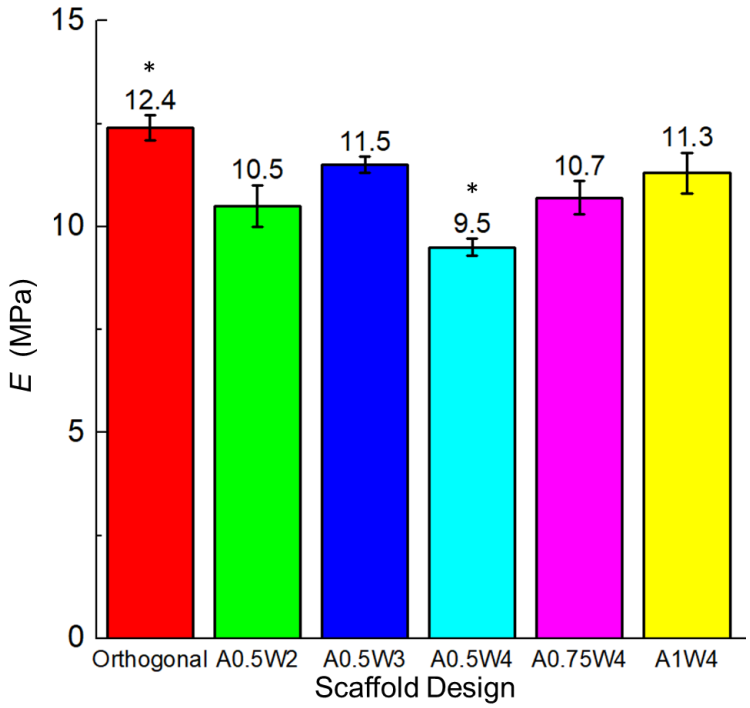

Figure 5.3 Young's modulus (*E*) values of the scaffolds for each scaffold design. * $p < 0.005$ for orthogonal vs. A05W2, A0.5W4, and A1W4; and for A0.5W4 vs. all sample groups.

5.3.3 Growth Study

The hMSC growth studies were performed by culturing cells in growth media for up to 7 days in growth media. The results for AlamarBlue assay and PicoGreen assay are shown in **Figure 5.4**. The AlamarBlue assay results showed that the measured mean intensities increased from Day 1 to Day 7, which indicated an increased metabolic activity with culture time. There was an exception for A1W4, which showed a drop from Day 4 to Day 7. At Day 7, no significant difference was observed between the test groups. For the PicoGreen assay, a similar trend was observed as the mean value of λ-DNA ascended from Day 1 to Day 7. At Day 7, there was no difference between the test groups. The multiphoton confocal images of the stem cells (F-actin in green and cell nuclei in blue) cultured on the 3D printed scaffolds for 7 days are given in **Figure 5.5**. F-actin

filaments were aligned with the printed struts that form the substrates, and this alignment was more pronounced in the curved regions in wavy scaffolds.

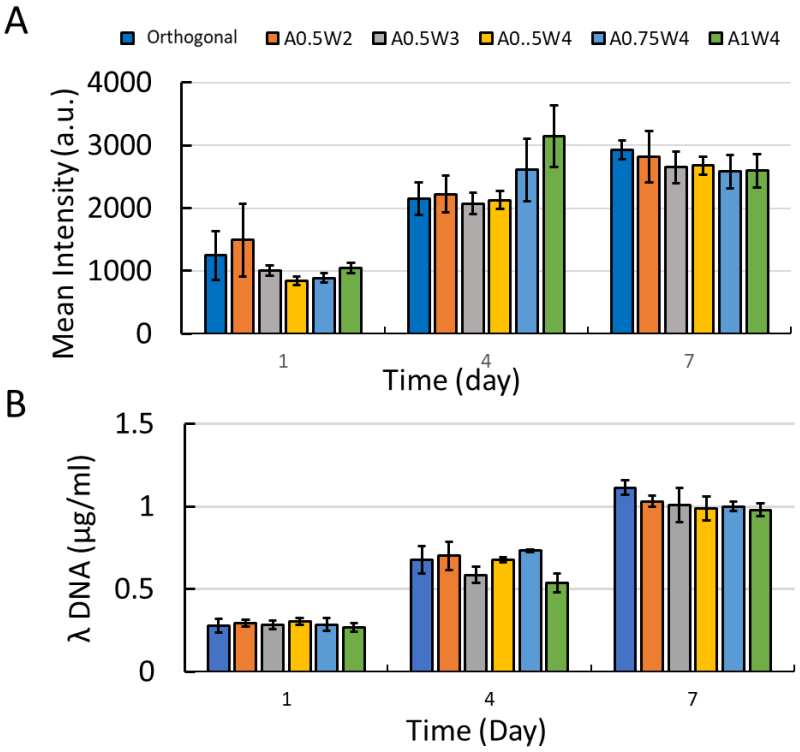

Figure 5.4 (A) AlamarBlue Assay (n=6); (B) PicoGreen Assay (n=3), *p<0.005

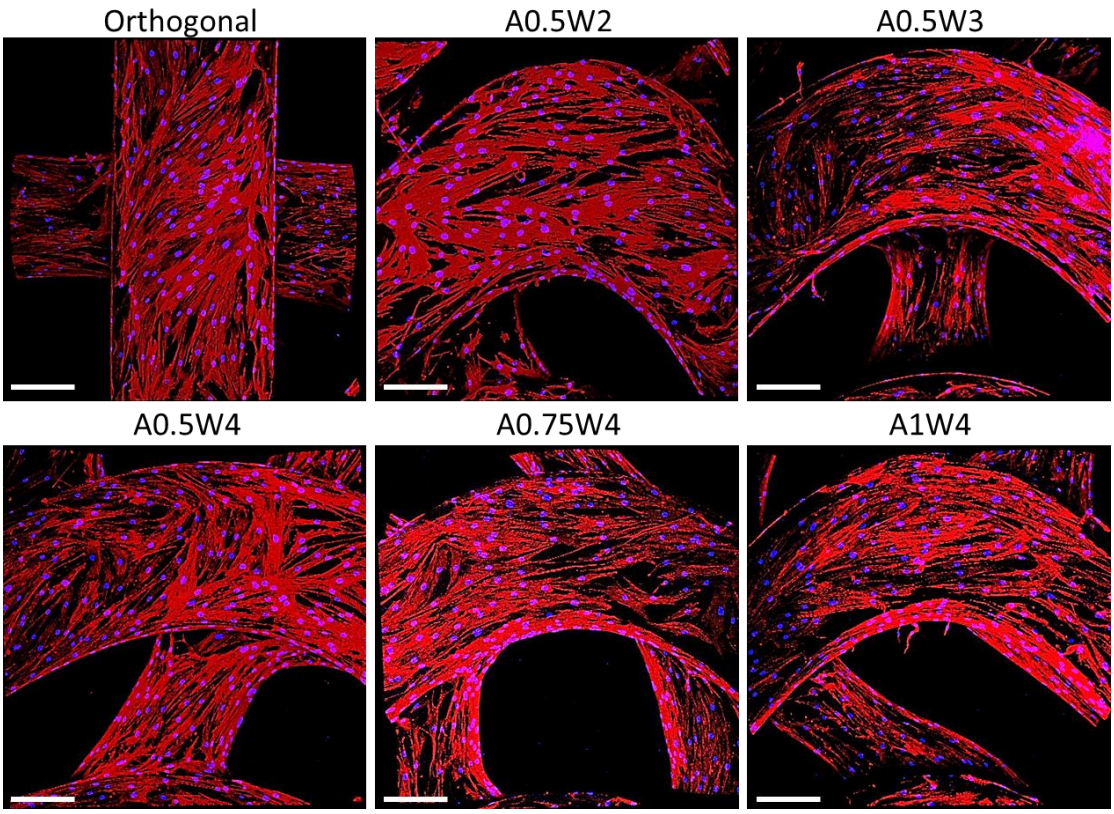

Figure 5.5 Multiphoton confocal images of the human mesenchymal stem cells (hMSCs) cultured on the scaffolds for seven days. Cells were stained for F-actin (red) and nuclei (blue). Scale bars are 200 μm.

5.3.4 Differentiation Study

Osteogenic differentiation of hMSCs cultured on the 3D printed scaffolds was studied for up to 21 days. **Figure 5.6** shows the results from AR staining and assay. The scaffolds with wavy designs showed more staining (**Figure 5.6A**) and higher values of mean calcium deposition (**Figure 5.6B**). The value of the mean calcium deposition in wavy groups was in the range of 2.5 to 6 times higher than that of the orthogonal group. Specifically, the average calcium deposition was equal to 9.33 ± 0.98 mM for A0.75W4, 8.14 ± 2.86 mM for A0.5W2, 7.60 ± 1.65 mM for A1W4, 6.12 ± 3.07 mM for A0.5W4, 3.96 ± 2.06 mM for A0.5W3, and 1.53 ± 0.10 mM for orthogonal scaffolds, in descending order. ALP

activity assay results, at culture Days 14 and 21, are given in Figure 7. Our results showed an increase in ALP activity for all sample groups from Day 14 to Day 21, and the ALP activity of the wavy scaffolds was higher than that of the orthogonal group at both Day 14 and Day 21 (**Figure 5.7**). At Day 14, A0.5W3 (13.16 ± 3.17 a.u.) was significantly higher than the orthogonal group (5.96 ± 1.58 a.u.). At Day 21, A0.5W2 (46.83 ± 7.90 a.u.) and A0.5W3 (45.51 ± 4.20 a.u.) were much higher than that of the orthogonal group (32.31 ± 0.89 a.u.). Representative fluorescent images showing vinculin staining at Day 7 are shown in **Figure 5.8**. We observed more pronounced vinculin fibers that were aligned with the wavy struts for wavy scaffolds as compared to diffused and randomly oriented vinculin for the orthogonal scaffold. **Figure 5.9** shows the representative confocal images of the hMSCs cultured on 3D printed scaffolds, in which cells were stained for osteocalcin (OC, green), F-actin (red), and nuclei (blue) at Culture Day 14 and 21. Osteocalcin staining was more pronounced on curved struts as compared to linear struts.

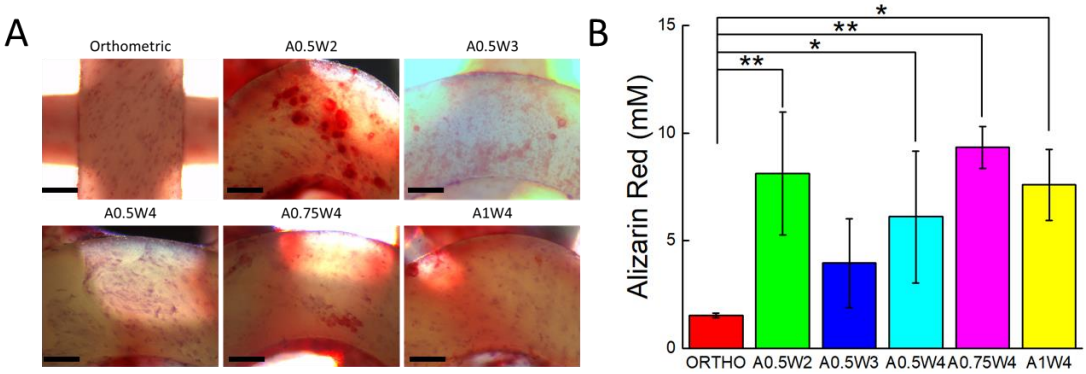

Figure 5.6 (A) Optical microscopy images of the hMSCs stained for alizarin red (red) after culture in osteogenic induction media for 21 days. Scale are 200 μm. (B) Alizarin red concentration indicating calcium deposition at Day 21. (* $p < 0.15$, ** $p < 0.05$, for $n = 3$).

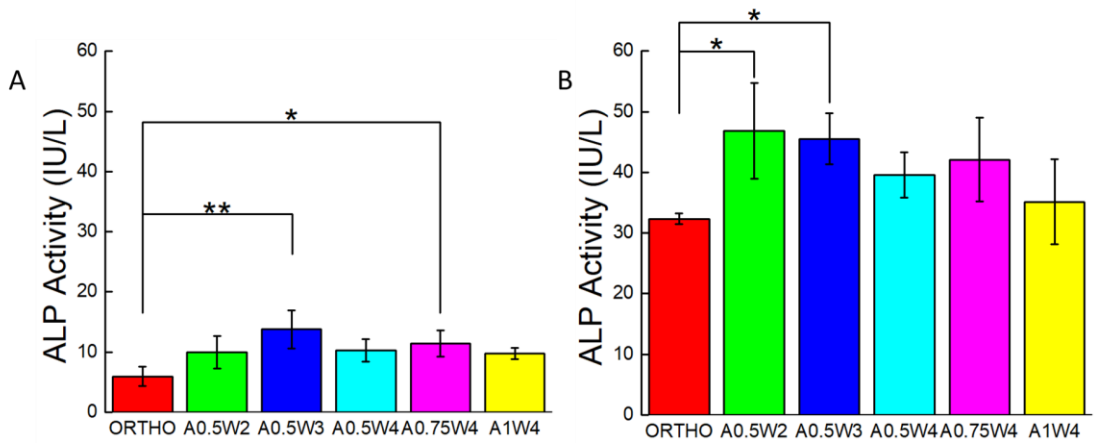

Figure 5.7 ALP activity assay results for: (A) Day 14 and (B) Day 21 (* $p < 0.15$, ** $p < 0.05$, for $n = 3$).

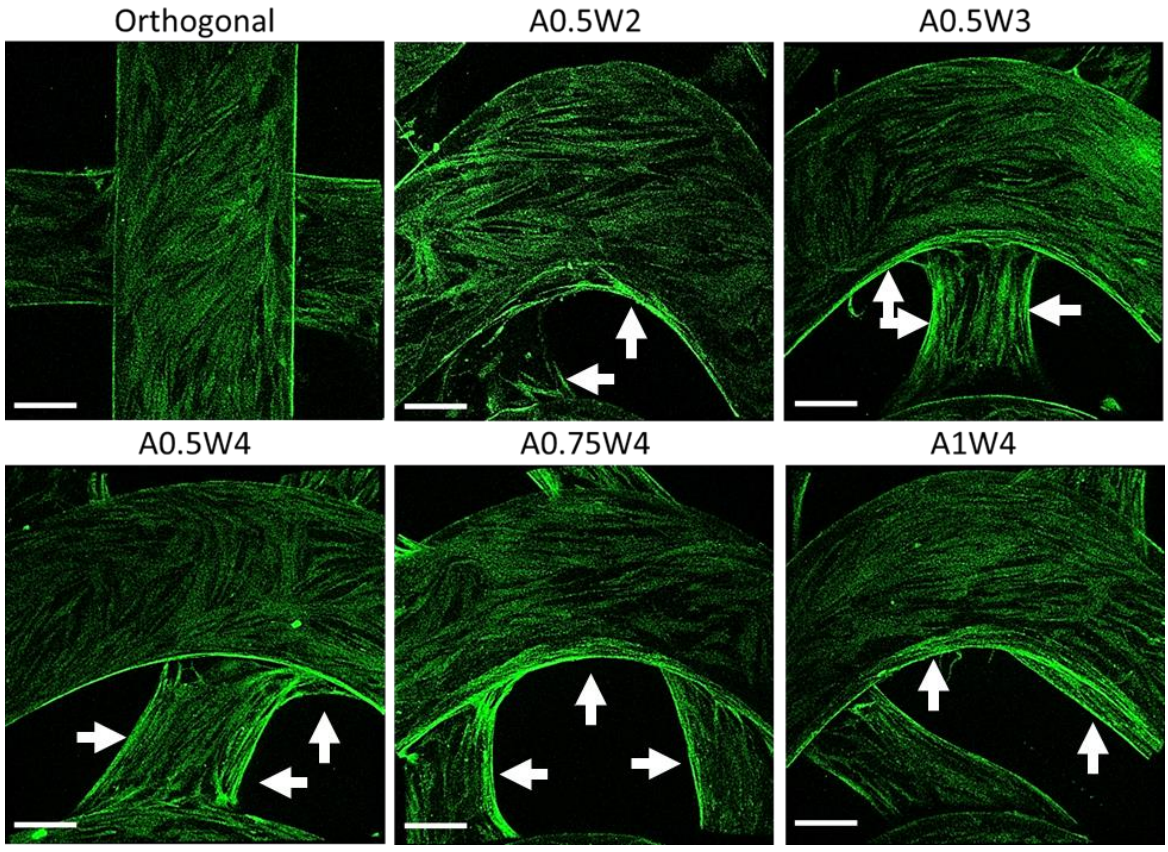

Figure 5.8 Multiphoton confocal images of hMSCs that are stained for vinculin (green) at Day 7.

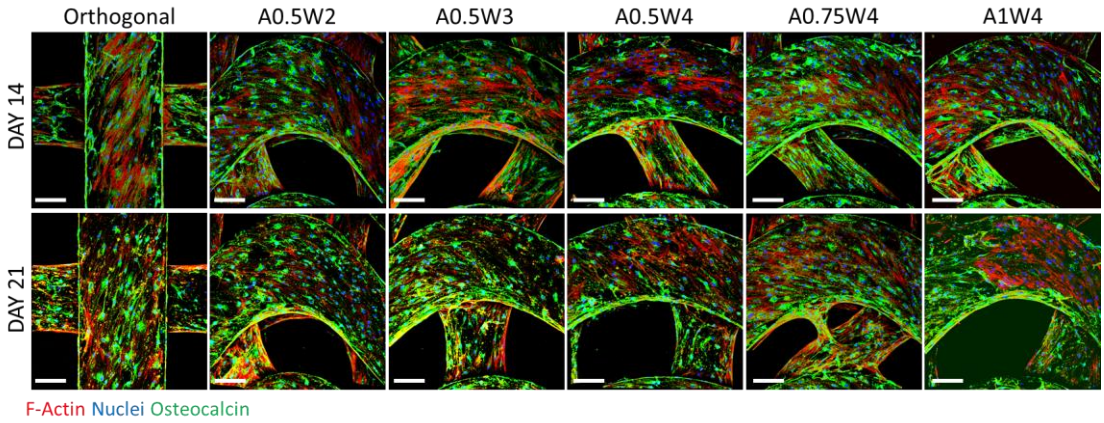

Figure 5.9 Multiphoton confocal images for hMSCs that were cultured in osteogenic induction media for 14 (top row) and 21 days (bottom row). Cells were immunostained for osteocalcin (green) and stained for F-actin (red) and cell nuclei (blue). Scale bars are 200 μm

5.4 Discussion

In this study, we used extrusion based DIW printing technology to fabricate PCL scaffolds. DIW allowed us to 3D print scaffolds directly from PCL pellets, which were melted within and extruded from a steel syringe attached to the print head. PCL was selected as a model polymer as it is a "Generally Recognized As Safe" (GRAS) polymer by the U.S. Food and Drug Administration and widely used to 3D print tissue engineering scaffolds for both *in vitro* and in vivo studies [82, 322, 359] We used hMSCs as the main cell line due to their ability to proliferate, migrate, and differentiate into a wide range of tissue specific phenotypes including bone, cartilage, and muscle. Stem cells are known to feel and respond to their microenvironment (matrix stiffness, topography, and bioactivity) by regulating their behavior [15, 174]]. Here, we focused on the topography, or scaffold architecture. To investigate the effects of 3D scaffold architecture on stem cell osteogenesis, we constructed scaffolds using struts in sinusoidal waveforms, systematically varying the amplitude and the wavelength (**Figures 5.1** and **5.2**, **Table 5.1**). The sinusoidal waveform design created

highly curved strut surfaces forming 3D scaffolds with wavy patterns. Our motivation to create wavy scaffolds was based on previous studies, which clearly showed the importance of substrate curvature on stem cell osteogenesis [353, 354].

The minimum wavelength and amplitude achievable for a strut size around 500 μm were 2 mm and 0.5 mm (A0.5W2). While keeping the amplitude constant at 0.5 mm, the wavelength was increased to 3 mm (A0.5W3) and 4 mm (A0.5W4). For the 4 mm wavelength, the amplitude was increased to 0.75 mm (A0.75W4) and 1 mm (A1W4). These geometrical constraints allowed us to create scaffolds with an average strut-to-strut distance of approximately 350 μm (**Figure 5.2**, **Table 5.1**). Note that the effect of pore size in bone scaffolds has been well studied [305, 314, 360-365], and a minimum pore size of ~150 μm is usually required for cell migration and tissue ingrowth [247, 293, 366, 367]. We then investigated the effect of scaffold design on mechanical properties of the scaffolds (**Figure 5.3**). The compressive modulus (*E*) values were determined by the design, i.e., strut-to-strut contacts between layers, and the overall scaffold porosity. E values were significantly the highest for orthogonal scaffolds (12.5 MPa) mainly because these scaffolds inherently displayed more strut-to-strut contacts, considering that this design had 16 struts per layer, whereas all the wavy designs had 15 struts per layer. This design also had one of the lowest porosities with ~56%. When wavy scaffolds were compared, A0.5W4 showed the significantly highest porosity (~62%) corresponding to the significantly lowest E value of 9.5 MPa followed by A0.75W4 (58%, 10.7 MPa), A1W4 (57% 11.3MPa), and A0.5W3 (56%, 11.5 MPa). A0.5W2 (56%, 10.5 MPa) was an exception and did not follow the trend. This was due to reduced strut-to-strut contacts due to the design (**Figure 5.2**). Although the overall scaffold modulus determines the mechanical support level that a

scaffold can provide when implanted, it did not affect the stem cell behavior in our study. This is because the stem cells feel the mechanics of the individual struts (which was uniform for all scaffold groups) that they reside on when seeded on to the scaffolds [358].

First, the growth study was conducted to determine the attachment and proliferation of the hMSCs cultured on our scaffolds. The metabolic activities of the cells were not significantly different from each other at each culture day, but increased significantly with culture day, reaching a maximum at Day 7 (**Figure 5.4A**). The same trend was observed when the DNA was quantified (**Figure 4B**). Note that this trend was not true for the A1W4 and A0.75W4 sample groups, for which the metabolic activity reached a maximum at Day 4 and did not change significantly at Day 7. Yet, the DNA count did not show this unexpected trend for these two sample groups, which represented the cell proliferation more accurately. F-actin staining at Day 7 confirmed that cells attached onto the struts and formed confluent layers at Day 7, taking the shape of the struts. Cells on wavy scaffolds were highly elongated, especially on the curved edges with well-defined F-actin filaments aligned with the scaffold curvature as compared to much bulkier cells on orthogonal scaffolds (**Figure 5.5**). In addition, stem cells on wavy scaffolds showed mature vinculin (focal adhesion marker) patches as compared to diffused vinculin staining of cells on orthogonal scaffolds at Day 7 (**Figure 5.8**). Focal adhesion is a vital step in osteogenesis [368] in which vinculin directs the interaction between talin and actin to direct the focal adhesion process [369]. We investigated if these significant changes in stem cell morphology, F-actin expression, and focal adhesion on wavy scaffolds as compare to orthogonal scaffolds correlated with stem cell osteogenesis on wavy scaffolds. It was also noted that the curvature had a direct effect on cell proliferation, and studies have shown

that curvature induced contractility enhances proliferation and cell growth [370-372]. In our study, we did not observe a significant difference in proliferation between sample groups. This was not contradictory to the literature as each of our wavy scaffolds displayed both concave and convex curvature, and the overall cellular behaviour was collective rather than distinct for each type of curvature.

The differentiation studies were conducted after the cells reached a confluent state at Day 7, as shown by the growth studies (**Figures 4** and **5**). At Day 7, the growth media was replaced with osteogenic induction media, and cells were cultured for 14 additional days in induction media, a total of 21 days in culture. To assess the osteogenic differentiation of hMSCs, we quantified calcium deposition and ALP activity and performed immunostaining for osteocalcin. The AR assay was used to probe the deposition of calcium. Optical microscope images revealed that wavy scaffolds showed more stained regions than the orthogonal group. When quantified, all the wavy scaffolds showed higher calcium deposition than the orthogonal group, and in particular, two groups (A0.5W2 and A0.75W4) showed significantly higher calcium deposition (**Figure 5.6**). These results indicated that the overall contribution of the curvature on these two scaffolds on cellular contractility induced calcium deposition was the highest. ALP is a well-known biological marker for stem cell osteogenesis [373]. ALP activity increased significantly for all of the scaffold groups from Day 14 to Day 21 (**Figure 5.7**). All the wavy groups showed higher ALP activity than the orthogonal group. However, the differences between wavy groups and the orthogonal group were not as significant as the results from the AR assay. This could be because the ALP expressed at earlier stages of the osteogenesis process. At Day 14, A0.5W3 showed significantly higher ALP activity ($p < 0.05$) when compared to the

orthogonal group. At Day 21, both A0.5W2 and A0.5W3 were substantially higher than the orthogonal group ($p < 0.15$). To supplement our quantitative differentiation assays, we performed OC immunostaining (**Figure 5.9**) as a marker for osteogenesis. Qualitatively, we observed increasing OC staining with culture day, and wavy scaffolds showed more OC staining, in particular in the curved regions of the scaffolds. The enhanced osteogenesis behaviour on wavy scaffolds could be explained as the effect of the curvature, which led to a highly aligned and stretched cellular morphology (**Figure 5.5**) with mature focal adhesions (**Figure 5.8**), leading to highly contractile cells promoting osteogenesis. We strongly believe that our results clearly showed the importance of scaffold architecture on hMSC osteogenesis and would help to develop novel scaffold architectures for bone tissue regeneration.

5.5 Conclusions

In this study, we developed 3D printed PCL scaffolds with wavy or linear patterns to investigate the effects of a wavy scaffold architecture on the osteogenic differentiation of hMSCs. When cultured in growth media, hMSCs attached and proliferated, forming confluent layers on the scaffolds within seven days. We found that hMSCs spread by taking the shape of the curved surfaces and exhibited elongated F-actin filaments and mature focal adhesion sites (vinculin staining). In contrast, hMSCs were bulkier in shape and showed dispersed vinculin staining on the orthogonal scaffold. We found that hMSCs showed significantly higher calcium deposition, higher ALP activity, and significantly pronounced osteocalcin staining when cultured on wavy scaffolds as compared to orthogonal scaffolds. These results are important in that they clearly showed the importance of scaffold

architecture on hMSC osteogenesis and may provide guidance on novel bone scaffold/graft design for pre-clinical and clinical applications.

CHAPTER 6

SUMMARY, CONCLUSIONS, AND FUTURE WORK

This dissertation introduced the development of a novel bioprinting approach for fabricating complex channels within cell-laden hydrogels, a novel bioink platform, and a novel UV-stimuli bioink platform, and a polyester-based functionalizable biomaterial ink platform for 3D printing of tissue engineering scaffolds. In addition, the effect of the scaffold architecture on stem cell differentiation was also investigated.

In Chapter 2, the reported approach is a complementary technique to existing approaches to fabricate user-defined and tunable channels and does not require rapid solid to gel transition of the support material (or shear-thinning behavior), which makes it more applicable for a wide range of commercially hydrogel systems. Since our approach does not require special chemistries, there are potentially a greater number of commercially available options for ink materials. Following this study, the approach could be utilized to fabricate microfluidic cell-laden hydrogel chips as *in vitro* models for drug screening and cell behavior studies.

In Chapter 3, the reported norbornene-functionalized bioink platforms, cCMC and NorCMC, have their advantages in cost-effectiveness, tunability, and cytocompatibility, broadening the bioink library of 3D bioprinting. However, the current bioink formulations have autogelation issues that limit the printable window, and it is difficult to print the bioinks as well-defined structures without support materials. To address these issues, we have found that the pH of the formulations can significantly postpone the autogelation point. To improve the printability, the in-situ-photocrosslink printing strategy [121] could be

applied to print cCMC and NorCMC. In addition, different crosslinkers are capable of adjusting the mechanical and biochemical properties of the bioinks, which indicates a great promise of the cCMC and NorCMC in cartilage tissue engineering.

In Chapter 4, the reported polyester-based ink platform, including HP5GH, HP5GP, and HP5BG, demonstrated great degradability, printability, and cytocompatibility. HP5GP and HP5GH were successfully functionalized, and HP5GP was selected to test the function of the ink, which was validated via the osteogenic differentiation study. This novel polymer platform with tunable functionalizability could be utilized for additive manufacturing of biodegradable devices and scaffolds with tailored mechanical and bioactive properties for a wide range of medical applications, including bone fixation devices and scaffolds for bone regeneration.

In Chapter 5, PCL scaffolds with wavy or linear architectures were printed, followed by an hMSC osteogenic differentiation study. The results showed hMSCs on wavy scaffolds had more calcium deposition, ALP activity, and osteocalcin deposition. Although the impact of the scaffold architecture on hMSC differentiation was clear, and we had proposed the curvature led to more aligned and stretched cellular morphology, the quantification of the impact of the scaffold architectures may be simulated with a proper model, which can further optimize the scaffold design for bone tissue engineering.

However, the presented studies have their limitations, and warrant future investigation. For the bioprinting approach for fabricating complex channels within cell-laden hydrogels, more characterizations for the HUVEC layer are yet to be performed. Permeability of the HUVEC layer is vital to the function of the vasculature. Also, immunostaining such as CD31 and VE-cadherin could be performed on the HUVEC layer

to verify cell phenotype and the cell-cell junction. Besides, the HUVEC layer cannot fully resemble the actual vessel structures, which have multicellular and hierarchical structures instead of a HUVEC monolayer. For the norbornene-modified CMC bioink platforms, one significant drawback is the print fidelity. Current ink formulations do not allow printing self-supportive cCMC/NorCMC without printing support materials. To address this issue, the in-situ crosslink strategy could be utilized as a potential solution [121]. As to the polyester-based ink platform with tunable properties, although the bioactivity was tunable, we did not directly evaluate the bioactivity. Due to our limited access to animal models, in vivo tests could have been performed to demonstrate the potency of the developed biomaterial ink. Moreover, thermal degradation should be considered and characterized, and the mechanical properties of the scaffolds could be tracked during the culture process. In the final chapter, to study the impact of scaffold architecture on hMSC osteogenesis, we performed multiple characterizations for osteogenesis. However, most of these were to probe the overall osteogenic expression of the cells on the scaffolds. This might be the reason for not to observe any significant difference between the different wavy scaffolds. More tests at a single cell level could potentially provide more detailed information to identify the optimal wavy pattern to enhance hMSC osteogenesis. In addition, the strut size (or the size of the wavy patterns) utilized in this study was much larger than that of a single cell due to limitations in 3D printing technology, which inherently limits our ability to create single-cell scale curvature.

APPENDIX A

SUPPLEMENTARY DATA OF CHAPTER 2

This appendix includes NMR data and line test data of Pluronic F-127

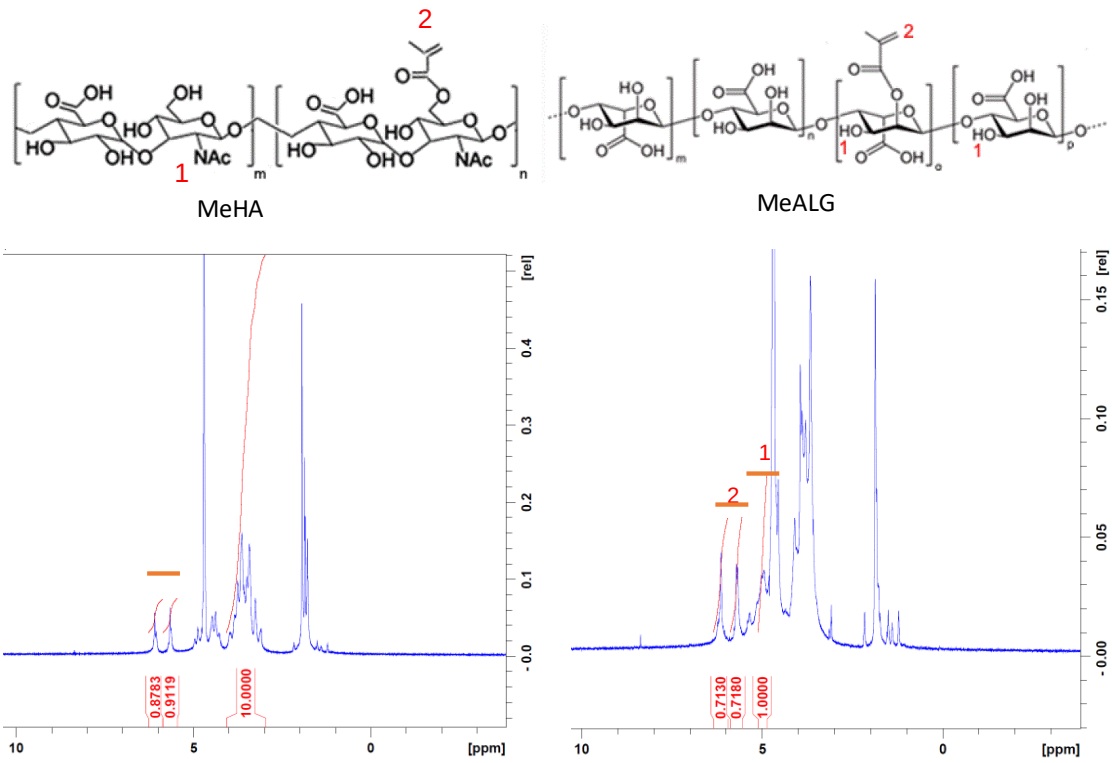

Figure A.1 ^{1}H NMR spectrum of methacrylated hyaluronic acid (MeHA) and methacrylated alginate (MeAlg). For MeHA, the functionalization was of ~90%, determined from the integration of the vinyl group (δ=5.8, 1 H and δ=6.25, 1 H) with respect to the HA backbone (δ=3.20-4.20, 10 H). For MeAlg, the functionalization was of ~72%, determined from integration of vinyl group (δ=5.8, 1H, and δ=6.25, 0.72 H) with respect to the hydroxyl group in alginate (δ=4.8-5.2 1H).

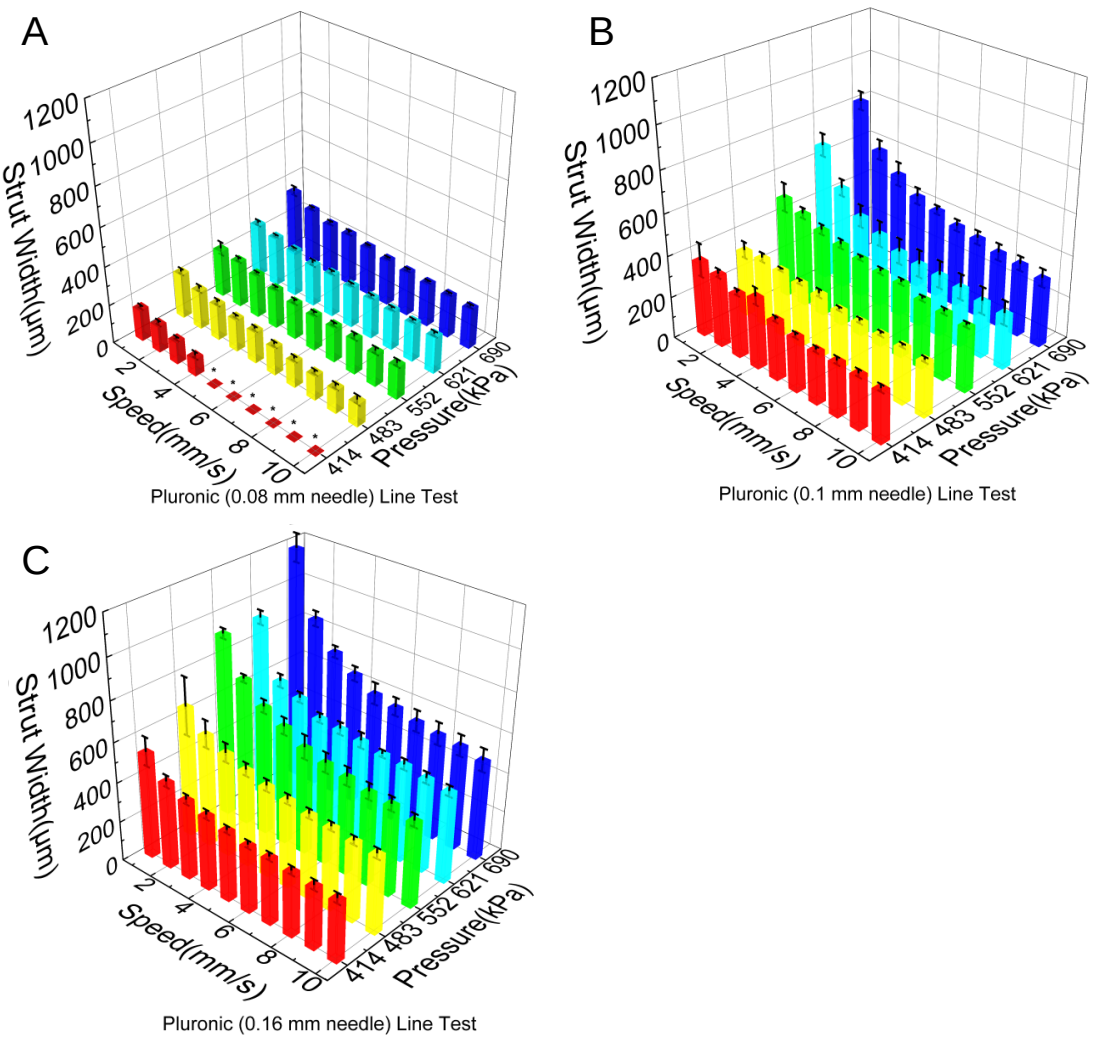

Figure A.2 Line test results showing the strut width plotted against print speed and print pressure for (A) 0.08 mm, (B) 0.10 mm, and (C) 0.16 mm needle from top to bottom, respectively.

APPENDIX B

SUPPLEMENTARY DATA OF CHAPTER 3

This appendix includes NMR data and rheological data of cCMC and NorCMC under UV.

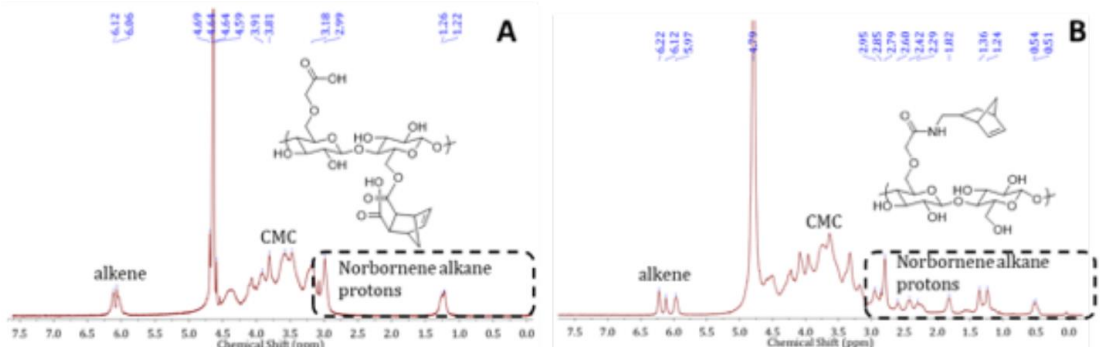

Figure B.1 ^{1}H NMR spectra of (A) cCMC and (B) NorCMC.

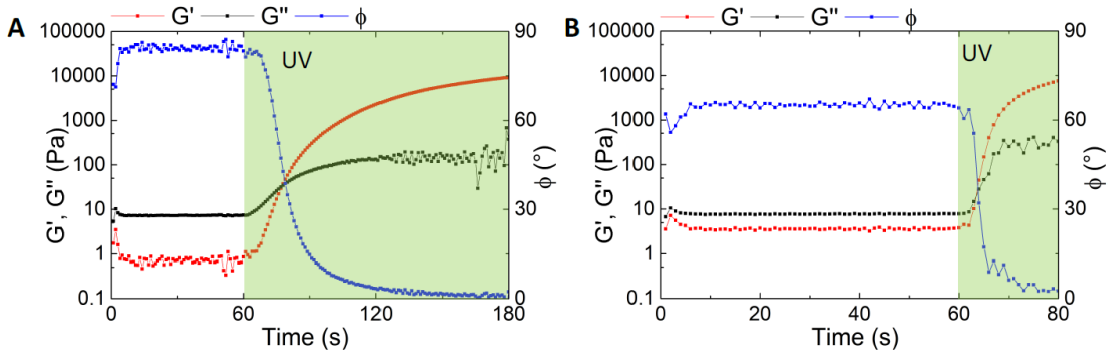

Figure B.2 Time sweep test of ink formulations under light exposure, (A) 10% NorCMC 1:2 and (B) cCMC 1:2. Green area denotes the UV exposure period.

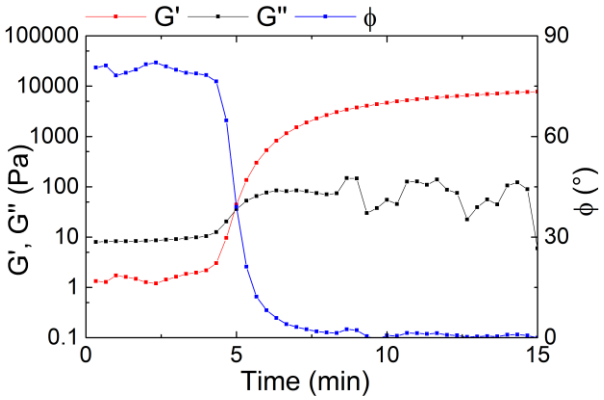

Figure B.3 Time sweep test of cCMC (1:2) without pH adjustment.

APPENDIX C

SUPPLEMENTARY DATA OF CHAPTER 4

C.1 Monomer Synthesis

C.1.1 Synthesis of 4-hydroxyphenethyl 2-(4-hydroxyphenyl)acetate (HTy)

A 2 L round bottom flask was attached to an overhead stirrer and a Dean-Stark apparatus with water-cooled condenser and a heating mantle was placed beneath the flask. 4-hydroxyphenylacetic acid (157.4 g, 1.03 mol), Tyrosol (142.9 g, 1.03 mol), phosphoric acid (5.07 g, 51.7 mmol), and 315 mL of toluene were added to the flask. The reaction mixture was stirred and heated at reflux until no more water was collected by azeotropic distillation. The reaction mixture was allowed to cool and phase separate and the upper layer was decanted leaving a thick syrup. The syrup was dissolved in 600 mL of ethyl acetate and washed twice with 150 mL of 5% sodium bicarbonate solution and twice with 150 mL of brine solution. The ethyl acetate solution was dried over magnesium sulfate and concentrated *in vacuo* to obtain a thick syrup. The syrup was concentrated *in vacuo* several times with cold dichloromethane to obtain a white powdered residue. The powder was recrystallized from a dichloromethane:hexane mixture, collected by vacuum filtration, and dried in a vacuum oven at 40 ˚C for 72 h. Yield: 223 g, 79%. Melting Point: 94 ˚C. ^{1}H NMR (500 MHz, DMSO-d_6, δ in ppm): 9.27 (s, 1H), 9.18 (s, 1H), 7.02 - 6.94 (m, 4H), 6.71 - 6.64 (m, 4H), 4.14 (t, J = 6.9 Hz, 2H), 3.48 (s, 2H), 2.74 (t, J = 6.9 Hz, 2H).

C.1.2 Synthesis of Dimethyl hex-5-enoylglutamate (Gluhexenamide dimethylester)

L-glutamic acid dimethyl ester hydrochloride (1.0 g, 4.7 mmol) was mixed with triethylamine (0.47 g, 4.7 mmol) in 10 mL of dichloromethane (DCM). Separately, 5-

hexenoic acid (0.59 g, 5.2 mmol), 1-ethyl-3-(3-dimethylaminopropyl)carbodiimide hydrochloride (EDCI) (0.99 g, 5.2 mmol), and hydroxybenzotriazole monohydrate (HOBt) (0.80 g, 5.2 mmol) were dissolved in 10 mL DCM. The two solutions were combined and stirred overnight. The solution was washed twice with 20 mL of 10% sodium bicarbonate solution, dried over magnesium sulfate, and concentrated *in vacuo* to obtain an oil that was used without further purification. Yield: 86 %. ^{1}H NMR (500 MHz, DMSO-d_6, δ in ppm): 8.18 (d, *J* = 7.5 Hz, 1H), 5.77 (ddt, *J* = 16.9, 10.2, 6.6 Hz, 1H), 5.03 - 4.90 (m, 2H), 4.23 (ddd, *J* = 9.2, 7.5, 5.3 Hz, 1H), 3.60 (s, 3H), 3.57 (s, 3H), 2.42 - 2.31 (m, 2H), 2.10 (t, *J* = 7.6 Hz, 2H), 2.02 - 1.90 (m, 3H), 1.79 (dddd, *J* = 13.8, 9.2, 7.9, 6.6 Hz, 1H), 1.55 (d, *J* = 7.5 Hz, 2H).

C.1.3 Synthesis of Hex-5-enoylglutamic acid (Gluhexenamide)

Dimethyl hex-5-enoylglutamate (1.1 g, 4.5 mmol) was combined with sodium hydroxide (0.5 g, 12.5 mmol) in a 3.5:1 tetrahydrofuran:water mixture (7 mL). The resulting solution was stirred overnight and concentrated *in vacuo.* The pH was lowered to ~3 by adding concentrated hydrochloric acid. This solution was extracted with 3 portions of 20 mL ethyl acetate. The ethyl acetate solution was dried over magnesium sulfate and concentrated *in vacuo*. 0.8 g of oily residue was obtained. Yield: 90%. ^{1}H NMR (400 MHz, DMSO-d_6, δ in ppm): 12.40 (s, 2H), 8.02 (d, *J* = 7.8 Hz, 1H), 5.77 (ddt, *J* = 16.9, 10.2, 6.6 Hz, 1H), 5.09 - 4.85 (m, 2H), 4.17 (ddd, *J* = 9.2, 7.9, 5.1 Hz, 1H), 2.28 - 2.20 (m, 2H), 2.14 - 2.07 (m, 2H), 2.03 - 1.87 (m, 3H), 1.79 - 1.66 (m, 1H), 1.61 - 1.49 (m, 2H). ESI-MS m/z: $[M-H]^-$ Calculated for $C_{11}H_{16}NO_5^-$ 242.10, found 242.09. ESI-MS: $[M+Na]^+$: Calculated for $C_{11}H_{17}NNaO_5$ 266.10, found 265.98.

C.1.4 Synthesis of Dimethyl pent-4-ynoylglutamate (Glupentynamide Dimethylester)

L-glutamic acid dimethyl ester hydrochloride (1.0 g, 4.7 mmol) was mixed with triethylamine (0.47 g, 4.7 mmol) in 10 mL DCM. Separately, 4-pentynoic acid (0.51 g, 5.2 mmol), EDCI (0.99 g, 5.2 mmol), and HOBt (0.80 g, 5.2 mmol) were dissolved in 10 mL DCM. The two solutions were combined and stirred overnight. The solution was washed twice with 20 mL of 10% sodium bicarbonate solution, dried over magnesium sulfate, and concentrated *in vacuo* to obtain an oil that was used without further purification. Yield: 93 %. ^{1}H NMR (400 MHz, DMSO-d_6, δ in ppm): 8.32 (d, J = 7.6 Hz, 1H), 4.28 (td, J = 8.4, 5.4 Hz, 1H), 3.66 - 3.53 (m, 6H), 2.74 (td, J = 2.1, 1.0 Hz, 1H), 2.43 - 2.24 (m, 6H), 1.98 (dtd, J = 13.3, 7.8, 5.3 Hz, 1H), 1.90 - 1.71 (m, 1H).

C.1.5 Synthesis of Pent-4-ynoylglutamic Acid (Glupentynamide)

Dimethyl pent-4-ynoylglutamate (1.1 g, 4.3 mmol) was combined with sodium hydroxide (0.5 g, 12.5 mmol) in a 3.5:1 tetrahydrofuran:water mixture (7 mL). The resulting solution was stirred overnight and concentrated *in vacuo.* The pH was lowered to ~3 by adding concentrated hydrochloric acid. This solution was extracted with 3 portions of 20 mL ethyl acetate. The ethyl acetate solution was dried over magnesium sulfate and concentrated *in vacuo* to obtain 0.64 g of solid powdered product. Yield: 66 %. Melting Point: 97 ˚C. ^{1}H NMR (400 MHz, DMSO-d_6, δ in ppm): 12.35 (s, 2H), 8.15 (d, J = 7.9 Hz, 1H), 4.20 (ddd, J = 9.2, 7.8, 5.0 Hz, 1H), 2.77 – 2.68 (m, 1H), 2.43 – 2.18 (m, 6H), 2.03 – 1.84 (m, 1H), 1.83 – 1.65 (m, 1H). ESI-MS m/z: $[M+Na]^+$ Calculated for $C_{10}H_{13}NNaO_5$ 250.07, found 250.02; $[M+H]^+$ Calculated for $C_{10}H_{14}NO_5$ 228.09, found 227.94.

C.2 Polymer Synthesis

C.2.1 General Synthesis of Polyesters

In a round bottom flask, 1 equivalent of diol (HTy), 0.97 combined equivalents of diacids, and 0.33 equivalents of 1,4-dimethylpyridinium p-toluenesulfonate (DPTS) were combined with DCM and magnetically stirred for 15 min. The stirring reaction mixture was cooled for 30 min in an ice bath and then 2.1 equivalents of N,N′-diisopropylcarbodiimide (DIC) were added. The stirring reaction mixture was kept in an ice bath for 1 hour and then allowed to gradually warm to room temperature overnight. After 16 hours, the reaction mixture was precipitated by gradually adding isopropanol (5x DCM volume) while stirring. The precipitate was collected by vacuum filtration, redissolved in DCM, and reprecipitated using isopropanol twice. The final precipitate was collected by vacuum filtration and dried in a vacuum oven at 40 ˚C for 48 hours. The precipitate was analyzed by ^{1}H-NMR, FTIR, GPC, DSC, and TGA.

C.2.2 Synthesis of Poly(HTy-co-50%phenylenediacetate Ester) (HP)

Yield: 88%. GPC: M_n = 84 kDa, M_w = 143 kDa, PDI = 1.7; DSC: T_g = 50 ˚C, T_{m1} = 131 ˚C, T_{m2}= 147 ˚C; TGA: T_d = 320 ˚C; ^{1}H NMR (500 MHz, DMSO-d_6, δ in ppm): 7.35 (s, 4H), 7.22 - 7.18 (m, 4H), 7.03 – 6.99 (m, 4H), 4.21 (t, *J* = 6.7 Hz, 2H), 3.92 (d, *J* = 4.4 Hz, 4H), 3.62 (s, 2H), 2.84 (t, *J* = 6.7 Hz, 2H), (Figure S1); FTIR (ATR) ν_{max} (cm^{-1}): 2917 (w), 1748 (m), 1728 (m), 1606 (w), 1506 (m), 1468 (w), 1422 (w), 1337 (w), 1218 (m), 1193 (m), 1165 (m), 1119 (s), 1017 (m), 915 (m), 807 (w), 788 (w), 689 (w), 648 (w).

C.2.3 Synthesis of Poly(HTy-co-45%phenylenediacetate-co-5%BocGlu ester) (HP5BG)

Yield: 94%. GPC: M_n = 80 kDa, M_w = 141 kDa, PDI = 1.8; DSC: T_g = 46 ˚C, T_{m1} = 125 ˚C, T_{m2} = 141 ˚C; TGA: T_d = 320 °C; ^{1}H NMR (500 MHz, DMSO-d_6, δ in ppm): 7.60 (s, 1H), 7.35 (s, 36H), 7.27 - 7.18 (m, 40H), 7.07 – 6.99 (m, 40H), 4.30 (s, 1H), 4.23 (t, J = 6.6 Hz, 20H), 3.93 (d, J = 4.2 Hz, 36H), 3.64 (s, 20H), 2.86 (t, J = 6.6 Hz, 20H), 2.75 (s, 2H), 2.28 – 2.19 (m, 1H), 2.13 – 2.04 (m, 1H), 1.39 (s, 9H), (Figure S2); FTIR (ATR) ν_{max} (cm^{-1}): 3035 (w), 2956 (w), 1749 (m), 1731 (m), 1607 (w), 1506 (m), 1423 (w), 1339 (w), 1300 (w), 1218 (m), 1193 (m), 1164 (m), 1120 (s), 1017 (m), 915 (m), 834 (w), 808 (w), 789 (w), 689 (w), 649 (w).

C.2.4 Synthesis of Poly(HTy-co-45%phenylenediacetate-co-5%Gluhexenamide Ester) (HP5GH)

Yield: 90%. GPC: M_n = 77 kDa, M_w = 126 kDa, PDI = 1.6; DSC: T_g = 47 ˚C, T_{m1} = 128 ˚C, T_{m2} = 143 ˚C; TGA: T_d = 320 ˚C; ^{1}H NMR (500 MHz, DMSO-d_6, δ in ppm): 8.51 – 8.47 (m, 1H), 7.34 (s, 36H), 7.25 - 7.16 (m, 40H), 7.05 - 6.98 (m, 40H), 5.82 - 5.69 (m, 1H), 5.01 - 4.88 (m, 2H), 4.59 - 4.49 (m, 1H), 4.21 (t, *J* = 6.6 Hz, 20H), 3.92 (d, *J* = 4.3 Hz, 36H), 3.62 (s, 20H), 2.84 (t, *J* = 6.6 Hz, 20H), 2.75 (s, 2H), 2.25 (m, 1H), 2.18 (t, *J* = 7.3 Hz, 2H), 2.13 - 2.05 (m, 1H), 2.05 - 1.99 (m, 2H), 1.64 - 1.56 (m, 2H), (Figure S3); FTIR (ATR) ν_{max} (cm^{-1}): 3035 (w), 2955 (w), 1749 (m), 1731 (m), 1674 (w), 1607 (w), 1506 (m), 1423 (w), 1338 (w), 1300 (w), 1218 (m), 1193 (m), 1164 (m), 1120 (s), 1017 (m), 915 (m), 844 (w), 808 (w), 789 (w), 688 (w), 648 (w).

C.2.5 Synthesis of Poly(HTy-co-45%phenylenediacetate -co-5%Glupentynamide Ester) (HP5GP)

Yield: 84%. GPC: M_n = 78 kDa, M_w = 129 kDa, PDI = 1.6; DSC: T_g = 50 ˚C, T_{m1} = 127 ˚C, T_{m2} = 144 ˚C; TGA: T_d = 320 ˚C; ^{1}H NMR (500 MHz, DMSO-d_6, δ in ppm): 8.62 - 8.58 (m, 1H), 7.34 (s, 36H), 7.25 - 7.17 (m, 40H), 7.06 - 6.98 (m, 40H), 4.59 - 4.52 (m, 1H), 4.21 (t, *J* = 6.7 Hz, 20H), 3.92 (d, *J* = 4.3 Hz, 36H), 3.62 (s, 20H), 2.84 (t, *J* = 6.7 Hz, 20H), 2.80 - 2.70 (m, 3H), 2.41 (s, 4H), 2.30 - 2.22 (m, 1H), 2.13 - 2.04 (m, 1H), (Figure S4); FTIR (ATR) ν_{max} (cm^{-1}): 3035 (w), 2956 (w), 1749 (m), 1731 (m), 1679 (w), 1607 (w), 1506 (m), 1423 (w), 1379 (w), 1338 (w), 1300 (m), 1218 (m), 1193 (m), 1164 (m), 1120 (s), 1017 (m), 915 (m), 844 (m), 808 (m), 789 (m), 688 (w), 649 (w), 596 (w), 556 (w).

C.3 Functionalization Studies

C.3.1 Bulk Reactivity of HP5GH and HP5GP

A solution of HP5GH (0.2 g in 2 mL DCM) was combined with 65 mg (3 equivalents) of 1*H*,1*H*,2*H*,2*H*-perflurodecanethiol and 10 mg of Irgacure-2959 (photoinitiator). The solution was transferred into a quartz cuvette and stirred with a magnetic stirrer. The solution was stirred under UV light (365 nm) for 5 hours. The solution was then added dropwise into a stirring solution of isopropanol to precipitate the polymer. The resulting residue was partially dried and re-dissolved in 2 mL DCM and reprecipitated to wash out the unreacted thiol. The resulting residue was filtered and dried in a vacuum oven at 40 ˚C. The reaction product was analyzed by ^{1}H and ^{19}F NMR.

C.3.2 Surface Reactivity of HP5GH with 1*H*,1*H*,2*H*,2*H*-perflurodecanethiol

Compression molded films of polymer HP5GH were cut into 5 mm diameter discs. Each disc was then kept in a Teflon dish and 10 µL solution of Irgacure-2959 in methanol (MeOH) and a 100 µL solution of 1*H*,1*H*,2*H*,2*H*-perflurodecanethiol in MeOH were added. The concentrations of the thiol and Irgacure-2959 are shown in **Table C.1**. Each film was then irradiated with UV for a predetermined time. The film was then flipped and identical amounts of Irgacure-2959 and 1*H*,1*H*,2*H*,2*H*-perflurodecanethiol were added to the other side and irradiated with UV. The UV source was kept at a distance of 14 cm and had a power of 3.6 mW/cm^2. For longer UV exposures, 50 µL of fresh MeOH was added on top to compensate for the loss of solvent due to evaporation. After irradiation of both sides, the film was transferred to a 1 dram vial and washed with 1 mL MeOH by vortexing for 20 seconds. The MeOH was separated and discarded and the washing was repeated 9 more time. Finally, each film was sonicated in 1 mL MeOH for 10 min, the MeOH was discarded, and the film was dried in a vacuum oven for 16 hours. The treated films were mounted on XPS instrument platform and data was collected for two distinct spots.

C.3.3 Surface Reactivity of HP5GH with Bovine Serum Albumin (BSA)

Two QCM gold plated crystals were spin coated with 2% (w/v) DCM solution of HP5GH and dried overnight under vacuum. A solution of 100 µl BSA (0.25 mg/mL) was placed on top of the crystals. To these crystals, a 50 µl solution of Irgacure-2959 (1mg/mL) was added (Irgacure-2959 was dissolved by stirring in DPBS for 1 hour). One crystal was then placed under UV light (365 nm) for 5 min and another was kept in dark. Then the crystals were rinsed by 10 mL DPBS. The crystals were then placed in the QCM chamber and the frequency was measured while a flow of DPBS was maintained. The frequency data was

converted to areal mass using the Sauerbrey equation.

C.4 Surface Reactivity of HP5GP with Az-Heparin

C.4.1 Synthesis of Az-Heparin

A batch of 376 mg of Heparin (5 kDa) was combined with 25.9 mg of imidazole sulfonyl azide tetrafluoroborate, 30 mg of potassium carbonate, and 7.7 mg of copper sulfate pentahydrate and dissolved in 37.5 mL deionized (DI) water. The reaction was stirred overnight, then dialyzed for 24 hours using D7884 dialysis membrane from Sigma-Aldrich, and lyophilized to obtain a white powdered residue.

C.4.2 QCM Experiment of HP5GP with Az-Heparin and BMP-2.

A QCM gold plated crystal was spin coated with 2% (w/v) DCM solution of HP5GP and dried overnight under vacuum. The polymer coated crystal was then loaded on QSENSE module and flowed over with DPBS until a stable baseline was achieved. Then a solution of az-Heparin (1mg/ml) mixed with 0.1 mg copper sulfate pentahydrate and 1 mg of sodium ascorbate was flowed over the polymer coated QCM crystal until an equilibrium was reached, then DPBS was flowed over the polymer coated surface to remove the unreacted az-Heparin. Then a solution of BMP-2 (24 µg/ml) was flowed over the coated QCM crystal until an equilibrium was reached. Then DPBS solution was flowed over the QCM crystal.

C.4.3QCM Control Experiment 1: HP5GP/HP + Az-Heparin. A QCM gold plated crystal was spin coated with 2% (w/v) DCM solution of HP5GP or 2% (w/v) HP and dried overnight under vacuum. The polymer coated crystal was then loaded on QSENSE module and flowed over with DI water until a stable baseline was achieved. Then a solution of az-

Heparin (1mg/ml) mixed with 0.1 mg copper sulfate pentahydrate and 1 mg of sodium ascorbate was flowed over the polymer coated QCM crystal for 6 hours. Then a solution of sodium dodecyl sulfate (2% aqueous) was flowed for 30 min followed by DI water overnight.

C.4.4 QCM Control Experiment 2: HP5GP + BMP-2. A QCM gold plated crystal was spin coated with 2% (w/v) DCM solution of HP5GP and dried overnight under vacuum. The polymer coated crystal was then loaded on QSENSE module and flowed over with DPBS until a stable baseline was achieved. Then a solution of BMP-2 (24 µg/ml) was flowed over the coated QCM crystal until an equilibrium was reached. Then DPBS solution was flowed over the QCM crystal.

Table C.1 The List of Results from Reactions between HP5GP and 1*H*,1*H*,2*H*,2*H*-perfluorodecanethiol

Expt No.	Polymer	Thiol (mg)	Photoinitiator (mg)	UV Exposure Time (min)	%C (Avg)	%O (Avg)	%F (Avg)	%F/%C	Corrected %F/%C	% reaction
1	HP5Gluhexe	1	0.01	5	78.63	18.505	1.935	0.0246	0.0232	55
2	HP5Gluhexe	0.5	0.01	5	81.01	18.075	0.465	0.0057	0.0043	10
3	HP5Gluhexe	0.1	0.01	5	81.125	17.96	0.1	0.0012	-0.0002	0
4	HP5Gluhexe	0.05	0.01	5	81.98	17.385	0.055	0.0007	-0.0008	0
5	HP5Gluhexe	0.01	0.01	5	80.375	18.38	0.11	0.0014	-0.0001	0
6	HP5Gluhexe	0.1	0.01	1	81.9	17.455	0.16	0.0020	0.0005	1
7	HP5Gluhexe	0.1	0.01	0.5	81.53	17.85	0.12	0.0015	0.0000	0
8	HP5Gluhexe	0.1	0.01	30	81.77	17.21	0.27	0.0033	0.0019	4
9	HP	1	0.01	5	80.75	18.435	0.115	0.0014	0.0000	0
10	HP	1	0.01	30	80.99	18.49	0.16	0.0020	0.0000	0
11	HP5Gluhexe	0	0	0	81.54	17.94	0.075	0.0009		
12	HP5Gluhexe	1	0.01	1	80.56	18.63	0.81	0.0100	0.0086	20
13	HP5Gluhexe	1	0.01	5	80.03	18.53	1.44	0.0179	0.0165	39
14	HP5Gluhexe	1	0.5	1	80.71	18.19	1.10	0.0137	0.0122	29
15	HP5Gluhexe	1	0.5	5	79.68	18.18	2.14	0.0268	0.0254	60
16	HP5Gluhexe	0.5	0.5	5	80.75	17.97	1.28	0.0159	0.0144	34
17	HP5Gluhexe	1	0.5	15	80.39	17.76	1.86	0.0231	0.0212	50
18	HP5Gluhexe	1	0.01	15	78.36	18.40	3.25	0.0414	0.0394	94
19	HP5Gluhexe	1	0.1	5	79.88	17.89	2.23	0.0279	0.0265	63

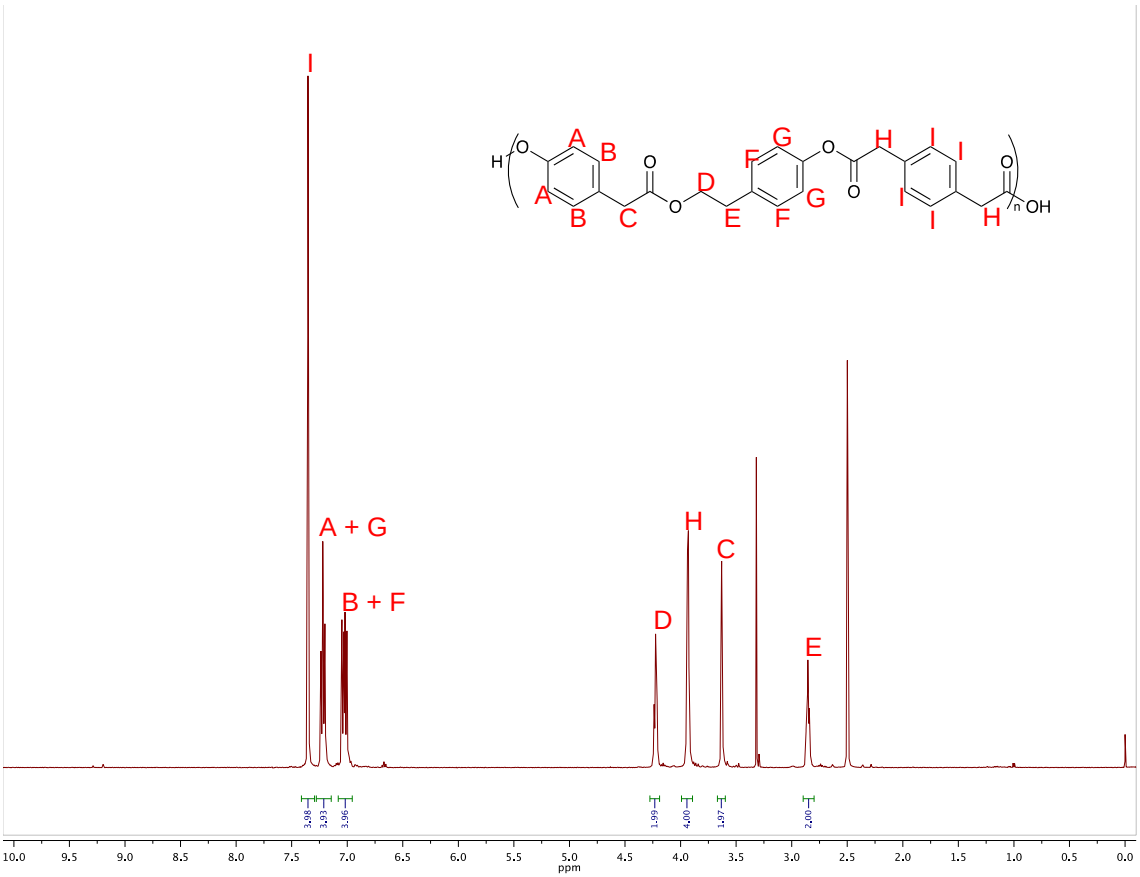

Figure C.1 ^{1}H NMR spectra of HP

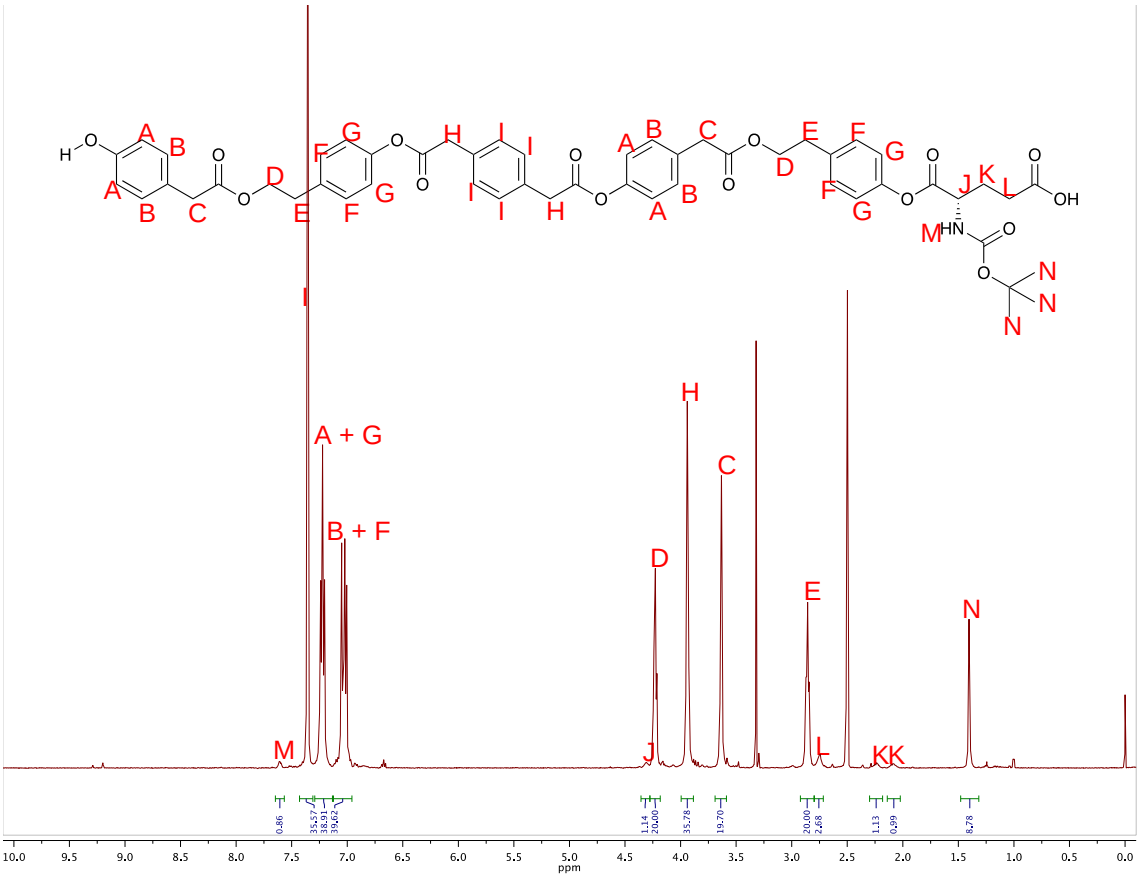

Figure C.2 ^{1}H NMR spectra of HP5BG

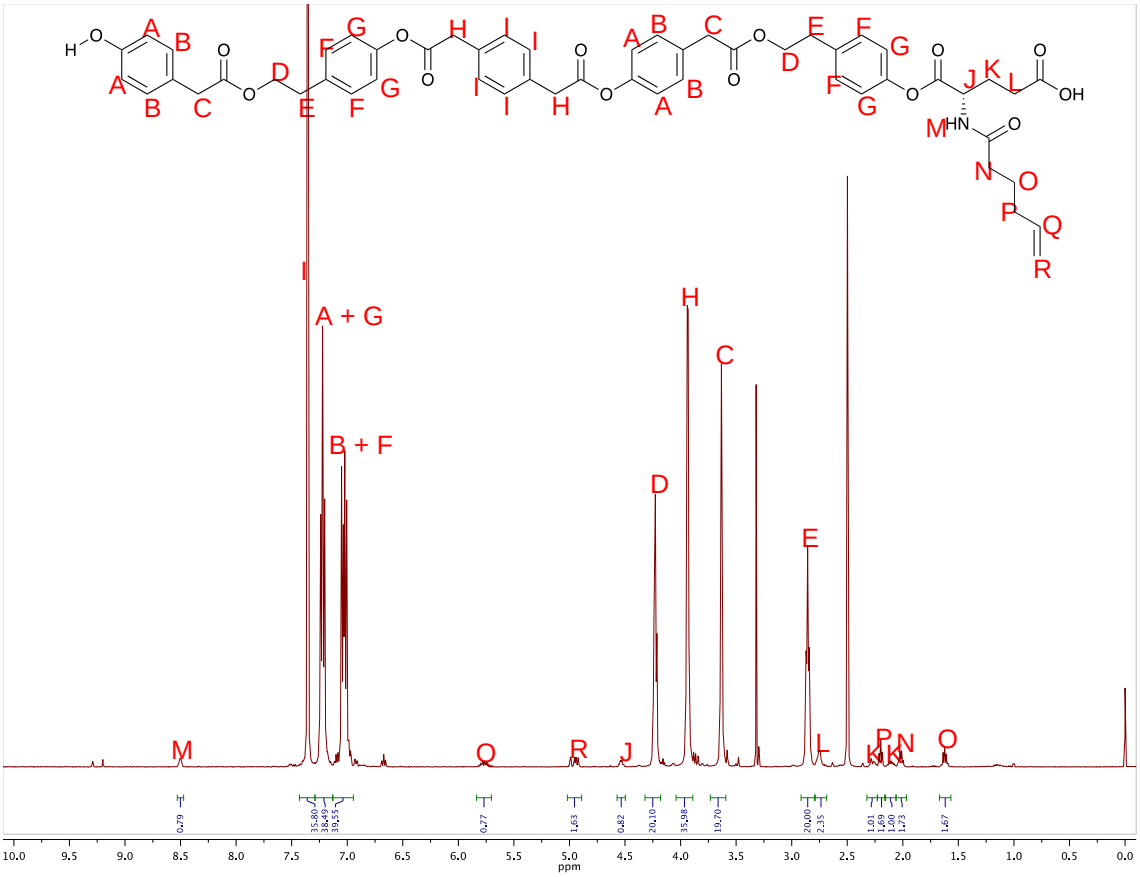

Figure C.3 ^{1}H NMR spectra of HP5GH

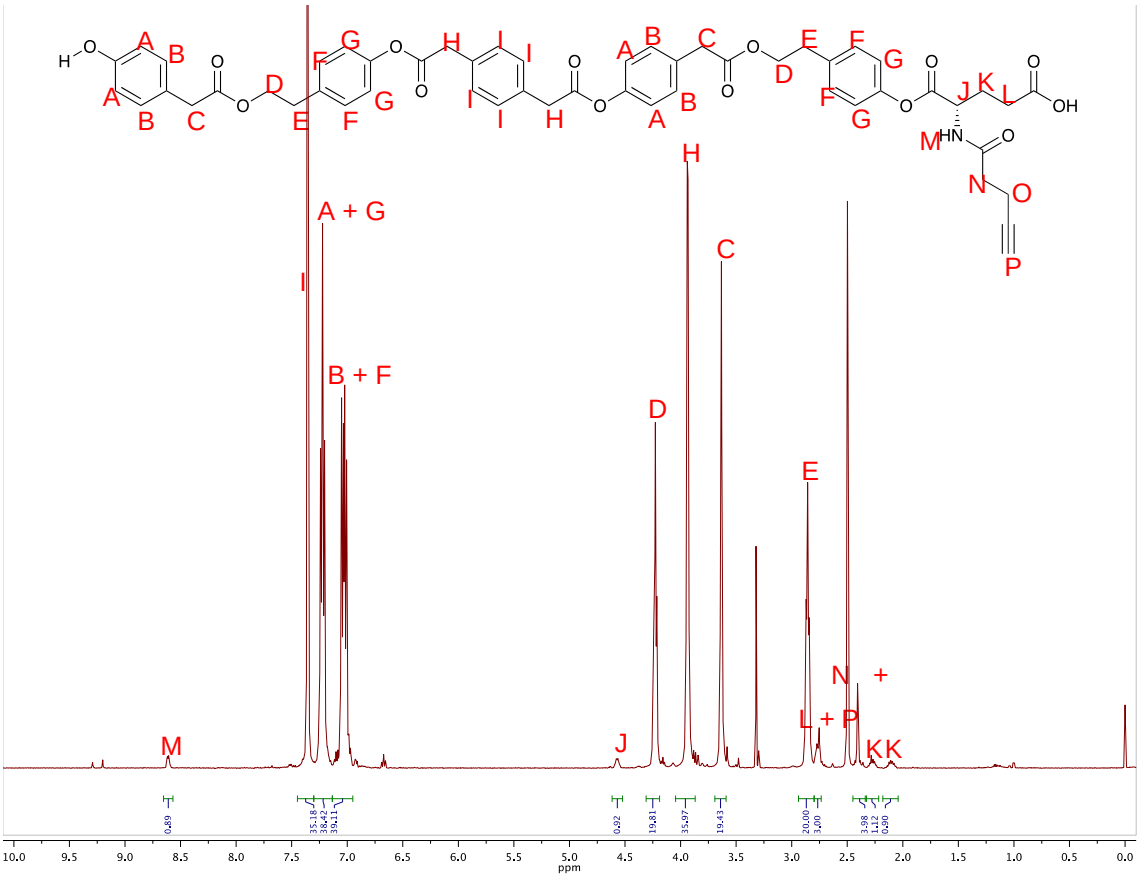

Figure C.4 ^{1}H NMR spectra of HP5GP

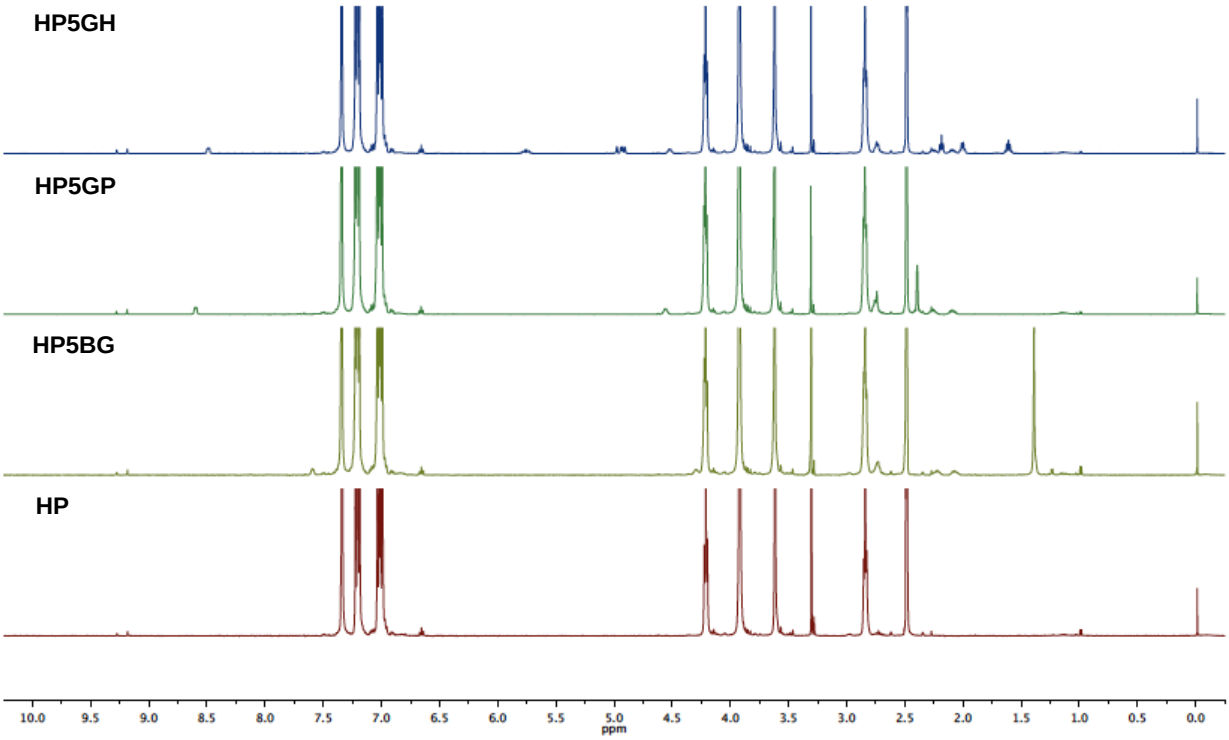

Figure C.5 Stacked ^{1}H NMR spectra for the polymers.

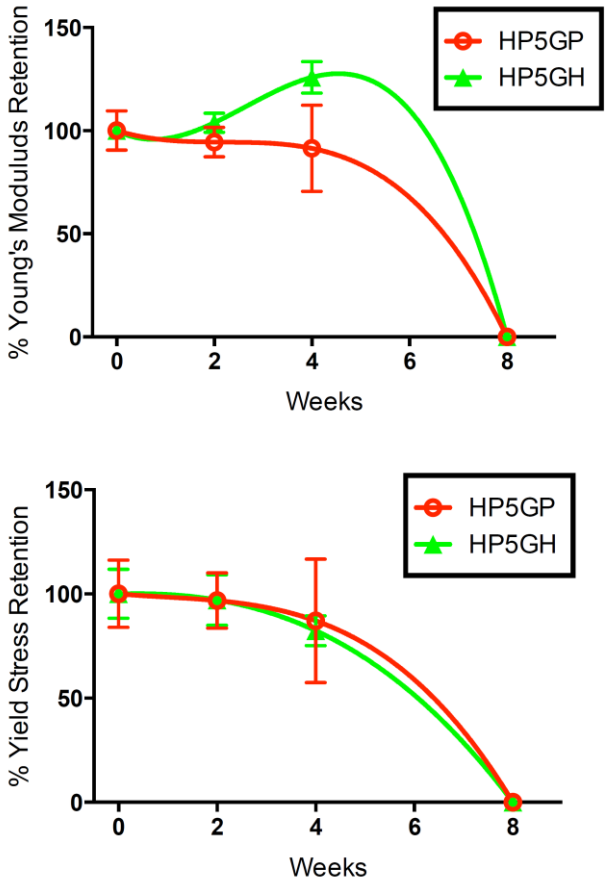

Figure C.6 Left: Young's modulus over time at 37 ˚C in DPBS; Right: Yield strength over time at 37 ˚C in DPBS.

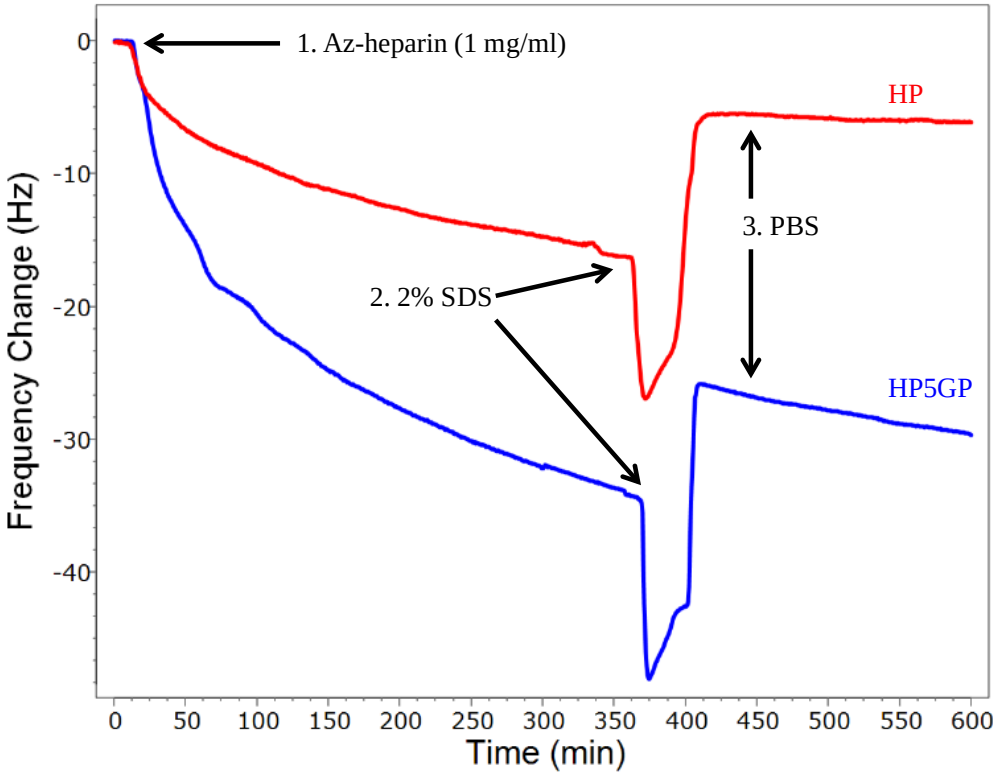

Figure C.7 Graph of frequency change over time when az-Heparin, 2% SDS, and DPBS were flowed over a QCM crystal coated with HP5GP.

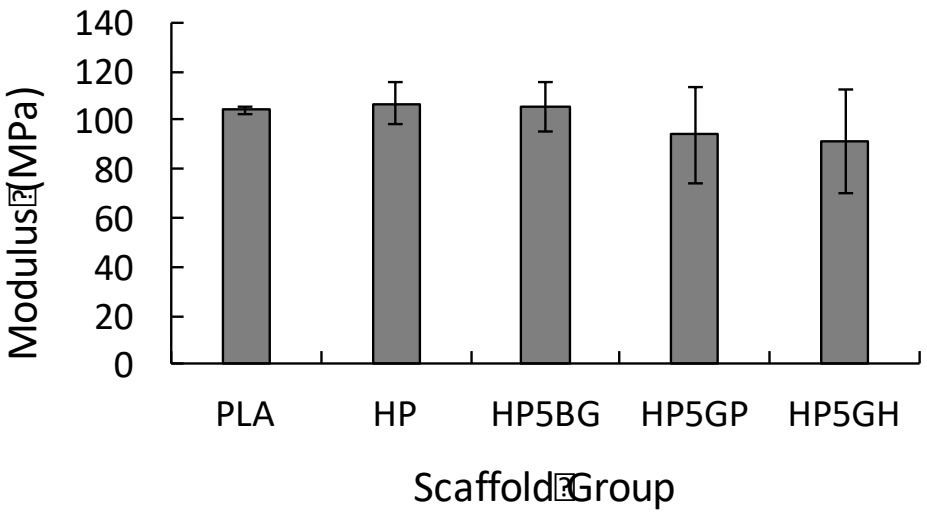

Figure C.8 Young's modulus values of the 3D printed scaffolds.

REFERENCES

[1] R. Langer, J.P. Vacanti, Tissue Engineering, American Association for the Advancement of Science Vol. 260(No. 5110) (1993) pp. 920.

[2] Y.S. Zhang, M. Duchamp, R. Oklu, L.W. Ellisen, R. Langer, A. Khademhosseini, Bioprinting the Cancer Microenvironment, ACS Biomaterials Science & Engineering 2(10) (2016) 1710.

[3] M.W. Tibbitt, C.B. Rodell, J.A. Burdick, K.S. Anseth, Progress in Material Design for Biomedical Applications, Proceedings of the National Academy of Sciences 112(47) (2015) 14444.

[4] K.H. Benam, S. Dauth, B. Hassel, A. Herland, A. Jain, K.J. Jang, K. Karalis, H.J. Kim, L. MacQueen, R. Mahmoodian, S. Musah, Y.S. Torisawa, A.D. van der Meer, R. Villenave, M. Yadid, K.K. Parker, D.E. Ingber, Engineered in Vitro Disease Models, Annual Review of Pathology 10 (2015) 195.

[5] D.G. Nguyen, J. Funk, J.B. Robbins, C. Crogan-Grundy, S.C. Presnell, T. Singer, A.B. Roth, Bioprinted 3D Primary Liver Tissues Allow Assessment of Organ-Level Response to Clinical Drug Induced Toxicity in Vitro, PLoS One 11(7) (2016) e0158674.

[6] L.G. Griffith, G. Naughton, Tissue Engineering - Current Challenges and Expanding Opportunities, Science 295(5557) (2002) 1009.

[7] P. Bajaj, R.M. Schweller, A. Khademhosseini, J.L. West, R. Bashir, 3D Biofabrication Strategies for Tissue Engineering and Regenerative Medicine, Annual Review of Biomedical Engineering 16(1) (2014) 247.

[8] N. Groen, M. Guvendiren, H. Rabitz, W.J. Welsh, J. Kohn, J. de Boer, Stepping into the Omics Era: Opportunities and Challenges for Biomaterials Science and Engineering, Acta Biomaterialia 34 (2016) 133.

[9] S.V. Murphy, A. Atala, 3D Bioprinting of Tissues and Organs, Nature Biotechnology 32(8) (2014) 773.

[10] A. Shafiee, A. Atala, Printing Technologies for Medical Applications, Trends in Molecular Medicine 22(3) (2016) 254.

[11] C. Mandrycky, Z. Wang, K. Kim, D.H. Kim, 3D Bioprinting for Engineering Complex Tissues, Biotechnology Advances 34(4) (2016) 422.

[12] I.T. Ozbolat, W. Peng, V. Ozbolat, Application Areas of 3D Bioprinting, Drug Discovery Today 21(8) (2016) 1257.

[13] M. Guvendiren, J. Molde, R.M.D. Soares, J. Kohn, Designing Biomaterials for 3D Printing, ACS Biomaterials Science & Engineering 2(10) (2016) 1679.

[14] F. Guillemot, V. Mironov, M. Nakamura, Bioprinting Is Coming of Age: Report from the International Conference on Bioprinting and Biofabrication in Bordeaux (3b'09), Biofabrication 2(1) (2010) 010201.

[15] M. Guvendiren, J.A. Burdick, Engineering Synthetic Hydrogel Microenvironments to Instruct Stem Cells, Current Opinion in Biotechnology 24(5) (2013) 841.

[16] A.J. Ryan, C.M. Brougham, C.D. Garciarena, S.W. Kerrigan, F.J. O'Brien, Towards 3D in Vitro Models for the Study of Cardiovascular Tissues and Disease, Drug Discovery Today 21(9) (2016) 1437.

[17] C.I. Johnson, D.J. Argyle, D.N. Clements, In Vitro Models for the Study of Osteoarthritis, The Veterinary Journal 209 (2016) 40.

[18] B. N. Turner, R. Strong, S. A. Gold, A Review of Melt Extrusion Additive Manufacturing Processes: I. Process Design and Modeling, Rapid Prototyping Journal 20(3) (2014) 192.

[19] I.T. Ozbolat, M. Hospodiuk, Current Advances and Future Perspectives in Extrusion-Based Bioprinting, Biomaterials 76 (2016) 321.

[20] H. Gudapati, M. Dey, I. Ozbolat, A Comprehensive Review on Droplet-Based Bioprinting: Past, Present and Future, Biomaterials 102 (2016) 20.

[21] M. Nakamura, A. Kobayashi, F. Takagi, A. Watanabe, Y. Hiruma, K. Ohuchi, Y. Iwasaki, M. Horie, I. Morita, S. Takatani, Biocompatible Inkjet Printing Technique for Designed Seeding of Individual Living Cells, Tissue Engineering 11(11-12) (2005) 1658.

[22] W.C. Wilson Jr, T. Boland, Cell and Organ Printing 1: Protein and Cell Printers, Anatomical Record - Part A Discoveries in Molecular, Cellular, and Evolutionary Biology 272(2) (2003) 491.

[23] V. Mironov, T. Boland, T. Trusk, G. Forgacs, R.R. Markwald, Organ Printing: Computer-Aided Jet-Based 3D Tissue Engineering, Trends in Biotechnology 21(4) (2003) 157.

[24] S. Seyed Farid Seyed, G. Samira, M. Mehdi, Y. Hooman, M. Hendrik Simon Cornelis, K. Nahrizul Adib, O. Noor Azuan Abu, A Review on Powder-Based Additive Manufacturing for Tissue Engineering: Selective Laser Sintering and Inkjet 3D Printing, Science and Technology of Advanced Materials 16(3) (2015) 033502.

[25] H. Miyanaji, S. Zhang, A. Lassell, A. Zandinejad, L. Yang, Process Development of Porcelain Ceramic Material with Binder Jetting Process for Dental Applications, Jom 68(3) (2016) 831.

[26] S.A. Skoog, P.L. Goering, R.J. Narayan, Stereolithography in Tissue Engineering, Journal of Materials Science: Materials in Medicine 25(3) (2014) 845.

[27] H. Cui, M. Nowicki, J.P. Fisher, L.G. Zhang, 3D Bioprinting for Organ Regeneration, Advanced Healthcare Materials (2016).

[28] A.B. Dababneh, I.T. Ozbolat, Bioprinting Technology: A Current State-of-the-Art Review, Journal of Manufacturing Science and Engineering 136(6) (2014) 061016.

[29] K.K.M. Ibrahim T. Ozbolat, Hemanth Gudapati, Evaluation of Bioprinter Technologies, Additive Manufacturing (2016).

[30] Y. Nishiyama, M. Nakamura, C. Henmi, K. Yamaguchi, S. Mochizuki, H. Nakagawa, K. Takiura, Development of a Three-Dimensional Bioprinter: Construction of Cell Supporting Structures Using Hydrogel and State-of-the-Art Inkjet Technology, Journal of Biomechanical Engineering 131(3) (2008) 035001.

[31] W.S. Choi, D. Ha, S. Park, T. Kim, Synthetic Multicellular Cell-to-Cell Communication in Inkjet Printed Bacterial Cell Systems, Biomaterials 32(10) (2011) 2500.

[32] L. Elomaa, C.-C. Pan, Y. Shanjani, A. Malkovskiy, J.V. Seppälä, Y. Yang, Three-Dimensional Fabrication of Cell-Laden Biodegradable Poly(Ethylene Glycol-Co-Depsipeptide) Hydrogels by Visible Light Stereolithography, Journal of Materials Chemistry B 3(42) (2015) 8348.

[33] V.B. Morris, S. Nimbalkar, M. Younesi, P. McClellan, O. Akkus, Mechanical Properties, Cytocompatibility and Manufacturability of Chitosan:Pegda Hybrid-Gel Scaffolds by Stereolithography, Annals of Biomedical Engineering 45(1) (2017) 286.

[34] Z. Wang, R. Abdulla, B. Parker, R. Samanipour, S. Ghosh, K. Kim, A Simple and High-Resolution Stereolithography-Based 3D Bioprinting System Using Visible Light Crosslinkable Bioinks, Biofabrication 7(4) (2015) 045009.

[35] L. Koch, S. Kuhn, H. Sorg, M. Gruene, S. Schlie, R. Gaebel, B. Polchow, K. Reimers, S. Stoelting, N. Ma, P.M. Vogt, G. Steinhoff, B. Chichkov, Laser Printing of Skin Cells and Human Stem Cells, Tissue Engineering Part C: Methods 16(5) (2010).

[36] J.A. Barron, B.J. Spargo, B.R. Ringeisen, Biological Laser Printing of Three Dimensional Cellular Structures, Applied Physics A: Materials Science and Processing 79(4-6) (2004) 1027.

[37] J.A. Barron, P. Wu, H.D. Ladouceur, B.R. Ringeisen, Biological Laser Printing: A Novel Technique for Creating Heterogeneous 3-Dimensional Cell Patterns, Biomedical Microdevices 6(2) (2004) 139.

[38] A. Doraiswamy, R.J. Narayan, T. Lippert, L. Urech, A. Wokaun, M. Nagel, B. Hopp, M. Dinescu, R. Modi, R.C.Y. Auyeung, D.B. Chrisey, Excimer Laser Forward Transfer of Mammalian Cells Using a Novel Triazene Absorbing Layer, Applied Surface Science 252(13 SPEC. ISS.) (2006) 4743.

[39] B.R. Ringeisen, H. Kim, J.A. Barron, D.B. Krizman, D.B. Chrisey, S. Jackman, R.Y.C. Auyeung, B.J. Spargo, Laser Printing of Pluripotent Embryonal Carcinoma Cells, Tissue Engineering 10(3-4) (2004) 483.

[40] B. Hopp, T. Smausz, N. Kresz, N. Barna, Z. Bor, L. Kolozsvári, D.B. Chrisey, A. Szabó, A. Nógrádi, Survival and Proliferative Ability of Various Living Cell Types after Laser-Induced Forward Transfer, Tissue Engineering 11(11-12) (2005) 1817.

[41] M. Guvendiren, J. Molde, R.M.D. Soares, J. Kohn, Designing Biomaterials for 3D Printing, ACS Biomaterials Science & Engineering (2016).

[42] R.R. Jose, M.J. Rodriguez, T.A. Dixon, F. Omenetto, D.L. Kaplan, Evolution of Bioinks and Additive Manufacturing Technologies for 3D Bioprinting, ACS Biomaterials Science & Engineering 2(10) (2016) 1662.

[43] A. Munaz, R.K. Vadivelu, J. St. John, M. Barton, H. Kamble, N.-T. Nguyen, Three-Dimensional Printing of Biological Matters, Journal of Science: Advanced Materials and Devices 1(1) (2016) 1.

[44] M. Hospodiuk, M. Dey, D. Sosnoski, I.T. Ozbolat, The Bioink: A Comprehensive Review on Bioprintable Materials, Biotechnology Advances 35(2) (2017) 217.

[45] P.S. Gungor-Ozkerim, I. Inci, Y.S. Zhang, A. Khademhosseini, M.R. Dokmeci, Bioinks for 3D Bioprinting: An Overview, Biomaterials Science 6(5) (2018) 915.

[46] S. Ji, M. Guvendiren, Recent Advances in Bioink Design for 3D Bioprinting of Tissues and Organs, Frontiers in Bioengineering and Biotechnology 5 (2017) 23.

[47] N.E. Fedorovich, J. Alblas, J.R. De Wijn, W.E. Hennink, A.B.J. Verbout, W.J.A. Dhert, Hydrogels as Extracellular Matrices for Skeletal Tissue Engineering: State-of-the-Art and Novel Application in Organ Printing, Tissue Engineering 13(8) (2007) 1905.

[48] C. Storm, J.J. Pastore, F.C. MacKintosh, T.C. Lubensky, P.A. Janmey, Nonlinear Elasticity in Biological Gels, Nature 435(7039) (2005) 191.

[49] M.L. Gardel, J.H. Shin, F.C. MacKintosh, L. Mahadevan, P. Matsudaira, D.A. Weitz, Elastic Behavior of Cross-Linked and Bundled Actin Networks, Science 304(5675) (2004) 1301.

[50] J.A. Burdick, G.D. Prestwich, Hyaluronic Acid Hydrogels for Biomedical Applications, Advanced Materials 23(12) (2011) H41.

[51] M. Ribeiro, M.A. de Moraes, M.M. Beppu, M.P. Garcia, M.H. Fernandes, F.J. Monteiro, M.P. Ferraz, Development of Silk Fibroin/Nanohydroxyapatite Composite Hydrogels for Bone Tissue Engineering, European Polymer Journal 67 (2015) 66.

[52] F. Pati, J. Jang, D.H. Ha, S. Won Kim, J.W. Rhie, J.H. Shim, D.H. Kim, D.W. Cho, Printing Three-Dimensional Tissue Analogues with Decellularized Extracellular Matrix Bioink, Nature Communications 5 (2014) 3935.

[53] A. Abaci, M. Guvendiren, Designing Decellularized Extracellular Matrix-Based Bioinks for 3D Bioprinting, Advanced Healthcare Materials (2020) e2000734.

[54] P.J. Schaner, N.D. Martin, T.N. Tulenko, I.M. Shapiro, N.A. Tarola, R.F. Leichter, R.A. Carabasi, P.J. Dimuzio, Decellularized Vein as a Potential Scaffold for Vascular Tissue Engineering, Journal of Vascular Surgery 40(1) (2004) 146.

[55] B.N. Brown, S.F. Badylak, Extracellular Matrix as an Inductive Scaffold for Functional Tissue Reconstruction, Translational Research 163(4) (2014) 268.

[56] S.F. Badylak, D. Taylor, K. Uygun, Whole-Organ Tissue Engineering: Decellularization and Recellularization of Three-Dimensional Matrix Scaffolds, Annual Review of Biomedical Engineering 13 (2011) 27.

[57] G. Gao, H. Kim, B.S. Kim, J.S. Kong, J.Y. Lee, B.W. Park, S. Chae, J. Kim, K. Ban, J. Jang, H.-J. Park, D.-W. Cho, Tissue-Engineering of Vascular Grafts Containing Endothelium and Smooth-Muscle Using Triple-Coaxial Cell Printing, Applied Physics Reviews 6(4) (2019) 041402.

[58] J. Jang, H.J. Park, S.W. Kim, H. Kim, J.Y. Park, S.J. Na, H.J. Kim, M.N. Park, S.H. Choi, S.H. Park, S.W. Kim, S.M. Kwon, P.J. Kim, D.W. Cho, 3D Printed Complex Tissue Construct Using Stem Cell-Laden Decellularized Extracellular Matrix Bioinks for Cardiac Repair, Biomaterials 112 (2016) 264.

[59] N. Noor, A. Shapira, R. Edri, I. Gal, L. Wertheim, T. Dvir, 3D Printing of Personalized Thick and Perfusable Cardiac Patches and Hearts, Advanced Science 6(11) (2019) 1900344.

[60] G. Forgacs, R.A. Foty, Biological Relevance of Tissue Liquidity and Viscoelasticity, in: A. Deutsch, J. Howard, M. Falcke, W. Zimmermann (Eds.), Function and Regulation of Cellular Systems, Birkhäuser Basel, Basel, 2004, pp. 269.

[61] F. Marga, A. Neagu, I. Kosztin, G. Forgacs, Developmental Biology and Tissue Engineering, Birth Defects Research Part C: Embryo Today: Reviews 81(4) (2007) 320.

[62] W.C. Wilson, Jr., T. Boland, Cell and Organ Printing 1: Protein and Cell Printers, The Anatomical Record Part A Discoveries in Molecular Cellular and Evolutionary Biology 272(2) (2003) 491.

[63] C. Norotte, F.S. Marga, L.E. Niklason, G. Forgacs, Scaffold-Free Vascular Tissue Engineering Using Bioprinting, Biomaterials 30(30) (2009) 5910.

[64] K. Jakab, F. Marga, C. Norotte, K. Murphy, G. Vunjak-Novakovic, G. Forgacs, Tissue Engineering by Self-Assembly and Bio-Printing of Living Cells, Biofabrication 2(2) (2010) 022001.

[65] K. Christensen, C. Xu, W. Chai, Z. Zhang, J. Fu, Y. Huang, Freeform Inkjet Printing of Cellular Structures with Bifurcations, Biotechnology and Bioengineering 112(5) (2015) 1047.

[66] P.A. Fleming, W.S. Argraves, C. Gentile, A. Neagu, G. Forgacs, C.J. Drake, Fusion of Uniluminal Vascular Spheroids: A Model for Assembly of Blood Vessels, Developmental dynamics : an official publication of the American Association of Anatomists 239(2) (2010) 398.

[67] G. Forgacs, R.A. Foty, Y. Shafrir, M.S. Steinberg, Viscoelastic Properties of Living Embryonic Tissues: A Quantitative Study, Biophysical Journal 74(5) (1998) 2227.

[68] K. Jakab, A. Neagu, V. Mironov, R.R. Markwald, G. Forgacs, Engineering Biological Structures of Prescribed Shape Using Self-Assembling Multicellular Systems, Proceedings of the National Academy of Sciences of the United States of America 101(9) (2004) 2864.

[69] O. Jeon, Y.B. Lee, H. Jeong, S.J. Lee, D. Wells, E. Alsberg, Individual Cell-Only Bioink and Photocurable Supporting Medium for 3D Printing and Generation of Engineered Tissues with Complex Geometries, Materials Horizons 6(8) (2019) 1625.

[70] T.J. Hinton, Q. Jallerat, R.N. Palchesko, J.H. Park, M.S. Grodzicki, H.-J. Shue, M.H. Ramadan, A.R. Hudson, A.W. Feinberg, Three-Dimensional Printing of Complex Biological Structures by Freeform Reversible Embedding of Suspended Hydrogels, Science Advances 1(9) (2015).

[71] B. Ayan, D.N. Heo, Z. Zhang, M. Dey, A. Povilianskas, C. Drapaca, I.T. Ozbolat, Aspiration-Assisted Bioprinting for Precise Positioning of Biologics, Science Advances 6(10) (2020) eaaw5111.

[72] T. Serra, M.A. Mateos-Timoneda, J.A. Planell, M. Navarro, 3D Printed Pla-Based Scaffolds, Organogenesis 9(4) (2013) 239.

[73] S. Ji, M. Guvendiren, 3D Printed Wavy Scaffolds Enhance Mesenchymal Stem Cell Osteogenesis, Micromachines (Basel) 11(1) (2019).

[74] M.F. Arif, S. Kumar, K.M. Varadarajan, W.J. Cantwell, Performance of Biocompatible Peek Processed by Fused Deposition Additive Manufacturing, Materials & Design 146 (2018) 249.

[75] B.C. Tellis, J.A. Szivek, C.L. Bliss, D.S. Margolis, R.K. Vaidyanathan, P. Calvert, Trabecular Scaffolds Created Using Micro Ct Guided Fused Deposition Modeling, Materials Science and Engineering C 28(1) (2009) 171.

[76] D.H. Rosenzweig, E. Carelli, T. Steffen, P. Jarzem, L. Haglund, 3D-Printed Abs and Pla Scaffolds for Cartilage and Nucleus Pulposus Tissue Regeneration, International Journal of Molecular Sciences 16(7) (2015) 15118.

[77] J. Xiao, Y. Gao, The Manufacture of 3D Printing of Medical Grade Tpu, Progress in Additive Manufacturing 2(3) (2017) 117.

[78] X. Chen, C. Gao, J. Jiang, Y. Wu, P. Zhu, G. Chen, 3D Printed Porous Pla/Nha Composite Scaffolds with Enhanced Osteogenesis and Osteoconductivity in Vivo for Bone Regeneration, Biomedical Materials 14(6) (2019) 065003.

[79] S.F. Shirazi, S. Gharehkhani, M. Mehrali, H. Yarmand, H.S. Metselaar, N. Adib Kadri, N.A. Osman, A Review on Powder-Based Additive Manufacturing for Tissue Engineering: Selective Laser Sintering and Inkjet 3D Printing, Science and Technology of Advanced Materials 16(3) (2015) 033502.

[80] F.P.W. Melchels, J. Feijen, D.W. Grijpma, A Poly(D,L-Lactide) Resin for the Preparation of Tissue Engineering Scaffolds by Stereolithography, Biomaterials 30(23) (2009) 3801.

[81] E.P. Childers, M.O. Wang, M.L. Becker, J.P. Fisher, D. Dean, 3D Printing of Resorbable Poly(Propylene Fumarate) Tissue Engineering Scaffolds, MRS Bulletin 40(2) (2015) 119.

[82] H.W. Kang, S.J. Lee, I.K. Ko, C. Kengla, J.J. Yoo, A. Atala, A 3D Bioprinting System to Produce Human-Scale Tissue Constructs with Structural Integrity, Nature Biotechnology 34(3) (2016) 312.

[83] U. Ripamonti, Osteoinduction in Porous Hydroxyapatite Implanted in Heterotopic Sites of Different Animal Models, Biomaterials 17(1) (1996) 31.

[84] S.J. Kalita, S. Bose, H.L. Hosick, A. Bandyopadhyay, Development of Controlled Porosity Polymer-Ceramic Composite Scaffolds Via Fused Deposition Modeling, Materials Science and Engineering: C 23(5) (2003) 611.

[85] G. Allen Brady, W. Halloran John, Stereolithography of Ceramic Suspensions, Rapid Prototyping Journal 3(2) (1997) 61.

[86] J.A. Gonzalez, J. Mireles, Y. Lin, R.B. Wicker, Characterization of Ceramic Components Fabricated Using Binder Jetting Additive Manufacturing Technology, Ceramics International 42(9) (2016) 10559.

[87] W. Du, X. Ren, C. Ma, Z. Pei, Ceramic Binder Jetting Additive Manufacturing: Particle Coating for Increasing Powder Sinterability and Part Strength, Materials Letters 234 (2019) 327.

[88] W. Kim, C.H. Jang, G. Kim, Optimally Designed Collagen/Polycaprolactone Biocomposites Supplemented with Controlled Release of Ha/Tcp/Rhbmp-2 and Ha/Tcp/Prp for Hard Tissue Regeneration, Materials Science and Engineering: C 78 (2017) 763.

[89] J. Groll, J.A. Burdick, D.W. Cho, B. Derby, M. Gelinsky, S.C. Heilshorn, T. Jungst, J. Malda, V.A. Mironov, K. Nakayama, A. Ovsianikov, W. Sun, S. Takeuchi, J.J. Yoo, T.B.F. Woodfield, A Definition of Bioinks and Their Distinction from Biomaterial Inks, Biofabrication 11(1) (2018) 013001.

[90] N.E. Fedorovich, W. Schuurman, H.M. Wijnberg, H.J. Prins, P.R. van Weeren, J. Malda, J. Alblas, W.J. Dhert, Biofabrication of Osteochondral Tissue Equivalents by Printing Topologically Defined, Cell-Laden Hydrogel Scaffolds, Tissue Engineering Part C: Methods 18(1) (2012) 33.

[91] Y. Zhao, R. Yao, L. Ouyang, H. Ding, T. Zhang, K. Zhang, S. Cheng, W. Sun, Three-Dimensional Printing of Hela Cells for Cervical Tumor Model in Vitro, Biofabrication 6(3) (2014) 035001.

[92] W. Sun, B. Starly, A.C. Daly, J.A. Burdick, J. Groll, G. Skeldon, W. Shu, Y. Sakai, M. Shinohara, M. Nishikawa, J. Jang, D.W. Cho, M. Nie, S. Takeuchi, S. Ostrovidov, A. Khademhosseini, R.D. Kamm, V. Mironov, L. Moroni, I.T. Ozbolat, The Bioprinting Roadmap, Biofabrication 12(2) (2020) 022002.

[93] H. Tetsuka, S.R. Shin, Materials and Technical Innovations in 3D Printing in Biomedical Applications, Journal of Materials Chemistry B 8(15) (2020) 2930.

[94] P. Thayer, H. Martinez, E. Gatenholm, History and Trends of 3D Bioprinting, in: J.M. Crook (Ed.), 3D Bioprinting: Principles and Protocols, Springer US, New York, NY, 2020, pp. 3..

[95] J. Li, C. Wu, P.K. Chu, M. Gelinsky, 3D Printing of Hydrogels: Rational Design Strategies and Emerging Biomedical Applications, Materials Science and Engineering: R: Reports 140 (2020) 100543.

[96] H.C.H. Ko, B.K. Milthorpe, C.D. McFarland, Engineering Thick Tissues - the Vascularisation Problem, European Cells and Materials 14 (2007) 1.

[97] P. Zorlutuna, N. Annabi, G. Camci-Unal, M. Nikkhah, J.M. Cha, J.W. Nichol, A. Manbachi, H. Bae, S. Chen, A. Khademhosseini, Microfabricated Biomaterials for Engineering 3D Tissues, Advanced Materials 24(14) (2012) 1782.

[98] J.S. Miller, K.R. Stevens, M.T. Yang, B.M. Baker, D.H. Nguyen, D.M. Cohen, E. Toro, A.A. Chen, P.A. Galie, X. Yu, R. Chaturvedi, S.N. Bhatia, C.S. Chen, Rapid Casting of Patterned Vascular Networks for Perfusable Engineered Three-Dimensional Tissues, Nature Materials 11(9) (2012) 768.

[99] D.B. Kolesky, R.L. Truby, A.S. Gladman, T.A. Busbee, K.A. Homan, J.A. Lewis, 3D Bioprinting of Vascularized, Heterogeneous Cell-Laden Tissue Constructs, Advanced Materials 26(19) (2014) 3124.

[100] D.B. Kolesky, K.A. Homan, M.A. Skylar-Scott, J.A. Lewis, Three-Dimensional Bioprinting of Thick Vascularized Tissues, Proceedings of the National Academy of Sciences of the United States of America 113(12) (2016) 3179.

[101] K.A. Homan, D.B. Kolesky, M.A. Skylar-Scott, J. Herrmann, H. Obuobi, A. Moisan, J.A. Lewis, Bioprinting of 3D Convoluted Renal Proximal Tubules on Perfusable Chips, Scientific Reports 6 (2016) 34845.

[102] K.A. Homan, N. Gupta, K.T. Kroll, D.B. Kolesky, M. Skylar-Scott, T. Miyoshi, D. Mau, M.T. Valerius, T. Ferrante, J.V. Bonventre, J.A. Lewis, R. Morizane, Flow-Enhanced Vascularization and Maturation of Kidney Organoids in Vitro, Nature Methods 16(3) (2019) 255.

[103] N.Y.C. Lin, K.A. Homan, S.S. Robinson, D.B. Kolesky, N. Duarte, A. Moisan, J.A. Lewis, Renal Reabsorption in 3D Vascularized Proximal Tubule Models, Proceedings of the National Academy of Sciences of the United States of America 116(12) (2019) 5399.

[104] Y. Du, G. Khandekar, J. Llewellyn, W. Polacheck, C.S. Chen, R.G. Wells, A Bile Duct-on-a-Chip with Organ-Level Functions, Hepatology 71(4) (2020) 1350.

[105] T.K. Merceron, M. Burt, Y.J. Seol, H.W. Kang, S.J. Lee, J.J. Yoo, A. Atala, A 3D Bioprinted Complex Structure for Engineering the Muscle-Tendon Unit, Biofabrication 7(3) (2015) 035003.

[106] A.C. Daly, G.M. Cunniffe, B.N. Sathy, O. Jeon, E. Alsberg, D.J. Kelly, 3D Bioprinting of Developmentally Inspired Templates for Whole Bone Organ Engineering, Advanced Healthcare Materials 5(18) (2016) 2353.

[107] B.S. Kim, G. Gao, J.Y. Kim, D.-W. Cho, 3D Cell Printing of Perfusable Vascularized Human Skin Equivalent Composed of Epidermis, Dermis, and Hypodermis for Better Structural Recapitulation of Native Skin, Advanced Healthcare Materials 8(7) (2019) 1801019.

[108] K. Jakab, C. Norotte, B. Damon, F. Marga, A. Neagu, C.L. Besch-Williford, A. Kachurin, K.H. Church, H. Park, V. Mironov, R. Markwald, G. Vunjak-Novakovic, G. Forgacs, Tissue Engineering by Self-Assembly of Cells Printed into Topologically Defined Structures, Tissue Engineering Part A 14(3) (2008) 413.

[109] V. Mironov, R.P. Visconti, V. Kasyanov, G. Forgacs, C.J. Drake, R.R. Markwald, Organ Printing: Tissue Spheroids as Building Blocks, Biomaterials 30(12) (2009) 2164.

[110] K. Jakab, C. Norotte, F. Marga, K. Murphy, G. Vunjak-Novakovic, G. Forgacs, Tissue Engineering by Self-Assembly and Bio-Printing of Living Cells, Biofabrication 2(2) (2010) 022001.

[111] C.M. Owens, F. Marga, G. Forgacs, C.M. Heesch, Biofabrication and Testing of a Fully Cellular Nerve Graft, Biofabrication 5(4) (2013) 045007.

[112] B. Byambaa, N. Annabi, K. Yue, G. Trujillo-de Santiago, M.M. Alvarez, W. Jia, M. Kazemzadeh-Narbat, S.R. Shin, A. Tamayol, A. Khademhosseini, Bioprinted Osteogenic and Vasculogenic Patterns for Engineering 3D Bone Tissue, Advanced Healthcare Materials 6(16) (2017).

[113] Z. Gu, J. Fu, H. Lin, Y. He, Development of 3D Bioprinting: From Printing Methods to Biomedical Applications, Asian Journal of Pharmaceutical Sciences (2019).

[114] Y. Zhang, Y. Yu, I.T. Ozbolat, Direct Bioprinting of Vessel-Like Tubular Microfluidic Channels, Journal of Nanotechnology in Engineering and Medicine 4(2) (2013).

[115] Q. Gao, Y. He, J.Z. Fu, A. Liu, L. Ma, Coaxial Nozzle-Assisted 3D Bioprinting with Built-in Microchannels for Nutrients Delivery, Biomaterials 61 (2015) 203.

[116] W. Jia, P.S. Gungor-Ozkerim, Y.S. Zhang, K. Yue, K. Zhu, W. Liu, Q. Pi, B. Byambaa, M.R. Dokmeci, S.R. Shin, A. Khademhosseini, Direct 3D Bioprinting of Perfusable Vascular Constructs Using a Blend Bioink, Biomaterials 106 (2016) 58.

[117] A.R. Akkineni, T. Ahlfeld, A. Lode, M. Gelinsky, A Versatile Method for Combining Different Biopolymers in a Core/Shell Fashion by 3D Plotting to Achieve Mechanically Robust Constructs, Biofabrication 8(4) (2016) 045001.

[118] H. Cui, W. Zhu, Y. Huang, C. Liu, Z.X. Yu, M. Nowicki, S. Miao, Y. Cheng, X. Zhou, S.J. Lee, Y. Zhou, S. Wang, M. Mohiuddin, K. Horvath, L.G. Zhang, In Vitro and in Vivo Evaluation of 3D Bioprinted Small-Diameter Vasculature with Smooth Muscle and Endothelium, Biofabrication (2019).

[119] L. Shao, Q. Gao, C. Xie, J. Fu, M. Xiang, Y. He, Directly Coaxial 3D Bioprinting of Large-Scale Vascularized Tissue Constructs, Biofabrication 12(3) (2020) 035014.

[120] G. Gao, J.H. Lee, J. Jang, D.H. Lee, J.-S. Kong, B.S. Kim, Y.-J. Choi, W.B. Jang, Y.J. Hong, S.-M. Kwon, D.-W. Cho, Tissue Engineered Bio-Blood-Vessels Constructed Using a Tissue-Specific Bioink and 3D Coaxial Cell Printing Technique: A Novel Therapy for Ischemic Disease, Advanced Functional Materials 27(33) (2017) 1700798.

[121] L. Ouyang, C.B. Highley, W. Sun, J.A. Burdick, A Generalizable Strategy for the 3D Bioprinting of Hydrogels from Nonviscous Photo-Crosslinkable Inks, Advanced Materials 29(8) (2017).

[122] Y. Yu, F. Fu, L. Shang, Y. Cheng, Z. Gu, Y. Zhao, Bioinspired Helical Microfibers from Microfluidics, Advanced Materials 29(18) (2017).

[123] Q. Pi, S. Maharjan, X. Yan, X. Liu, B. Singh, A.M. van Genderen, F. Robledo-Padilla, R. Parra-Saldivar, N. Hu, W. Jia, C. Xu, J. Kang, S. Hassan, H. Cheng, X. Hou, A. Khademhosseini, Y.S. Zhang, Digitally Tunable Microfluidic Bioprinting of Multilayered Cannular Tissues, Advanced Materials 30(43) (2018) e1706913.

[124] L. Shao, Q. Gao, H. Zhao, C. Xie, J. Fu, Z. Liu, M. Xiang, Y. He, Fiber-Based Mini Tissue with Morphology-Controllable Gelma Microfibers, Small 14(44) (2018) e1802187.

[125] A. McCormack, C.B. Highley, N.R. Leslie, F.P.W. Melchels, 3D Printing in Suspension Baths: Keeping the Promises of Bioprinting Afloat, Trends in Biotechnology 38(6) (2020) 584.

[126] W. Wu, A. DeConinck, J.A. Lewis, Omnidirectional Printing of 3D Microvascular Networks, Advanced Materials 23(24) (2011) H178.

[127] T. Bhattacharjee, S.M. Zehnder, K.G. Rowe, S. Jain, R.M. Nixon, W.G. Sawyer, T.E. Angelini, Writing in the Granular Gel Medium, Science Advances 1(8) (2015) e1500655.

[128] A. Lee, A.R. Hudson, D.J. Shiwarski, J.W. Tashman, T.J. Hinton, S. Yerneni, J.M. Bliley, P.G. Campbell, A.W. Feinberg, 3D Bioprinting of Collagen to Rebuild Components of the Human Heart, Science 365(6452) (2019) 482.

[129] T. Bhattacharjee, C.J. Gil, S.L. Marshall, J.M. Urueña, C.S. O'Bryan, M. Carstens, B. Keselowsky, G.D. Palmer, S. Ghivizzani, C.P. Gibbs, W.G. Sawyer, T.E. Angelini, Liquid-Like Solids Support Cells in 3D, ACS Biomaterials Science & Engineering 2(10) (2016) 1787.

[130] C.B. Highley, C.B. Rodell, J.A. Burdick, Direct 3D Printing of Shear-Thinning Hydrogels into Self-Healing Hydrogels, Advanced Materials 27(34) (2015) 5075.

[131] L.H. Han, S. Suri, C.E. Schmidt, S. Chen, Fabrication of Three-Dimensional Scaffolds for Heterogeneous Tissue Engineering, Biomedical Microdevices 12(4) (2010) 721.

[132] S. Suri, L.H. Han, W. Zhang, A. Singh, S. Chen, C.E. Schmidt, Solid Freeform Fabrication of Designer Scaffolds of Hyaluronic Acid for Nerve Tissue Engineering, Biomed Microdevices 13(6) (2011) 983.

[133] R. Gauvin, Y.C. Chen, J.W. Lee, P. Soman, P. Zorlutuna, J.W. Nichol, H. Bae, S. Chen, A. Khademhosseini, Microfabrication of Complex Porous Tissue Engineering Scaffolds Using 3D Projection Stereolithography, Biomaterials 33(15) (2012) 3824.

[134] S.P. Grogan, P.H. Chung, P. Soman, P. Chen, M.K. Lotz, S. Chen, D.D. D'Lima, Digital Micromirror Device Projection Printing System for Meniscus Tissue Engineering, Acta Biomaterialia 9(7) (2013) 7218.

[135] K.C. Hribar, P. Soman, J. Warner, P. Chung, S. Chen, Light-Assisted Direct-Write of 3D Functional Biomaterials, Lab on a Chip 14(2) (2014) 268.

[136] T.Q. Huang, X. Qu, J. Liu, S. Chen, 3D Printing of Biomimetic Microstructures for Cancer Cell Migration, Biomedical Microdevices 16(1) (2014) 127.

[137] X. Ma, X. Qu, W. Zhu, Y.-S. Li, S. Yuan, H. Zhang, J. Liu, P. Wang, C.S.E. Lai, F. Zanella, G.-S. Feng, F. Sheikh, S. Chien, S. Chen, Deterministically Patterned Biomimetic Human Ipsc-Derived Hepatic Model Via Rapid 3D Bioprinting, Proceedings of the National Academy of Sciences of the United States of America 113(8) (2016) 2206.

[138] W. Zhu, X. Ma, M. Gou, D. Mei, K. Zhang, S. Chen, 3D Printing of Functional Biomaterials for Tissue Engineering, Current Opinion in Biotechnology 40 (2016) 103.

[139] X. Ma, C. Yu, P. Wang, W. Xu, X. Wan, C.S.E. Lai, J. Liu, A. Koroleva-Maharajh, S. Chen, Rapid 3D Bioprinting of Decellularized Extracellular Matrix with Regionally Varied Mechanical Properties and Biomimetic Microarchitecture, Biomaterials 185 (2018) 310.

[140] C. Yu, X. Ma, W. Zhu, P. Wang, K.L. Miller, J. Stupin, A. Koroleva-Maharajh, A. Hairabedian, S. Chen, Scanningless and Continuous 3D Bioprinting of Human Tissues with Decellularized Extracellular Matrix, Biomaterials 194 (2019) 1.

[141] J. Liu, J. He, J. Liu, X. Ma, Q. Chen, N. Lawrence, W. Zhu, Y. Xu, S. Chen, Rapid 3D Bioprinting of in Vitro Cardiac Tissue Models Using Human Embryonic Stem Cell-Derived Cardiomyocytes, Bioprinting 13 (2019) e00040.

[142] B. Grigoryan, S.J. Paulsen, D.C. Corbett, D.W. Sazer, C.L. Fortin, A.J. Zaita, P.T. Greenfield, N.J. Calafat, J.P. Gounley, A.H. Ta, F. Johansson, A. Randles, J.E. Rosenkrantz, J.D. Louis-Rosenberg, P.A. Galie, K.R. Stevens, J.S. Miller, Multivascular Networks and Functional Intravascular Topologies within Biocompatible Hydrogels, Science 364(6439) (2019) 458.

[143] K.S. Lim, R. Levato, P.F. Costa, M.D. Castilho, C.R. Alcala-Orozco, K.M.A. van Dorenmalen, F.P.W. Melchels, D. Gawlitta, G.J. Hooper, J. Malda, T.B.F. Woodfield, Bio-Resin for High Resolution Lithography-Based Biofabrication of Complex Cell-Laden Constructs, Biofabrication 10(3) (2018) 034101.

[144] N.A. Chartrain, C.B. Williams, A.R. Whittington, A Review on Fabricating Tissue Scaffolds Using Vat Photopolymerization, Acta Biomaterialia 74 (2018) 90.

[145] C.Y. Liaw, M. Guvendiren, Current and Emerging Applications of 3D Printing in Medicine, Biofabrication 9(2) (2017) 024102.

[146] V. Mironov, V. Kasyanov, R.R. Markwald, Organ Printing: From Bioprinter to Organ Biofabrication Line, Current Opinion in Biotechnology 22(5) (2011) 667.

[147] M.W. Laschke, Y. Harder, M. Amon, I. Martin, J. Farhadi, A. Ring, N. Torio-Padron, R. Schramm, M. Rücker, D. Junker, J.M. Häufel, C. Carvalho, M. Heberer, G. Germann, B. Vollmar, M.D. Menger, Angiogenesis in Tissue Engineering: Breathing Life into Constructed Tissue Substitutes, Tissue Engineering 12(8) (2006) 2093.

[148] J.P. Stegemann, S.N. Kaszuba, S.L. Rowe, Review: Advances in Vascular Tissue Engineering Using Protein-Based Biomaterials, Tissue Engineering 13(11) (2007) 2601.

[149] R.K. Jain, P. Au, J. Tam, D.G. Duda, D. Fukumura, Engineering Vascularized Tissue, Nature Biotechnology 23 (2005) 821.

[150] C.-Y. Liaw, S. Ji, M. Guvendiren, Engineering 3D Hydrogels for Personalized in Vitro Human Tissue Models, Advanced Healthcare Materials 7(4) (2018) 1701165.

[151] D.G. Seifu, K. Mequanint, Fabrication of Vascular Tissue Engineering Scaffolds with Enhanced Oxygen Diffusivity and Cell Infiltration, Journal of Biomaterials and Tissue Engineering 2(4) (2012) 280.

[152] A.J. Melchiorri, N. Hibino, Z.R. Brandes, R.A. Jonas, J.P. Fisher, Development and Assessment of a Biodegradable Solvent Cast Polyester Fabric Small-Diameter Vascular Graft, Journal of Biomedical Materials Research Part A 102(6) (2013) 1972.

[153] S.C. Baker, G. Rohman, J. Hinley, J. Stahlschmidt, N.R. Cameron, J. Southgate, Cellular Integration and Vascularisation Promoted by a Resorbable, Particulate-Leached, Cross-Linked Poly(E-Caprolactone) Scaffold, Macromolecular Bioscience 11(5) (2011) 618.

[154] W. Thein-Han, H.H.K. Xu, Prevascularization of a Gas-Foaming Macroporous Calcium Phosphate Cement Scaffold Via Coculture of Human Umbilical Vein Endothelial Cells and Osteoblasts, Tissue Engineering Part A 19(15-16) (2013) 1675.

[155] S. Singh, B.M. Wu, J.C. Dunn, The Enhancement of Vegf-Mediated Angiogenesis by Polycaprolactone Scaffolds with Surface Cross-Linked Heparin, Biomaterials 32(8) (2011) 2059.

[156] H.-Y. Mi, X. Jing, J. McNulty, M.R. Salick, X.-F. Peng, L.-S. Turng, Approaches to Fabricating Multiple-Layered Vascular Scaffolds Using Hybrid Electrospinning and Thermally Induced Phase Separation Methods, Industrial & Engineering Chemistry Research 55(4) (2016) 882.

[157] I.S. Park, S.-H. Kim, Y.H. Kim, I.H. Kim, S.H. Kim, A Collagen/Smooth Muscle Cell-Incorporated Elastic Scaffold for Tissue-Engineered Vascular Grafts, Journal of Biomaterials Science, Polymer Edition 20(11) (2009) 1645.

[158] A. Hasan, A. Memic, N. Annabi, M. Hossain, A. Paul, M.R. Dokmeci, F. Dehghani, A. Khademhosseini, Electrospun Scaffolds for Tissue Engineering of Vascular Grafts, Acta Biomaterialia 10(1) (2014) 11.

[159] R. Gauvin, T. Ahsan, D. Larouche, P. Lévesque, J. Dubé, F.A. Auger, R.M. Nerem, L. Germain, A Novel Single-Step Self-Assembly Approach for the Fabrication of Tissue-Engineered Vascular Constructs, Tissue Engineering Part A 16(5) (2009) 1737.

[160] K.S. Toohey, N.R. Sottos, J.A. Lewis, J.S. Moore, S.R. White, Self-Healing Materials with Microvascular Networks, Nature Materials 6(8) (2007) 581.

[161] P. Datta, B. Ayan, I.T. Ozbolat, Bioprinting for Vascular and Vascularized Tissue Biofabrication, Acta Biomaterialia 51 (2017) 1.

[162] L.E. Bertassoni, M. Cecconi, V. Manoharan, M. Nikkhah, J. Hjortnaes, A.L. Cristino, G. Barabaschi, D. Demarchi, M.R. Dokmeci, Y. Yang, A. Khademhosseini, Hydrogel Bioprinted Microchannel Networks for Vascularization of Tissue Engineering Constructs, Lab on a Chip 14(13) (2014) 2202.

[163] V.K. Lee, D.Y. Kim, H. Ngo, Y. Lee, L. Seo, S.-S. Yoo, P.A. Vincent, G. Dai, Creating Perfused Functional Vascular Channels Using 3D Bio-Printing Technology, Biomaterials 35(28) (2014) 8092.

[164] V.K. Lee, A.M. Lanzi, N. Haygan, S.S. Yoo, P.A. Vincent, G. Dai, Generation of Multi-Scale Vascular Network System within 3D Hydrogel Using 3D Bio-Printing Technology, Cellular and Molecular Bioengineering 7(3) (2014) 460.

[165] L. Ouyang, C.B. Highley, C.B. Rodell, W. Sun, J.A. Burdick, 3D Printing of Shear-Thinning Hyaluronic Acid Hydrogels with Secondary Cross-Linking, ACS Biomaterials Science & Engineering 2(10) (2016) 1743.

[166] K.H. Song, C.B. Highley, A. Rouff, J.A. Burdick, Complex 3D-Printed Microchannels within Cell-Degradable Hydrogels, Advanced Functional Materials (2018) 1801331.

[167] T.E. Angelini, B.S. Sumerlin, C.S. O'Bryan, W. Gregory Sawyer, T. Bhattacharjee, Organic Microgel System for 3D Printing of Silicone Structures, 2016, .

[168] C.S. O'Bryan, T. Bhattacharjee, S. Hart, C.P. Kabb, K.D. Schulze, I. Chilakala, B.S. Sumerlin, W.G. Sawyer, T.E. Angelini, Self-Assembled Micro-Organogels for 3D Printing Silicone Structures, Science Advances 3(5) (2017).

[169] W. Wu, A. DeConinck, A. Lewis Jennifer, Omnidirectional Printing of 3D Microvascular Networks, Advanced Materials 23(24) (2011) H178.

[170] T. Grix, A. Ruppelt, A. Thomas, A.K. Amler, B.P. Noichl, R. Lauster, L. Kloke, Bioprinting Perfusion-Enabled Liver Equivalents for Advanced Organ-on-a-Chip Applications, Genes (Basel) 9(4) (2018).

[171] R. Raman, B. Bhaduri, M. Mir, A. Shkumatov, M.K. Lee, G. Popescu, H. Kong, R. Bashir, High-Resolution Projection Microstereolithography for Patterning of Neovasculature, Advanced Healthcare Materials 5(5) (2016) 610.

[172] K. Arcaute, B.K. Mann, R.B. Wicker, Stereolithography of Three-Dimensional Bioactive Poly(Ethylene Glycol) Constructs with Encapsulated Cells, Annals of Biomedical Engineering 34(9) (2006) 1429.

[173] S. Khetan, M. Guvendiren, W.R. Legant, D.M. Cohen, C.S. Chen, J.A. Burdick, Degradation-Mediated Cellular Traction Directs Stem Cell Fate in Covalently Crosslinked Three-Dimensional Hydrogels, Nature Materials 12(5) (2013) 458.

[174] M. Guvendiren, J.A. Burdick, Stiffening Hydrogels to Probe Short- and Long-Term Cellular Responses to Dynamic Mechanics, Nature Communications 3 (2012) 792.

[175] B.D. Fairbanks, M.P. Schwartz, C.N. Bowman, K.S. Anseth, Photoinitiated Polymerization of Peg-Diacrylate with Lithium Phenyl-2,4,6-Trimethylbenzoylphosphinate: Polymerization Rate and Cytocompatibility, Biomaterials 30(35) (2009) 6702.

[176] M. Guvendiren, S. Yang, J.A. Burdick, Swelling-Induced Surface Patterns in Hydrogels with Gradient Crosslinking Density, Advanced Functional Materials 19(19) (2009) 3038.

[177] J. Park, S.J. Lee, S. Chung, J.H. Lee, W.D. Kim, J.Y. Lee, S.A. Park, Cell-Laden 3D Bioprinting Hydrogel Matrix Depending on Different Compositions for Soft Tissue Engineering: Characterization and Evaluation, Materials Science and Engineering: C (2016).

[178] L. Archer, 3D Printing with Living Inks, Science 358(6367) (2017) 1143.

[179] X. Ma, J. Liu, W. Zhu, M. Tang, N. Lawrence, C. Yu, M. Gou, S. Chen, 3D Bioprinting of Functional Tissue Models for Personalized Drug Screening and in Vitro Disease Modeling, Advanced Drug Delivery Reviews 132 (2018) 235.

[180] J. Jang, H.-G. Yi, D.-W. Cho, 3D Printed Tissue Models: Present and Future, ACS Biomaterials Science & Engineering 2(10) (2016) 1722.

[181] L.M. Norona, D.G. Nguyen, D.A. Gerber, S.C. Presnell, M. Mosedale, P.B. Watkins, Bioprinted Liver Provides Early Insight into the Role of Kupffer Cells in Tgf-B1 and Methotrexate-Induced Fibrogenesis, PLOS ONE 14(1) (2019) e0208958.

[182] M. Albanna, K.W. Binder, S.V. Murphy, J. Kim, S.A. Qasem, W. Zhao, J. Tan, I.B. El-Amin, D.D. Dice, J. Marco, J. Green, T. Xu, A. Skardal, J.H. Holmes, J.D. Jackson, A. Atala, J.J. Yoo, In Situ Bioprinting of Autologous Skin Cells Accelerates Wound Healing of Extensive Excisional Full-Thickness Wounds, Scientific Reports 9(1) (2019) 1856.

[183] N. Ashammakhi, S. Ahadian, I. Pountos, S.-K. Hu, N. Tellisi, P. Bandaru, S. Ostrovidov, M.R. Dokmeci, A. Khademhosseini, In Situ Three-Dimensional Printing for Reparative and Regenerative Therapy, Biomedical Microdevices 21(2) (2019) 42.

[184] V. Keriquel, H. Oliveira, M. Rémy, S. Ziane, S. Delmond, B. Rousseau, S. Rey, S. Catros, J. Amédée, F. Guillemot, J.-C. Fricain, In Situ Printing of Mesenchymal Stromal Cells, by Laser-Assisted Bioprinting, for in Vivo Bone Regeneration Applications, Scientific Reports 7(1) (2017) 1778.

[185] T.I. Ozbolat, K.K. Moncal, H. Gudapati, Evaluation of Bioprinter Technologies, Additive Manufacturing (2016).

[186] S. Ji, M. Guvendiren, Recent Advances in Bioink Design for 3D Bioprinting of Tissues and Organs, Frontiers in Bioengineering and Biotechnology 5 (2017) 23.

[187] K. Dubbin, A. Tabet, S.C. Heilshorn, Quantitative Criteria to Benchmark New and Existing Bio-Inks for Cell Compatibility, Biofabrication 9(4) (2017) 044102.

[188] K. Holzl, S. Lin, L. Tytgat, S. Van Vlierberghe, L. Gu, A. Ovsianikov, Bioink Properties before, During and after 3D Bioprinting, Biofabrication 8(3) (2016) 032002.

[189] D. Chimene, K.K. Lennox, R.R. Kaunas, A.K. Gaharwar, Advanced Bioinks for 3D Printing: A Materials Science Perspective, Annals of Biomedical Engineering 44(6) (2016) 2090.

[190] D.B. Kolesky, K.A. Homan, M.A. Skylar-Scott, J.A. Lewis, Three-Dimensional Bioprinting of Thick Vascularized Tissues, Proceedings of the National Academy of Sciences 113(12) (2016) 3179.

[191] D.B. Kolesky, R.L. Truby, A.S. Gladman, T.A. Busbee, K.A. Homan, J.A. Lewis, 3D Bioprinting of Vascularized, Heterogeneous Cell-Laden Tissue Constructs, Advanced Materials 26(19) (2014) 3124.

[192] A.L. Rutz, K.E. Hyland, A.E. Jakus, W.R. Burghardt, R.N. Shah, A Multimaterial Bioink Method for 3D Printing Tunable, Cell-Compatible Hydrogels, Advanced Materials 27(9) (2015) 1607.

[193] C. Colosi, S.R. Shin, V. Manoharan, S. Massa, M. Costantini, A. Barbetta, M.R. Dokmeci, M. Dentini, A. Khademhosseini, Microfluidic Bioprinting of Heterogeneous 3D Tissue Constructs Using Low-Viscosity Bioink, Advanced Materials 28(4) (2016) 677.

[194] K.S. Lim, B.S. Schon, N.V. Mekhileri, G.C.J. Brown, C.M. Chia, S. Prabakar, G.J. Hooper, T.B.F. Woodfield, New Visible-Light Photoinitiating System for Improved Print Fidelity in Gelatin-Based Bioinks, ACS Biomaterials Science & Engineering 2(10) (2016) 1752.

[195] J. Yin, M. Yan, Y. Wang, J. Fu, H. Suo, 3D Bioprinting of Low-Concentration Cell-Laden Gelatin Methacrylate (Gelma) Bioinks with a Two-Step Cross-Linking Strategy, ACS Applied Materials & Interfaces 10(8) (2018) 6849.

[196] S. Ji, E. Almeida, M. Guvendiren, 3D Bioprinting of Complex Channels within Cell-Laden Hydrogels, Acta Biomaterialiaialia (2019).

[197] S. Khalil, W. Sun, Bioprinting Endothelial Cells with Alginate for 3D Tissue Constructs, Journal of Biomechanical Engineering 131(11) (2009).

[198] H. Yi, L.-Q. Wu, W.E. Bentley, R. Ghodssi, G.W. Rubloff, J.N. Culver, G.F. Payne, Biofabrication with Chitosan, Biomacromolecules 6(6) (2005) 2881.

[199] K.K. Moncal, V. Ozbolat, P. Datta, D.N. Heo, I.T. Ozbolat, Thermally-Controlled Extrusion-Based Bioprinting of Collagen, Journal of Materials Science: Materials in Medicine 30(5) (2019) 55.

[200] S. Rhee, J.L. Puetzer, B.N. Mason, C.A. Reinhart-King, L.J. Bonassar, 3D Bioprinting of Spatially Heterogeneous Collagen Constructs for Cartilage Tissue Engineering, ACS Biomaterials Science & Engineering 2(10) (2016) 1800.

[201] C. Lee, E. Abelseth, L. de la Vega, S.M. Willerth, Bioprinting a Novel Glioblastoma Tumor Model Using a Fibrin-Based Bioink for Drug Screening, Materials Today Chemistry 12 (2019) 78.

[202] Z. Zheng, J. Wu, M. Liu, H. Wang, C. Li, M.J. Rodriguez, G. Li, X. Wang, D.L. Kaplan, 3D Bioprinting of Self-Standing Silk-Based Bioink, Advanced Healthcare Materials 7(6) (2018) 1701026.

[203] S. Chawla, S. Midha, A. Sharma, S. Ghosh, Silk-Based Bioinks for 3D Bioprinting, Advanced Healthcare Materials 7(8) (2018) 1701204.

[204] J. Jang, T.G. Kim, B.S. Kim, S.-W. Kim, S.-M. Kwon, D.-W. Cho, Tailoring Mechanical Properties of Decellularized Extracellular Matrix Bioink by Vitamin B2-Induced Photo-Crosslinking, Acta Biomaterialiaialia 33 (2016) 88.

[205] J. Jang, H.-J. Park, S.-W. Kim, H. Kim, J.Y. Park, S.J. Na, H.J. Kim, M.N. Park, S.H. Choi, S.H. Park, S.W. Kim, S.-M. Kwon, P.-J. Kim, D.-W. Cho, 3D Printed Complex Tissue Construct Using Stem Cell-Laden Decellularized Extracellular Matrix Bioinks for Cardiac Repair, Biomaterials 112 (2017) 264.

[206] M. Kesti, M. Muller, J. Becher, M. Schnabelrauch, M. D'Este, D. Eglin, M. Zenobi-Wong, A Versatile Bioink for Three-Dimensional Printing of Cellular Scaffolds Based on Thermally and Photo-Triggered Tandem Gelation, Acta Biomaterialia 11 (2015) 162.

[207] L.E. Bertassoni, C. J.C., V. Manoharan, A.L. Cristino, N.S. Bhise, W.A. Araujo, P. Zorlutuna, N.E. Vrana, A.M. Ghaemmaghami, M.R. Dokmeci, A. Khademhosseini, Direct-Write Bioprinting of Cell-Laden Methacrylated Gelatin Hydrogels, Biofabrication 6(2) (2014) 024105.

[208] W. Liu, M.A. Heinrich, Y. Zhou, A. Akpek, N. Hu, X. Liu, X. Guan, Z. Zhong, X. Jin, A. Khademhosseini, Y.S. Zhang, Extrusion Bioprinting of Shear-Thinning Gelatin Methacryloyl Bioinks, Advanced Healthcare Materials 6(12) (2017) 10.1002/adhm.201601451.

[209] J. Schurz, A Bright Future for Cellulose, Progress in Polymer Science 24(4) (1999) 481.

[210] C. Chang, L. Zhang, Cellulose-Based Hydrogels: Present Status and Application Prospects, Carbohydrate Polymers 84(1) (2011) 40.

[211] D. Klemm, B. Heublein, H.P. Fink, A. Bohn, Cellulose: Fascinating Biopolymer and Sustainable Raw Material, Angewandte Chemie International Edition 44(22) (2005) 3358.

[212] T. McOscar, Renewable Hydrogels from Norbornene-Functionalized Carboxymethyl Cellulose and a Short Dithiol Crosslinked Via a Thiol-Ene Reaction, Electronic Theses and Dissertations 2761 (2017).

[213] A.S. Gladman, E.A. Matsumoto, R.G. Nuzzo, L. Mahadevan, J.A. Lewis, Biomimetic 4D Printing, Nature Materials 15(4) (2016) 413.

[214] Q. Wang, J. Sun, Q. Yao, C. Ji, J. Liu, Q. Zhu, 3D Printing with Cellulose Materials, Cellulose 25(8) (2018) 4275.

[215] A. Cataldi, D. Rigotti, V.D.H. Nguyen, A. Pegoretti, Polyvinyl Alcohol Reinforced with Crystalline Nanocellulose for 3D Printing Application, Materials Today Communications 15 (2018) 236.

[216] L. Li, Y. Zhu, J. Yang, 3D Bioprinting of Cellulose with Controlled Porous Structures from Nmmo, Materials Letters 210 (2018) 136.

[217] H. Martínez Ávila, S. Schwarz, N. Rotter, P. Gatenholm, 3D Bioprinting of Human Chondrocyte-Laden Nanocellulose Hydrogels for Patient-Specific Auricular Cartilage Regeneration, Bioprinting 1-2 (2016) 22.

[218] I. Henriksson, P. Gatenholm, D.A. Hägg, Increased Lipid Accumulation and Adipogenic Gene Expression of Adipocytes in 3D Bioprinted Nanocellulose Scaffolds, Biofabrication 9(1) (2017) 015022.

[219] K.M.O. Håkansson, I.C. Henriksson, C. de la Peña Vázquez, V. Kuzmenko, K. Markstedt, P. Enoksson, P. Gatenholm, Solidification of 3D Printed Nanofibril Hydrogels into Functional 3D Cellulose Structures, Advanced Materials Technologies 1(7) (2016) 1600096.

[220] M. Müller, E. Öztürk, Ø. Arlov, P. Gatenholm, M. Zenobi-Wong, Alginate Sulfate–Nanocellulose Bioinks for Cartilage Bioprinting Applications, Annals of Biomedical Engineering 45(1) (2017) 210.

[221] D. Nguyen, D.A. Hägg, A. Forsman, J. Ekholm, P. Nimkingratana, C. Brantsing, T. Kalogeropoulos, S. Zaunz, S. Concaro, M. Brittberg, A. Lindahl, P. Gatenholm, A. Enejder, S. Simonsson, Cartilage Tissue Engineering by the 3D Bioprinting of Ips Cells in a Nanocellulose/Alginate Bioink, Scientific Reports 7(1) (2017) 658.

[222] K. Schütz, A.-M. Placht, B. Paul, S. Brüggemeier, M. Gelinsky, A. Lode, Three-Dimensional Plotting of a Cell-Laden Alginate/Methylcellulose Blend: Towards Biofabrication of Tissue Engineering Constructs with Clinically Relevant Dimensions, Journal of Tissue Engineering and Regenerative Medicine 11(5) (2017) 1574.

[223] K. Markstedt, A. Mantas, I. Tournier, H. Martinez Avila, D. Hagg, P. Gatenholm, 3D Bioprinting Human Chondrocytes with Nanocellulose-Alginate Bioink for Cartilage Tissue Engineering Applications, Biomacromolecules 16(5) (2015) 1489.

[224] K. Markstedt, A. Escalante, G. Toriz, P. Gatenholm, Biomimetic Inks Based on Cellulose Nanofibrils and Cross-Linkable Xylans for 3D Printing, ACS Applied Materials & Interfaces 9(46) (2017) 40878.

[225] N. Contessi Negrini, L. Bonetti, L. Contili, S. Farè, 3D Printing of Methylcellulose-Based Hydrogels, Bioprinting 10 (2018) e00024.

[226] H. Li, Y.J. Tan, K.F. Leong, L. Li, 3D Bioprinting of Highly Thixotropic Alginate/Methylcellulose Hydrogel with Strong Interface Bonding, ACS Applied Materials & Interfaces 9(23) (2017) 20086.

[227] C.E. Hoyle, C.N. Bowman, Thiol-Ene Click Chemistry, Angewandte Chemie International Edition 49(9) (2010) 1540.

[228] S.K. Reddy, N.B. Cramer, C.N. Bowman, Thiol−Vinyl Mechanisms. 2. Kinetic Modeling of Ternary Thiol−Vinyl Photopolymerizations, Macromolecules 39(10) (2006) 3681.

[229] B.D. Fairbanks, M.P. Schwartz, A.E. Halevi, C.R. Nuttelman, C.N. Bowman, K.S. Anseth, A Versatile Synthetic Extracellular Matrix Mimic Via Thiol-Norbornene Photopolymerization, Advanced Materials 21(48) (2009) 5005.

[230] W.M. Gramlich, I.L. Kim, J.A. Burdick, Synthesis and Orthogonal Photopatterning of Hyaluronic Acid Hydrogels with Thiol-Norbornene Chemistry, Biomaterials 34(38) (2013) 9803.

[231] H.W. Ooi, C. Mota, A.T. Ten Cate, A. Calore, L. Moroni, M.B. Baker, Thiol-Ene Alginate Hydrogels as Versatile Bioinks for Bioprinting, Biomacromolecules 19(8) (2018) 3390.

[232] K.H. Song, C.B. Highley, A. Rouff, J.A. Burdick, Complex 3D-Printed Microchannels within Cell-Degradable Hydrogels, Advanced Functional Materials 28(31) (2018) 1801331.

[233] Z. Mũnoz, H. Shih, C.-C. Lin, Gelatin Hydrogels Formed by Orthogonal Thiol–Norbornene Photochemistry for Cell Encapsulation, Biomaterials Science 2(8) (2014) 1063.

[234] H.D. Nguyen, H.-Y. Liu, B.N. Hudson, C.-C. Lin, Enzymatic Cross-Linking of Dynamic Thiol-Norbornene Click Hydrogels, ACS Biomaterials Science & Engineering 5(3) (2019) 1247.

[235] Z. Jiang, R. Shaha, K. Jiang, R. McBride, C. Frick, J. Oakey, Composite Hydrogels with Controlled Degradation in 3D Printed Scaffolds, IEEE Trans Nanobioscience 18(2) (2019) 261.

[236] T.V.C. McOscar, W.M. Gramlich, Hydrogels from Norbornene-Functionalized Carboxymethyl Cellulose Using a Uv-Initiated Thiol-Ene Click Reaction, Cellulose 25(11) (2018) 6531.

[237] N. Dadoo, S.B. Landry, J.D. Bomar, W.M. Gramlich, Synthesis and Spatiotemporal Modification of Biocompatible and Stimuli-Responsive Carboxymethyl Cellulose Hydrogels Using Thiol-Norbornene Chemistry, Macromolecular Bioscience 17(9) (2017).

[238] C.-Y. Liaw, M. Guvendiren, Current and Emerging Applications of 3D Printing in Medicine, Biofabrication 9(2) (2017) 024102.

[239] T. Billiet, M. Vandenhaute, J. Schelfhout, S. Van Vlierberghe, P. Dubruel, A Review of Trends and Limitations in Hydrogel-Rapid Prototyping for Tissue Engineering, Biomaterials 33(26) (2012) 6020.

[240] N.E. Fedorovich, J. Alblas, W.E. Hennink, F.C. Oner, W.J.A. Dhert, Organ Printing: The Future of Bone Regeneration?, Trends in Biotechnology 29(12) (2011) 601.

[241] F. Marga, K. Jakab, C. Khatiwala, B. Shepherd, S. Dorfman, B. Hubbard, S. Colbert, F. Gabor, Toward Engineering Functional Organ Modules by Additive Manufacturing, Biofabrication 4(2) (2012).

[242] I.T. Ozbolat, Y. Yu, Bioprinting toward Organ Fabrication: Challenges and Future Trends, Ieee Transactions on Biomedical Engineering 60(3) (2013) 691.

[243] S.M. Peltola, F.P.W. Melchels, D.W. Grijpma, M. Kellomaki, A Review of Rapid Prototyping Techniques for Tissue Engineering Purposes, Annals of Medicine 40(4) (2008) 268.

[244] W. Sun, A. Darling, B. Starly, J. Nam, Computer-Aided Tissue Engineering: Overview, Scope and Challenges, Biotechnology and Applied Biochemistry 39 (2004) 29.

[245] S.J. Hollister, Porous Scaffold Design for Tissue Engineering, Nature Materials 4(7) (2005) 518.

[246] D.W. Hutmacher, Scaffold Design and Fabrication Technologies for Engineering Tissues - State of the Art and Future Perspectives, Journal of Biomaterials Science-Polymer Edition 12(1) (2001) 107.

[247] V. Karageorgiou, D. Kaplan, Porosity of 3D Biomaterial Scaffolds and Osteogenesis, Biomaterials 26(27) (2005) 5474.

[248] J.S. Miller, K.R. Stevens, M.T. Yang, B.M. Baker, D.-H.T. Nguyen, D.M. Cohen, E. Toro, A.A. Chen, P.A. Galie, X. Yu, R. Chaturvedi, S.N. Bhatia, C.S. Chen, Rapid Casting of Patterned Vascular Networks for Perfusable Engineered Three-Dimensional Tissues, Nature Materials 11(9) (2012) 768.

[249] S.F. Badylak, D.J. Weiss, A. Caplan, P. Macchiarini, Engineered Whole Organs and Complex Tissues, Lancet 379(9819) (2012) 943.

[250] J. Parthasarathy, 3D Modeling, Custom Implants and Its Future Perspectives in Craniofacial Surgery, Annals of Maxillofacial Surgery 4(1) (2014) 9.

[251] D.A. Zopf, S.J. Hollister, M.E. Nelson, R.G. Ohye, G.E. Green, Bioresorbable Airway Splint Created with a Three-Dimensional Printer, New England Journal of Medicine 368(21) (2013) 2043.

[252] M.A. Woodruff, D.W. Hutmacher, The Return of a Forgotten Polymer—Polycaprolactone in the 21st Century, Progress in Polymer Science 35(10) (2010) 1217.

[253] T. Serra, J.A. Planell, M. Navarro, High-Resolution Pla-Based Composite Scaffolds Via 3-D Printing Technology, Acta Biomaterialiaialia 9(3) (2013) 5521.

[254] A. Feinberg, T. Hinton, Additive Manufacturing of Embedded Materials, Carnegie-Mellon University, USA, 2016, .

[255] B. Highley Christopher, B. Rodell Christopher, A. Burdick Jason, Direct 3D Printing of Shear‐Thinning Hydrogels into Self‐Healing Hydrogels, Advanced Materials 27(34) (2015) 5075.

[256] T.J. Hinton, A. Hudson, K. Pusch, A. Lee, A.W. Feinberg, 3D Printing Pdms Elastomer in a Hydrophilic Support Bath Via Freeform Reversible Embedding, ACS Biomaterials Science & Engineering 2(10) (2016) 1781.

[257] S.R. Govindarajan, Y. Xu, J.P. Swanson, T. Jain, Y. Lu, J.-W. Choi, A. Joy, A Solvent and Initiator Free, Low-Modulus, Degradable Polyester Platform with Modular Functionality for Ambient-Temperature 3D Printing, Macromolecules 49(7) (2016) 2429.

[258] Y. Yi-Cheun, B.H. Christopher, O. Liliang, A.B. Jason, 3D Printing of Photocurable Poly(Glycerol Sebacate) Elastomers, Biofabrication 8(4) (2016) 045004.

[259] A.L. Rutz, K.E. Hyland, A.E. Jakus, W.R. Burghardt, R.N. Shah, A Multimaterial Bioink Method for 3D Printing Tunable, Cell-Compatible Hydrogels, Advanced Materials 27(9) (2015) 1607.

[260] M.E. Mackay, Z.R. Swain, C.R. Banbury, D.D. Phan, D.A. Edwards, The Performance of the Hot End in a Plasticating 3D Printer, Journal of Rheology 61(2) (2017) 229.

[261] R. Anitha, S. Arunachalam, P. Radhakrishnan, Critical Parameters Influencing the Quality of Prototypes in Fused Deposition Modelling, Journal of Materials Processing Technology 118(1) (2001) 385.

[262] I. Engelberg, J. Kohn, Physicomechanical Properties of Degradable Polymers Used in Medical Applications - a Comparative-Study, Biomaterials 12(3) (1991) 292.

[263] L.E. Freed, G. Vunjaknovakovic, R.J. Biron, D.B. Eagles, D.C. Lesnoy, S.K. Barlow, R. Langer, Biodegradable Polymer Scaffolds for Tissue Engineering, Bio-Technology 12(7) (1994) 689.

[264] N. Huebsch, D.J. Mooney, Inspiration and Application in the Evolution of Biomaterials, Nature 462(7272) (2009) 426.

[265] S. Mitragotri, J. Lahann, Physical Approaches to Biomaterial Design, Nature Materials 8(1) (2009) 15.

[266] A.J. Mieszawska, D.L. Kaplan, Smart Biomaterials - Regulating Cell Behavior through Signaling Molecules, BMC Biology 8 (2010) 59.

[267] J. Kohn, New Approaches to Biomaterials Design, Nature Materials 3(11) (2004) 745.

[268] S. Ravi, E.L. Chaikof, Biomaterials for Vascular Tissue Engineering, Regenerative Medicine 5(1) (2009) 107.

[269] Y. Kimura, K. Shirotani, H. Yamane, T. Kitao, Ring-Opening Polymerization of 3(S)-[(Benzyloxycarbonyl)Methyl]-1,4-Dioxane-2,5-Dione: A New Route to a Poly(.Alpha.-Hydroxy Acid) with Pendant Carboxyl Groups, Macromolecules 21(11) (1988) 3338.

[270] M. Trollsås, V.Y. Lee, D. Mecerreyes, P. Löwenhielm, M. Möller, R.D. Miller, J.L. Hedrick, Hydrophilic Aliphatic Polyesters: Design, Synthesis, and Ring-Opening Polymerization of Functional Cyclic Esters, Macromolecules 33(13) (2000) 4619.

[271] D. Tian, P. Dubois, R. Jérôme, Macromolecular Engineering of Polylactones and Polylactides. 22. Copolymerization of E-Caprolactone and 1,4,8-Trioxaspiro[4.6]-9-Undecanone Initiated by Aluminum Isopropoxide, Macromolecules 30(9) (1997) 2575.

[272] B.J. Adzima, Y. Tao, C.J. Kloxin, C.A. DeForest, K.S. Anseth, C.N. Bowman, Spatial and Temporal Control of the Alkyne–Azide Cycloaddition by Photoinitiated Cu(Ii) Reduction, Nature Chemistry 3 (2011) 256.

[273] D.A. Ossipov, J. Hilborn, Poly(Vinyl Alcohol)-Based Hydrogels Formed by "Click Chemistry", Macromolecules 39(5) (2006) 1709.

[274] C.A. DeForest, K.S. Anseth, Cytocompatible Click-Based Hydrogels with Dynamically-Tunable Properties through Orthogonal Photoconjugation and Photocleavage Reactions, Nature Chemistry 3(12) (2011) 925.

[275] A.J. Link, D.A. Tirrell, Cell Surface Labeling of Escherichia Coli Via Copper(I)-Catalyzed [3+2] Cycloaddition, Journal of the American Chemical Society 125(37) (2003) 11164.

[276] A.E. Speers, G.C. Adam, B.F. Cravatt, Activity-Based Protein Profiling in Vivo Using a Copper(I)-Catalyzed Azide-Alkyne [3 + 2] Cycloaddition, Journal of the American Chemical Society 125(16) (2003) 4686.

[277] S.I. Ertel, J. Kohn, Evaluation of a Series of Tyrosine-Derived Polycarbonates as Degradable Biomaterials, Journal of Biomedical Materials Research 28(8) (1994) 919.

[278] S.D. Sommerfeld, Z. Zhang, M.C. Costache, S.L. Vega, J. Kohn, Enzymatic Surface Erosion of High Tensile Strength Polycarbonates Based on Natural Phenols, Biomacromolecules 15(3) (2014) 830.

[279] V. Tangpasuthadol, S.M. Pendharkar, J. Kohn, Hydrolytic Degradation of Tyrosine-Derived Polycarbonates, a Class of New Biomaterials. Part I: Study of Model Compounds, Biomaterials 21(23) (2000) 2371.

[280] S.L. Bourke, J. Kohn, Polymers Derived from the Amino Acid L-Tyrosine: Polycarbonates, Polyarylates and Copolymers with Poly(Ethylene Glycol), Advanced Drug Delivery Reviews 55(4) (2003) 447.

[281] D. Lewitus, K.L. Smith, W. Shain, J. Kohn, Ultrafast Resorbing Polymers for Use as Carriers for Cortical Neural Probes, Acta Biomaterialiaialia 7(6) (2011) 2483.

[282] G. Papadopoulos, D. Boskou, Antioxidant Effect of Natural Phenols on Olive Oil, Journal of the American Oil Chemists' Society 68(9) (1991) 669.

[283] I. Aissa, M. Bouaziz, F. Frikha, R.B. Mansour, Y. Gargouri, Synthesized Tyrosyl Hydroxyphenylacetate, a Novel Antioxidant, Anti-Stress and Antibacterial Compound, Process Biochemistry 47(12) (2012) 2356.

[284] M. Ruel, R.J. Laham, J.A. Parker, M.J. Post, J.A. Ware, M. Simons, F.W. Sellke, Long-Term Effects of Surgical Angiogenic Therapy with Fibroblast Growth Factor 2 Protein, The Journal of Thoracic and Cardiovascular Surgery 124(1) (2002) 28.

[285] O. Jeon, S.J. Song, S.-W. Kang, A.J. Putnam, B.-S. Kim, Enhancement of Ectopic Bone Formation by Bone Morphogenetic Protein-2 Released from a Heparin-Conjugated Poly (L-Lactic-Co-Glycolic Acid) Scaffold, Biomaterials 28(17) (2007) 2763.

[286] D.G. Belair, N.N. Le, W.L. Murphy, Design of Growth Factor Sequestering Biomaterials, Chemical communications (Cambridge, England) 50(99) (2014) 15651.

[287] S.F. van Dongen, R.L. Teeuwen, M. Nallani, S.S. van Berkel, J.J. Cornelissen, R.J. Nolte, J.C. van Hest, Single-Step Azide Introduction in Proteins Via an Aqueous Diazo Transfer, Bioconjugate Chemistry 20(1) (2008) 20.

[288] M. Guvendiren, D.A. Brass, P.B. Messersmith, K.R. Shull, Adhesion of Dopa-Functionalized Model Membranes to Hard and Soft Surfaces, The Journal of Adhesion 85(9) (2009) 631.

[289] Z. Sheikh, S. Najeeb, Z. Khurshid, V. Verma, H. Rashid, M. Glogauer, Biodegradable Materials for Bone Repair and Tissue Engineering Applications, Materials 8(9) (2015) 5744.

[290] S. Slavin, J. Burns, D.M. Haddleton, C.R. Becer, Synthesis of Glycopolymers Via Click Reactions, European Polymer Journal 47(4) (2011) 435.

[291] D. Tang, R.S. Tare, L.Y. Yang, D.F. Williams, K.L. Ou, R.O. Oreffo, Biofabrication of Bone Tissue: Approaches, Challenges and Translation for Bone Regeneration, Biomaterials 83 (2016) 363.

[292] A. Oryan, S. Alidadi, A. Moshiri, N. Maffulli, Bone Regenerative Medicine: Classic Options, Novel Strategies, and Future Directions, Journal of Orthopaedic Surgery and Research 9(1) (2014) 18.

[293] S. Bose, M. Roy, A. Bandyopadhyay, Recent Advances in Bone Tissue Engineering Scaffolds, Trends in Biotechnology 30(10) (2012) 546.

[294] V. Mourino, A.R. Boccaccini, Bone Tissue Engineering Therapeutics: Controlled Drug Delivery in Three-Dimensional Scaffolds, Journal of The Royal Society Interface 7(43) (2010) 209.

[295] S. Nandi, S. Roy, P. Mukherjee, B. Kundu, D. De, D. Basu, Orthopaedic Applications of Bone Graft &Amp; Graft Substitutes : A Review, Indian Journal of Medical Research 132(1) (2010) 15.

[296] M.E. Elsalanty, D.G. Genecov, Bone Grafts in Craniofacial Surgery, Craniomaxillofacial Trauma & Reconstruction 2(3) (2009) 125.

[297] T. Albrektsson, C. Johansson, Osteoinduction, Osteoconduction and Osseointegration, European spine journal : official publication of the European Spine Society, the European Spinal Deformity Society, and the European Section of the Cervical Spine Research Society 10 Suppl 2(Suppl 2) (2001) S96.

[298] P. Janicki, G. Schmidmaier, What Should Be the Characteristics of the Ideal Bone Graft Substitute? Combining Scaffolds with Growth Factors and/or Stem Cells, Injury 42 Suppl 2 (2011) S77.

[299] M. Kucharska, B. Butruk, K. Walenko, T. Brynk, T. Ciach, Fabrication of in-Situ Foamed Chitosan/B-Tcp Scaffolds for Bone Tissue Engineering Application, Materials Letters 85 (2012) 124.

[300] W. Chen, H. Zhou, M. Tang, M.D. Weir, C. Bao, H.H.K. Xu, Gas-Foaming Calcium Phosphate Cement Scaffold Encapsulating Human Umbilical Cord Stem Cells, Tissue Engineering. Part A 18(7-8) (2012) 816.

[301] M. Costantini, A. Barbetta, 6 - Gas Foaming Technologies for 3D Scaffold Engineering, in: Y. Deng, J. Kuiper (Eds.), Functional 3D Tissue Engineering Scaffolds, Woodhead Publishing2018, pp. 127..

[302] A.G. Mikos, A.J. Thorsen, L.A. Czerwonka, Y. Bao, R. Langer, D.N. Winslow, J.P. Vacanti, Preparation and Characterization of Poly(L-Lactic Acid) Foams, Polymer 35(5) (1994) 1068.

[303] A. Sola, J. Bertacchini, D. D'Avella, L. Anselmi, T. Maraldi, S. Marmiroli, M. Messori, Development of Solvent-Casting Particulate Leaching (Scpl) Polymer Scaffolds as Improved Three-Dimensional Supports to Mimic the Bone Marrow Niche, Materials Science and Engineering: C 96 (2019) 153.

[304] N. Thadavirul, P. Pavasant, P. Supaphol, Development of Polycaprolactone Porous Scaffolds by Combining Solvent Casting, Particulate Leaching, and Polymer Leaching Techniques for Bone Tissue Engineering, Journal of Biomedical Materials Research Part A 102(10) (2014) 3379.

[305] H. Cao, N. Kuboyama, A Biodegradable Porous Composite Scaffold of Pga/B-Tcp for Bone Tissue Engineering, Bone 46(2) (2010) 386.

[306] C.-J. Liao, C.-F. Chen, J.-H. Chen, S.-F. Chiang, Y.-J. Lin, K.-Y. Chang, Fabrication of Porous Biodegradable Polymer Scaffolds Using a Solvent Merging/Particulate Leaching Method, Journal of Biomedical Materials Research 59(4) (2002) 676.

[307] Y.S. Nam, T.G. Park, Porous Biodegradable Polymeric Scaffolds Prepared by Thermally Induced Phase Separation, Journal of Biomedical Materials Research 47(1) (1999) 8.

[308] R. Akbarzadeh, A.M. Yousefi, Effects of Processing Parameters in Thermally Induced Phase Separation Technique on Porous Architecture of Scaffolds for Bone Tissue Engineering, Journal of Biomedical Materials Research 102(6) (2014) 1304.

[309] N. Sultana, M. Wang, Fabrication of Ha/Phbv Composite Scaffolds through the Emulsion Freezing/Freeze-Drying Process and Characterisation of the Scaffolds, Journal of Materials Science: Materials in Medicine 19(7) (2007) 2555.

[310] K. Whang, D.C. Tsai, E.K. Nam, M. Aitken, S.M. Sprague, P.K. Patel, K.E. Healy, Ectopic Bone Formation Via Rhbmp-2 Delivery from Porous Bioabsorbable Polymer Scaffolds, Journal of Biomedical Materials Research 42(4) (1998) 491.

[311] M.P. Prabhakaran, J. Venugopal, S. Ramakrishna, Electrospun Nanostructured Scaffolds for Bone Tissue Engineering, Acta Biomaterialia 5(8) (2009) 2884.

[312] H. Yoshimoto, Y.M. Shin, H. Terai, J.P. Vacanti, A Biodegradable Nanofiber Scaffold by Electrospinning and Its Potential for Bone Tissue Engineering, Biomaterials 24(12) (2003) 2077.

[313] C. Li, C. Vepari, H.-J. Jin, H.J. Kim, D.L. Kaplan, Electrospun Silk-Bmp-2 Scaffolds for Bone Tissue Engineering, Biomaterials 27(16) (2006) 3115.

[314] S. Bose, S. Vahabzadeh, A. Bandyopadhyay, Bone Tissue Engineering Using 3D Printing, Materials Today 16(12) (2013) 496.

[315] A.E. Jakus, A.L. Rutz, S.W. Jordan, A. Kannan, S.M. Mitchell, C. Yun, K.D. Koube, S.C. Yoo, H.E. Whiteley, C.-P. Richter, R.D. Galiano, W.K. Hsu, S.R. Stock, E.L. Hsu, R.N. Shah, Hyperelastic “Bone”: A Highly Versatile, Growth Factor–Free, Osteoregenerative, Scalable, and Surgically Friendly Biomaterial, Science Translational Medicine 8(358) (2016) 358ra127.

[316] Y. Yan, H. Chen, H. Zhang, C. Guo, K. Yang, K. Chen, R. Cheng, N. Qian, N. Sandler, Y.S. Zhang, H. Shen, J. Qi, W. Cui, L. Deng, Vascularized 3D Printed Scaffolds for Promoting Bone Regeneration, Biomaterials 190-191 (2019) 97.

[317] D.W. Hutmacher, T. Schantz, I. Zein, K.W. Ng, S.H. Teoh, K.C. Tan, Mechanical Properties and Cell Cultural Response of Polycaprolactone Scaffolds Designed and Fabricated Via Fused Deposition Modeling, Journal of Biomedical Materials Research 55(2) (2001) 203.

[318] J.-T. Schantz, A. Brandwood, D.W. Hutmacher, H.L. Khor, K. Bittner, Osteogenic Differentiation of Mesenchymal Progenitor Cells in Computer Designed Fibrin-Polymer-Ceramic Scaffolds Manufactured by Fused Deposition Modeling, Journal of Materials Science: Materials in Medicine 16(9) (2005) 807.

[319] J. Korpela, A. Kokkari, H. Korhonen, M. Malin, T. Närhi, J. Seppälä, Biodegradable and Bioactive Porous Scaffold Structures Prepared Using Fused Deposition Modeling, Journal of Biomedical Materials Research Part B: Applied Biomaterials 101B(4) (2012) 610.

[320] S. Ji, K. Dube, J.P. Chesterman, S.L. Fung, C.Y. Liaw, J. Kohn, M. Guvendiren, Polyester-Based Ink Platform with Tunable Bioactivity for 3D Printing of Tissue Engineering Scaffolds, Biomaterials Science 7(2) (2019) 560.

[321] J. Russias, E. Saiz, S. Deville, K. Gryn, G. Liu, R.K. Nalla, A.P. Tomsia, Fabrication and in Vitro Characterization of Three-Dimensional Organic/Inorganic Scaffolds by Robocasting, Journal of Biomedical Materials Research Part A 83A(2) (2007) 434.

[322] J.M. Williams, A. Adewunmi, R.M. Schek, C.L. Flanagan, P.H. Krebsbach, S.E. Feinberg, S.J. Hollister, S. Das, Bone Tissue Engineering Using Polycaprolactone Scaffolds Fabricated Via Selective Laser Sintering, Biomaterials 26(23) (2005) 4817.

[323] P.X. Lan, J.W. Lee, Y.-J. Seol, D.-W. Cho, Development of 3D Ppf/Def Scaffolds Using Micro-Stereolithography and Surface Modification, Journal of Materials Science: Materials in Medicine 20(1) (2009) 271.

[324] W. Bian, D. Li, Q. Lian, W. Zhang, L. Zhu, X. Li, Z. Jin, Design and Fabrication of a Novel Porous Implant with Pre-Set Channels Based on Ceramic Stereolithography for Vascular Implantation, Biofabrication 3(3) (2011) 034103.

[325] A. Ronca, L. Ambrosio, D.W. Grijpma, Preparation of Designed Poly(D,L-Lactide)/Nanosized Hydroxyapatite Composite Structures by Stereolithography, Acta Biomaterialia 9(4) (2013) 5989.

[326] D. Dean, W. Jonathan, A. Siblani, M.O. Wang, K. Kim, A.G. Mikos, J.P. Fisher, Continuous Digital Light Processing (Cdlp): Highly Accurate Additive Manufacturing of Tissue Engineered Bone Scaffolds, Virtual and Physical Prototyping 7(1) (2012) 13.

[327] D. Dean, E. Mott, X. Luo, M. Busso, M.O. Wang, C. Vorwald, A. Siblani, J.P. Fisher, Multiple Initiators and Dyes for Continuous Digital Light Processing (Cdlp) Additive Manufacture of Resorbable Bone Tissue Engineering Scaffolds, Virtual and Physical Prototyping 9(1) (2014) 3.

[328] P.F. Egan, I. Bauer, K. Shea, S.J. Ferguson, Mechanics of Three-Dimensional Printed Lattices for Biomedical Devices, Journal of Mechanical Design 141(3) (2019).

[329] Y. Zhang, C. Tse, D. Rouholamin, P.J. Smith, Scaffolds for Tissue Engineering Produced by Inkjet Printing, Central European Journal of Engineering 2(3) (2012) 325.

[330] S.M. Giannitelli, D. Accoto, M. Trombetta, A. Rainer, Current Trends in the Design of Scaffolds for Computer-Aided Tissue Engineering, Acta Biomaterialia 10(2) (2014) 580.

[331] M.R. Dias, J.M. Guedes, C.L. Flanagan, S.J. Hollister, P.R. Fernandes, Optimization of Scaffold Design for Bone Tissue Engineering: A Computational and Experimental Study, Medical Engineering and Physics 36(4) (2014) 448.

[332] D.W. Hutmacher, M. Sittinger, M.V. Risbud, Scaffold-Based Tissue Engineering: Rationale for Computer-Aided Design and Solid Free-Form Fabrication Systems, Trends in Biotechnology 22(7) (2004) 354.

[333] M. Wang, N. Yang, Three-Dimensional Computational Model Simulating the Fracture Healing Process with Both Biphasic Poroelastic Finite Element Analysis and Fuzzy Logic Control, Scientific Reports 8(1) (2018) 6744.

[334] P.S.P. Poh, D. Valainis, K. Bhattacharya, M. van Griensven, P. Dondl, Optimization of Bone Scaffold Porosity Distributions, Scientific Reports 9(1) (2019) 9170.

[335] P.F. Egan, K.A. Shea, S.J. Ferguson, Simulated Tissue Growth for 3D Printed Scaffolds, Biomechanics and Modeling in Mechanobiology 17(5) (2018) 1481.

[336] M.F. Pittenger, A.M. Mackay, S.C. Beck, R.K. Jaiswal, R. Douglas, J.D. Mosca, M.A. Moorman, D.W. Simonetti, S. Craig, D.R. Marshak, Multilineage Potential of Adult Human Mesenchymal Stem Cells, Science 284(5411) (1999) 143.

[337] D. Marolt, M. Knezevic, G.V. Novakovic, Bone Tissue Engineering with Human Stem Cells, Stem Cell Research & Therapy 1(2) (2010) 10.

[338] J.M. Seong, B.-C. Kim, J.-H. Park, I.K. Kwon, A. Mantalaris, Y.-S. Hwang, Stem Cells in Bone Tissue Engineering, Biomedical Materials 5(6) (2010) 062001.

[339] A.-M. Yousefi, P.F. James, R. Akbarzadeh, A. Subramanian, C. Flavin, H. Oudadesse, Prospect of Stem Cells in Bone Tissue Engineering: A Review, Stem Cells International2016 (2016) 6180487.

[340] A.J. Engler, S. Sen, H.L. Sweeney, D.E. Discher, Matrix Elasticity Directs Stem Cell Lineage Specification, Cell 126(4) (2006) 677.

[341] D.E. Discher, D.J. Mooney, P.W. Zandstra, Growth Factors, Matrices, and Forces Combine and Control Stem Cells, Science 324(5935) (2009) 1673.

[342] D.E. Discher, P. Janmey, Y.-l. Wang, Tissue Cells Feel and Respond to the Stiffness of Their Substrate, Science 310(5751) (2005) 1139.

[343] R.A. Marklein, J.A. Burdick, Controlling Stem Cell Fate with Material Design, Advanced Materials 22(2) (2010) 175.

[344] J.A. Burdick, G. Vunjak-Novakovic, Engineered Microenvironments for Controlled Stem Cell Differentiation, Tissue Engineering. Part A 15(2) (2009) 205.

[345] R.G. Flemming, C.J. Murphy, G.A. Abrams, S.L. Goodman, P.F. Nealey, Effects of Synthetic Micro- and Nano-Structured Surfaces on Cell Behavior, Biomaterials 20(6) (1999) 573.

[346] W. Chen, Y. Shao, X. Li, G. Zhao, J. Fu, Nanotopographical Surfaces for Stem Cell Fate Control: Engineering Mechanobiology from the Bottom, Nano Today 9(6) (2014) 759.

[347] S. Dobbenga, L.E. Fratila-Apachitei, A.A. Zadpoor, Nanopattern-Induced Osteogenic Differentiation of Stem Cells – a Systematic Review, Acta Biomaterialia 46 (2016) 3.

[348] M. Guvendiren, J.A. Burdick, Stem Cell Response to Spatially and Temporally Displayed and Reversible Surface Topography, Advanced Healthcare Materials 2(1) (2013) 155.

[349] M.J. Dalby, N. Gadegaard, R. Tare, A. Andar, M.O. Riehle, P. Herzyk, C.D.W. Wilkinson, R.O.C. Oreffo, The Control of Human Mesenchymal Cell Differentiation Using Nanoscale Symmetry and Disorder, Nature Materials 6 (2007) 997.

[350] S. Oh, K.S. Brammer, Y.S.J. Li, D. Teng, A.J. Engler, S. Chien, S. Jin, Stem Cell Fate Dictated Solely by Altered Nanotube Dimension, Proceedings of the National Academy of Sciences of the United States of America 106(7) (2009) 2130.

[351] A.B. Faia-Torres, M. Charnley, T. Goren, S. Guimond-Lischer, M. Rottmar, K. Maniura-Weber, N.D. Spencer, R.L. Reis, M. Textor, N.M. Neves, Osteogenic Differentiation of Human Mesenchymal Stem Cells in the Absence of Osteogenic Supplements: A Surface-Roughness Gradient Study, Acta Biomaterialia 28 (2015) 64.

[352] R. McBeath, D.M. Pirone, C.M. Nelson, K. Bhadriraju, C.S. Chen, Cell Shape, Cytoskeletal Tension, and Rhoa Regulate Stem Cell Lineage Commitment, Developmental Cell 6(4) (2004) 483.

[353] S.A. Ruiz, C.S. Chen, Emergence of Patterned Stem Cell Differentiation within Multicellular Structures, Stem Cells 26(11) (2008) 2921.

[354] K.A. Kilian, B. Bugarija, B.T. Lahn, M. Mrksich, Geometric Cues for Directing the Differentiation of Mesenchymal Stem Cells, Proceedings of the National Academy of Sciences of the United States of America 107(11) (2010) 4872.

[355] M. Guvendiren, J.A. Burdick, The Control of Stem Cell Morphology and Differentiation by Hydrogel Surface Wrinkles, Biomaterials 31(25) (2010) 6511.

[356] P. Viswanathan, M.G. Ondeck, S. Chirasatitsin, K. Ngamkham, G.C. Reilly, A.J. Engler, G. Battaglia, 3D Surface Topology Guides Stem Cell Adhesion and Differentiation, Biomaterials 52 (2015) 140.

[357] G. Kumar, C.K. Tison, K. Chatterjee, P.S. Pine, J.H. McDaniel, M.L. Salit, M.F. Young, C.G. Simon, Jr., The Determination of Stem Cell Fate by 3D Scaffold Structures through the Control of Cell Shape, Biomaterials 32(35) (2011) 9188.

[358] M. Guvendiren, S. Fung, J. Kohn, C. De Maria, F. Montemurro, G. Vozzi, The Control of Stem Cell Morphology and Differentiation Using Three-Dimensional Printed Scaffold Architecture, MRS Communications 7(03) (2017) 383.

[359] R.J. Morrison, S.J. Hollister, M.F. Niedner, M.G. Mahani, A.H. Park, D.K. Mehta, R.G. Ohye, G.E. Green, Mitigation of Tracheobronchomalacia with 3D-Printed Personalized Medical Devices in Pediatric Patients, Science Translational Medicine 7(285) (2015) 285ra64.

[360] W. Xue, B.V. Krishna, A. Bandyopadhyay, S. Bose, Processing and Biocompatibility Evaluation of Laser Processed Porous Titanium, Acta Biomaterialia 3(6) (2007) 1007.

[361] V.K. Balla, S. Bodhak, S. Bose, A. Bandyopadhyay, Porous Tantalum Structures for Bone Implants: Fabrication, Mechanical and in Vitro Biological Properties, Acta Biomaterialia 6(8) (2010) 3349.

[362] S.M. Bittner, B.T. Smith, L. Diaz-Gomez, C.D. Hudgins, A.J. Melchiorri, D.W. Scott, J.P. Fisher, A.G. Mikos, Fabrication and Mechanical Characterization of 3D Printed Vertical Uniform and Gradient Scaffolds for Bone and Osteochondral Tissue Engineering, Acta Biomaterialia 90 (2019) 37.

[363] G.A. Fielding, A. Bandyopadhyay, S. Bose, Effects of Silica and Zinc Oxide Doping on Mechanical and Biological Properties of 3D Printed Tricalcium Phosphate Tissue Engineering Scaffolds, Dental Materials 28(2) (2012) 113.

[364] C.M. Murphy, M.G. Haugh, F.J. O'Brien, The Effect of Mean Pore Size on Cell Attachment, Proliferation and Migration in Collagen-Glycosaminoglycan Scaffolds for Bone Tissue Engineering, Biomaterials 31(3) (2010) 461.

[365] L.G. Sicchieri, G.E. Crippa, P.T. de Oliveira, M.M. Beloti, A.L. Rosa, Pore Size Regulates Cell and Tissue Interactions with Plga-Cap Scaffolds Used for Bone Engineering, J Tissue Eng Regen Med 6(2) (2012) 155.

[366] A.C. Jones, C.H. Arns, A.P. Sheppard, D.W. Hutmacher, B.K. Milthorpe, M.A. Knackstedt, Assessment of Bone Ingrowth into Porous Biomaterials Using Micro-Ct, Biomaterials 28(15) (2007) 2491.

[367] S.J. Hollister, C.Y. Lin, E. Saito, C.Y. Lin, R.D. Schek, J.M. Taboas, J.M. Williams, B. Partee, C.L. Flanagan, A. Diggs, E.N. Wilke, G.H. Van Lenthe, R. Müller, T. Wirtz, S. Das, S.E. Feinberg, P.H. Krebsbach, Engineering Craniofacial Scaffolds, Orthodontics & Craniofacial Research 8(3) (2005) 162.

[368] M.J.P. Biggs, M.J. Dalby, Focal Adhesions in Osteoneogenesis, Proceedings of the Institution of Mechanical Engineers. Part H, Journal of engineering in medicine 224(12) (2010) 1441.

[369] J.D. Humphries, P. Wang, C. Streuli, B. Geiger, M.J. Humphries, C. Ballestrem, Vinculin Controls Focal Adhesion Formation by Direct Interactions with Talin and Actin, Journal of Cell Biology 179(5) (2007) 1043.

[370] C.M. Bidan, K.P. Kommareddy, M. Rumpler, P. Kollmannsberger, Y.J.M. Bréchet, P. Fratzl, J.W.C. Dunlop, How Linear Tension Converts to Curvature: Geometric Control of Bone Tissue Growth, PLoS One 7(5) (2012) e36336.

[371] C.M. Nelson, R.P. Jean, J.L. Tan, W.F. Liu, N.J. Sniadecki, A.A. Spector, C.S. Chen, Emergent Patterns of Growth Controlled by Multicellular Form and Mechanics, Proceedings of the National Academy of Sciences of the United States of America 102(33) (2005) 11594.

[372] M. Rumpler, A. Woesz, J.W.C. Dunlop, J.T. van Dongen, P. Fratzl, The Effect of Geometry on Three-Dimensional Tissue Growth, Journal of The Royal Society Interface 5(27) (2008) 1173.

[373] E.E. Golub, K. Boesze-Battaglia, The Role of Alkaline Phosphatase in Mineralization, Current Opinion in Orthopaedics 18(5) (2007) 444.